

Department of Exploration Geophysics

Groundwater Investigation Using the Seismoelectric Method

Mohammad Syamsu Rosid

This thesis is presented for the Degree of
Doctor of Philosophy
of
Curtin University of Technology

June 2007

Declaration

This thesis contains no material which has been accepted for the award of any other degree or diploma in any university.

To the best of my knowledge and belief this thesis contains no material previously published by any other person except where due acknowledgment has been made.

Signature:



Date: 14/06/2007

ABSTRACT

Seismoelectric methods are based upon an energy conversion from mechanical energy into electromagnetic energy when seismic waves pass through rocks. The electrokinetic sounding (EKS) is one such method that has great potential to probe for hydrogeological studies as it results from the movement of pore fluids under seismic excitation. In theory, the method should be able to directly map changes in hydraulic permeability, rock porosity, or fluid-chemistry.

The main purpose of this study is to test whether the seismoelectric response can be used to detect and map hydrogeology parameters such as changes of permeability, porosity, salinity, and thickness. This study is focused on survey design, approaches to reduce electronic and natural noise, and data processing techniques to combat ambient electromagnetic noise. The interpretation of data is another important component and guidelines and means to avoid processing artifacts and misinterpretation of ghost signals from multiple reflections.

Pitfalls in the method were examined and approaches to enhance the acquisition method developed. In practice, the limited number of acquisition channels, and the strength of type 1 unwanted signals compared to the desired Type 2 signals limits the effectiveness of the $f\text{-}k$ or $\tau\text{-}p$ filters. A solution to this problem was devised by combining shot records from 24 channels at different positions to perform a virtual 120 channels shot record. This composition allowed velocity or move-out dependent filters to perform more effectively.

Field measurements were undertaken in three different areas in Western Australia that could be characterised as shallow and deep aquifers, saline and fresh groundwater, and impermeable and permeable medium. These field measurements produced two types of electrokinetic response; non-radiating field Type 1, and radiating field Type 2 seismoelectric effects. The interpreted results from these data sets demonstrate that the electrokinetic responses can be detected from formations more than 60 metres deep. Some significant hydrogeological boundaries were recorded up to 21 m deep over a paleochannel in saline groundwater conditions, and

to at least 50 m deep in freshwater aquifers. Evidence is produced from these trials for electrokinetic signals arising from changes in permeability and fluid chemistry/salinity; thus supporting the basic theory of electrokinetic conversion, and providing further support to the assertion that electrokinetic conversion is a tool for hydrogeological investigation.

ACKNOWLEDGMENTS

I wish to acknowledge with appreciation the generosity of QUE Project Department of Physics University of Indonesia, and Cooperative Research Centre for Landscape Environments and Mineral Exploration (CRCLEME) for the financial support of my study and these experiments.

I would like to thank my supervisor, Dr. Anton W. Kepic, for help, advice and direction throughout the year and an enjoyable field surveys and challenging project. I have learnt so much from him while working in this project, and again thank him gratefully for all he has done for me during my time here. Thanks also to my chairpersons, Professor Norm Uren, Professor John Mc Donald and Professor Bruce Hartley and to my associate supervisor, Professor Jayson Meyers.

I am thankful to Delayed Yield Consulting, Department of Conservation and Land Management, and Water Corporation for also their financial support and supplying geological data and providing access to survey area in this study.

Thank you to Dr. Milovan Urosevic for helping me in seismic data processing.

Thanks also to Barret Cameron, Karen Gillgalon, Kim Bone, Bahman Bayat, Sioni Sioni, Don Hunter and Margarita Norvill for their assistance in the field to provide thousands blows of sledgehammer.

I would also thank Department of Exploration Geophysics Curtin University for guidance and provision of facilities throughout the year. I would particularly like to thank Dominic Howman for his kindness during my study.

Finally I would like to thank my mother, father and mother in law for their consistently moral support and my wife and all my children and all my family for their encouragement and their patiently accompanies during the year.

TABLE OF CONTENTS

Abstract	iii
Acknowledgments	v
Table of Contents	vi
List of Figures	viii
List of Tables	xi
1. Introduction	
1.1. Background	1
1.2. Motivation for Research	7
1.3. Objectives	9
1.4. Thesis Layout	9
2. The Electrokinetic Effect	
2.1. Introduction	11
2.2. Electrical Double Layer	15
2.3. Zeta and Streaming Potential	20
2.4. Macroscopic Electric Fields from Electrokinetic Effects	27
3. Acquisition Methodology	
3.1. Introduction	37
3.2. Instrumentation	38
3.2.1. Overview	38
3.2.2. Seismic Sources	39
3.2.3. Pre-Amplifier and Grounded Dipole Sensors	45
3.3. Noise	48
3.3.1. Seismic Related Noise	48
3.3.2. Electrical and Other Sources of Noise	51
3.4. Field Configuration	54

4. Methodology of Processing and Data Analysis	
4.1. Introduction	59
4.2. Removal of Powerline Harmonic Noise	61
4.3. Band-Pass Filter	64
4.4. F-K Filtering	71
4.5. Data Analysis for Interpretation	77
5. Field Experiments	
5.1. Introduction	82
5.2. Experiments at Nambi, Leonora	84
5.2.1. Field and Hydrogeological Description	84
5.2.2. Results and Discussion	85
5.3. Experiments at Lake Bryde, Pingrup	91
5.3.1. Field and Hydrogeological Description	91
5.3.2. Results and Discussion	94
5.3.3. LB03 AVO Analysis	105
5.4. Experiments Near the Blackwood River, Nannup	107
5.4.1. Field and Hydrogeological Description	107
5.4.2. Results and Discussion	112
5.4.2.1. Seismic Data	112
5.4.2.2. Seismoelectric Data	117
5.4.2.3. BW17 AVO Analysis	126
5.5. Enhancing the Data from BW16 and BW25 with a Virtual Shot Gather	128
5.5.1. BW25 AVO Analysis	139
6. Conclusions and Recommendations	
6.1. Conclusions	142
6.2. Recommendations	146
References	148

LIST OF FIGURES

Figure 1.1. – Statistical and true piezoelectric effects	5
Figure 2.1. – A simple illustration of electrokinetic processes	13
Figure 2.2. – A Stern model of the structure of the electric double layer on rock-fluid interface	17
Figure 2.3. – Electrostatic potential near a negatively charged mineral grain ..	19
Figure 2.4. – (a)- Schematic of chamber	22
(b)- Cross-section of a capillary tube	22
Figure 2.5. – Reflection wave within a Fresnel zone	30
Figure 2.6. – A Pythagorean theorem to calculate the radius of the Fresnel Zone	31
Figure 2.7. – Two types of seismoelectric response in nature	36
Figure 3.1. – The source of seismic excitation	41
Figure 3.2. – A shallow shot is blowing out at Nambi surveys	43
Figure 3.3. – (a)- Coherent noise in a Lake Bryde seismoelectric shot record	49
(b)- The power spectrum shows the 50 Hz power line noise	49
Figure 3.4. – Field illustration how to avoid noise during acquisition	53
Figure 3.5. – Geometry of 24 dipoles configuration with (a)- contiguous dipoles configuration	56
(b)- overlapping dipole with split spread configuration	56
Figure 4.1. – An example of raw seismoelectric and seismic data	60
Figure 4.2. – Powerline harmonic noise of 50 Hz and 2500 Hz	63
Figure 4.3. – The characteristic curve of a hypothetical band-pass filter ...	64
Figure 4.4. – Butterworth response of phase and group delay	68
Figure 4.5. – Impulse responses of Butterworth band-pass filter	69
Figure 4.6. – An example of filtered Nannup seismoelectric data	70
Figure 4.7. – An f - k analysis of seismoelectric shot record	73
Figure 4.8. – An example of f - k filtered electrokinetic data	76
Figure 5.1. – A geological section of the Nambi seismoelectric survey	84
Figure 5.2. – Raw Nambi seismic and seismoelectric data	85

Figure 5.3. – Processed Nambi seismic and seismoelectric data	87
Figure 5.4. – An example of velocity picking to find a velocity model ...	88
Figure 5.5. – Time to offset curve of first break picking from Nambi seismic data	89
Figure 5.6. – Location of the Lake Bryde catchment, Pingrup	91
Figure 5.7. – Borehole logs data of Lake Bryde site	92
Figure 5.8. – Two seismic shot records from LB03	95
Figure 5.9. – First break picking curves of LB03	96
Figure 5.10. – Raw seismoelectric data of	
(a)- LB01	97
(b)- LB02	97
(c)- LB03	97
Figure 5.11. – Filtered seismoelectric data from LB03	100
Figure 5.12. – Enlarged view of LB03 shot #18	103
Figure 5.13. – AVO analysis of LB03	106
Figure 5.14. – Topography of the Nannup survey area	108
Figure 5.15. – The local survey area and variation of its watertable surface	110
Figure 5.16. – Borehole logs data of BW17 Nannup site	111
Figure 5.17. – Example of raw seismic refraction and reflection from BW17	113
Figure 5.18. – First break curve of BW17	114
Figure 5.19. – Interpreted near-surface brute stack seismic section	116
Figure 5.20. – Raw seismoelectric data and their amplitude of	
(a)- BW 25	118
(b)- BW 17	118
(c)- BW 27	118
Figure 5.21. – Photograph of seismoelectric acquisition at BW17	119
Figure 5.22. – A series of type 2 seismoelectric signals of BW17	121
Figure 5.23. – Enlarged and interpreted view of BW17 shot #6 records	123
Figure 5.24. – AVO Analysis of BW17	127
Figure 5.25. – Geological and geophysical log data from BW27	128
Figure 5.26. – The processed seismoelectric records of BW27	129

Figure 5.27. – Raw Seismoelectric data: individually and its virtual 100+ channels	
(a)- from BW16	131
(b)- from BW25	131
Figure 5.28. – First break picking time to offset curve of	
(a)- BW 16	133
(b)- BW 25	133
Figure 5.29. – An example of seismoelectric data from BW16	
(a)- Raw data	137
(b)- Filtered and Interpreted data	137
Figure 5.30. – An example of seismoelectric data from BW25	
(a)- Raw data	138
(b)- Filtered and Interpreted data	138
Figure 5.31. – Analysis of AVO of BW25 Nannup data	140

LIST OF TABLES

Table 2.1. – Principal electrokinetic processes	12
Table 5.1. – Field experiments carried out as part of this research	83
Table 5.2. – The velocity model of LB03	96
Table 5.3. – Depth to time conversion of geological interfaces of LB03	102
Table 5.4. – The velocity model of BW17	115
Table 5.5. – The stacking velocity model	116
Table 5.6. – Depth to (One Way) Time conversion of BW17	124
Table 5.7. – Velocity model of BW16 and BW25	134
Table 5.8. – Conversion of depth to one way time of BW16	135
Table 5.9. – Conversion of depth to transit time of BW25	136

CHAPTER 1

INTRODUCTION

1.1 Background

The seismoelectric effect has been examined both theoretically and experimentally since the 1930's. It is a conversion of mechanical energy into electromagnetic energy when seismic waves pass through rocks. Seismoelectric effect has been studied for decades, but there is no widely established seismoelectric method to characterize the earth. This thesis is a step towards making the effect become a more widely used geophysical technique to characterize the earth. Debye (1933) was the first to propose the electrokinetic model that acoustic waves can generate electric fields at liquid-solid interfaces. Thompson (1936) provided the first published field evidence of seismoelectric signals, and hypothesized that the variation in resistivity with elastic deformation was the mechanism for the observed seismic-to-electric coupling. Since then, other seismoelectric field recordings have been published by Martner and Sparks (1959), Broding et al. (1963), Long and Rivers (1975), Thompson and Gist (1993), Kepic et al. (1995), Butler et al. (1996), Beamish (1999), Garambois and Dietrich (2001), and Rosid and Kepic (2003, 2004). Meanwhile, Frenkel (1944), Biot (1956a, b), and Neeve and Yeats (1989) have made important developments in the basic theory and physical models of electrokinetic effects in porous media. More recently, Pride (1994), Pride and Haartsen (1996), and Haartsen and Pride (1997) have developed mathematical expressions for the electrokinetic coupling of seismic-to-electromagnetic disturbances in the Earth, which may be used to accurately forward model complicated earth structures via finite difference approximation. Also some laboratory test results have been published by Revil et al. (1996) who tested the influence of saline water, and Zhu et al. (2000) that developed a borehole model. Some authors have also discussed the possibility of geopotential phenomena such as earthquakes (Mizutani et al., 1976; and Ishido and Mizutani, 1981) and geothermal influences (Corwin and Hoover, 1979) to be related to the electrokinetic coupling processes.

There are at least four causes of seismoelectric effects (Butler et al., 1996): resistivity modulation, piezoelectric effects, radio pulsed effects (RPE), and electrokinetic effects.

1.1.1 Resistivity Modulation

Resistivity modulation occurs when the acoustic wave modulates the resistance of the earth, causing electrical potentials to vary when telluric currents are present in the ground. This effect, also called J-effect by Blau and Statham (1936), is the earliest seismoelectric effect observed by Thompson (1936, 1939). Zablocki (1966) and Long and Rivers (1975) also claim to have observed these effects. These observations are supported by Brace and Orange (1968a, b) with their laboratory data that shows that variation in electrolyte saturation and pore pressure cause significant variations of resistivity. At low pressure the effect of pressure can be worked as a partially saturated rock becomes less resistive, whereas saturated rock becomes more resistive as the pressure increases. The general expression of the potential-versus-distance for a point electrode at the surface of a horizontally layered medium can be shown as

$$V(r) = \frac{I \rho_1}{2\pi r} G(r, k) \quad 1.1$$

where I is current, ρ_1 is the surface layer resistivity, r is the radial distance from the electrode, k is the factors of resistivity contrast or the reflection coefficient of layers (which $-1 < k < 1$) and $G(r, k)$ is the Kernel function and is dependent on layering (Grant and West, 1965). Telford et al. (1996) defines the function $G(r, k)$ for a fixed value of r , as

$$G(r, k) = \left[1 + 2 \sum_{m=1}^{\infty} \frac{k^m}{\left\{ 1 + (2mz/r)^2 \right\}^{1/2}} \right] \quad 1.2$$

where z is the depth of layer, and m is the layer index. The first term is the normal potential factor (if the earth was homogenous and uniform) and the second term is referred to as the disturbing potential factor. As a seismic wave passes through the earth, resistivity modulation within any layers will cause $V(r)$, I , and $G(r,k)$ to become functions of time (Long and Rivers, 1975). With regard to their experiment (at the effective radius $r = r_o$ from the current electrode) if the current electrode is held at a constant voltage (as is normally the case) then equation (1.1) could be written as,

$$V(r,t) = \frac{V_o r_o G[r,k(t)]}{r G[r_o,k(t)]} \quad 1.3$$

From equation (1.3) we can see that the voltage-versus-distance relation is determined only by the resistivity contrast factors $k(t)$, which is referred to the surface resistivity. The resistivity layering function $G(r,k)$ can be obtained from Schlumberger or Wenner depth sounding. However, if a constant current were maintained through the electrode, a change in the surface resistivity which includes disturbances near the electrode contact will generate voltages. The condition of constant voltage, therefore, represents an anomalous seismoelectric response caused by resistivity changes below the surface layer. The constant current conditions, on the other hand, gives voltage changes that represent a seismoelectric response caused by the change in resistivity.

1.1.2 Piezoelectric Effect

Piezoelectricity is generated within certain classes of crystals when a seismic wave deforms the crystal lattice along sensitive axes. The phenomenon can physically be described as follows. Piezoelectricity is a mechanic-to-electric coupling mechanism characterizing insulating crystals which lack centers of symmetry. So, piezoelectric properties depend upon symmetry of spin. All minerals without a centre of symmetry may be piezoelectric. Even aggregates of piezoelectric crystals are piezoelectric if the grains are suitably aligned (Bishop, 1981). Quartz is the most common, and most important, natural mineral with piezoelectric properties.

Precision cut crystals are commonly used in radio transmitters/receivers, ‘everlasting’ cigarette lighters, and ‘quartz’ watches, which exploit this characteristic.

The possibility of piezoelectric effects generated by acoustic waves in rocks was first observed by Volarovich and Parkhomenko (1954). Since then, the piezoelectric effect in natural fabrics has been studied in both laboratory measurements (Tuck et al., 1977) and field measurements in the former Soviet Union to locate quartz veins and pegmatite bodies (Volarovich et al., 1959; Volarovich and Sobolev, 1969). However, their analyses have shown that while piezoelectric effects were measured, it has not been proved that the effects were related to the structure of the crystal (fabric). Bishop (1981), later reported that piezoelectric effects are not only due to randomly aligned grains, termed as a statistical effect (Tuck et al., 1977), but may be due to alignment within the fabric. He demonstrated the alignment phenomena in laboratory studies of quartz mylonites. In regards to the laboratory tests, the first phenomenon is dependent on the number of mineral grains in the sample, whereas the second phenomena effect depends upon the orientation of the grains. In principle, the piezoelectric axes in an aggregate may be random, spatially aligned or polar aligned. The illustration of this hypothesis can be seen schematically at Figure 1.1. However, some scientists still believe that the piezoelectric effects in naturally occurring rocks are rare phenomena, because random alignment of the piezoelectric crystals in the rocks results in an overall cancellation of any large-scale electric fields (Sobolev et al., 1984).

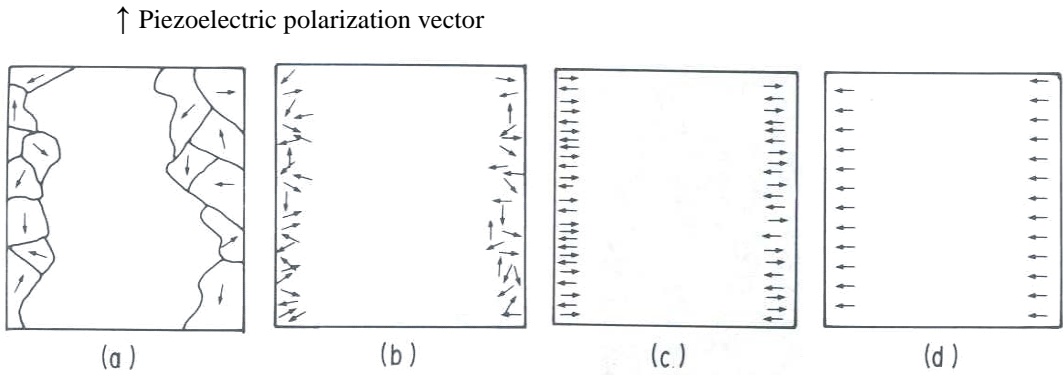


Figure 1.1. Statistical and true piezoelectric effects. (a) Large random grains, large statistical effect, (b) Small random grains, small statistical effect, (c) Spatially aligned but random polarity, (d) Polar aligned, a true piezoelectric effect (after Bishop, 1981).

1.1.3 Radio Pulse Effect

The radio pulsed effect (RPE) is a highly non-linear process in sulfide-rich rocks that generates high frequency electromagnetic responses (audio-band to radio-waves) from strong acoustic waves. The phenomenon was discovered by Sobolev et al. (1980) in the late 1970's as they observed that many piezoelectric field data contained distinctive pulses when sulfide minerals were in the vicinity. Since then, Sobolev et al. (1984), Maxwell et al. (1992), Kepic et al. (1995 and 2001) have claimed that the RPE phenomenon have been detected and may be used to assist in mapping sulfide ore bodies. The effect was initially referred to as PRRER, pulsed radio range electromagnetic radiation, but Sobolev et al. (1982) have subsequently renamed it RPE, radio pulsed effect (Kepic et al., 1995 and 2001). Although Sobolev et al. (1982) claimed that rock fractures are strongly suspected, the exact cause of RPE is unknown. Kepic et al. (1995) have stated that there are six typical features of RPE signals: (1) a relatively high amplitude pulse of short duration, (2) order of peak electric field amplitudes is millivolts to tens of millivolts, (3) pulse bandwidths were in the range of kHz to few MHz (Sobolev et al., 1982), (4) the signals need a critical seismic energy (Sobolev et al., 1982; Maxwell et al., 1992), (5) greater amounts of seismic energy tend to stimulate more signals rather than greater amplitudes, (6) unlike other seismoelectric effects, the relationship between

stress and electromagnetic field strength in RPE is non-linear (as is EM from rock fracture, Nitsan, 1977; Yamada et al., 1989).

1.1.4 Electrokinetic Effect

Electrokinetic effects seen in field measurements were initially described as a seismoelectric effect of second kind or E-effect (Ivanov, 1940), and were explained as an electrofiltration phenomenon in moist soil. It resulted from a coupling between fluid flow and electric current flow in a medium containing both solid and liquid component. This effect is the most widely reported and studied of the four known physical mechanisms and generally produces the largest electric fields. Our understanding of this effect has significantly improved since Ivanov's work in the 1940's due to many field studies and theoretical papers in this area. Most of the studies listed in the beginning of this chapter are studies of this effect because it is so readily produced compared to the other types of seismoelectric effects.

The electrokinetic effect is similar to the more familiar streaming potential phenomenon that groundwater forced to move through a capillary or porous plug induces a difference of electric potentials. This mechanical or sonic-to-electrical coupling mechanism is a conversion from kinetic to electrical energy. The mechanism occurs at the solid-liquid interface within a rock matrix where a charge distribution attributed to an electric double layer (i.e. mobile and immobile layers) is generated and facilitates the coupling. The electrokinetic response emerges because the relative motion of the electrically charged ions in the pore fluid naturally tends to equilibrium conditions. Therefore, the existence of seismic p-wave perturbation induces a small scale motion of fluid relative to the solid matrix layer and causes an imbalance of the mobile ions and so leads to a small scale electric current, which can result in macroscopic polarization and resulting electric fields. Further reference to "seismoelectric" in this thesis refers to seismoelectric signals due to electrokinetic mechanisms.

1.2 Motivation for Research

The seismoelectric exploration method based upon electrokinetic conversion has been sporadically implemented since 1939 to detect the water table and very near subsurface boundaries. It was first promoted by Ivanov (1939, 1940) even though his field data records were not clearly linked to a subsurface interface. Moreover, the delay time between shot detonation and electrical response was associated with the shot-to-dipole separation rather than the distance from shot to any particular interface or target, as you would expect from electrical signals from interfaces. A better demonstration was by Martner and Sparks (1959), who used a single channel seismograph and documented clear seismoelectric responses from the base of a weathered layer. Broding et al. (1963) investigated the response along a 35 m profile in a borehole and found that the peak signal associated with a sandy loam–shale interface. Parkhomenko and Gaskarov’s (1971) borehole measurements show that seismoelectric responses in limestone were consistently stronger than the event observed in clays. Butler et al. (1996) detected electrokinetic responses from a sand/gravel–glacial till boundary using an eight channel data acquisition system and multiple sensors. Similar field measurements and numerical simulations were carried out by Mikhailov et al. (1997) which also identified the electrokinetic conversion from a top soil–glacial till interface as well as signals from the water table and the glacial till–bedrock interface. Garambois and Dietrich (2001) reported that electrokinetic responses were detected from two boundaries at 2 and 10 m depth. They also reported that the magnetic fields were detected moving along with the shear waves, which was predicted by numerical models of Pride and Haartsen (1996) and Haartsen and Pride (1997). However, all of these field results generally show that the prior field works of seismoelectric response only recorded one layer, which is usually from a very shallow boundary. The seismoelectric events that are generated from multi and deeper layer sources are the target of our controlled field surveys. The effectiveness of data acquisition as well as data processing is another challenge that has to be faced to help practitioners use the method to probe hydrogeological parameters.

As the seismoelectric effect is strongly dependent on the mobility of ions within the electrical double layer, it has great potential, in theory, to directly measure important

transport properties of rocks such as hydraulic permeability contrasts (shale – reservoir sand, or fractured zone) or changes in pore surface chemistry (oil – water contact). Recently, there has been more activity in testing the method in various groundwater problems (see Strachan and Wolfe, 2001; Butler et al., 2002; Boulytchov, A., 2002; and Rosid and Kepic, 2004). Despite the recent resurgence in field studies, there are few successful case histories to support the promise that the method is able to map permeability contrasts and pore chemistry changes in the subsurface. This situation is understandable as the amplitudes of the electrical signals produced from the seismic wave are millivolts per metre to microvolts per metre, and measuring such signals in the presence of cultural interference, which is usually much greater in magnitude, is difficult. Therefore, further field studies are needed to develop acquisition and signal processing methodology as well as testing the seismoelectric method's viability.

Porosity ϕ and permeability k of rocks, two important physical properties (of rocks), are still very challenging to measure by geophysical field methods. However, the electrokinetic coupling mechanism to produce the seismoelectric response depends upon the small scale separation of electrical charge due to relative motion of pore fluid and rock matrix induced by seismic waves. In principle, this electric field is proportional to physical properties such as porosity and fluid permittivity, and is inversely proportional to fluid viscosity. Therefore:

1. the seismoelectric method may be able to detect differences in porosity ϕ and permeability k of geological formations from field measurements;
2. the seismoelectric effect may allow quantitative interpretation of permeability if some of the fluid properties and subsurface chemistry are known or estimated; and
3. conversely, changes in fluid properties may be detected if other physical parameters do not vary too much, that for example saline/fresh water interface and groundwater contaminant could be detected by this method.

1.3 Objectives

The principal aim of my study is to examine whether seismoelectric effects can detect and map significant changes in aquifer permeability, salinity and thickness. Many past studies appear to be opportunistic rather than controlled tests. Very few of the researchers cited have published more than one example of field data. Most of the researchers listed in advance have published one field test only. With regard to the issues above some controlled field surveys have been designed and tested to characterise the seismoelectric responses from porous, layered, fresh and saline, and saturated and unsaturated media in both shallow and deeper aquifers. To assist in determining the physical cause of differences in the seismoelectric response, the field experiments need to be supported by other geophysical methods such as well-log data, electrical surveys, and both refraction and reflection seismic data.

An additional aim is to produce a robust strategy for the electrode configuration, acquisition, processing, and interpretation of seismoelectric data. Unlike seismic exploration, the seismoelectric method has no standard procedure/methodology to provide subsurface information. There is currently little information in the aforementioned published studies about the means of data acquisition, signal processing, and data interpretation (with the exception of the thesis of Butler, 1996). Electrical noise is an important problem potential practitioners are faced with in seismoelectric prospecting.

1.4 Thesis Layout

This thesis is divided into six chapters. Chapter 1 reviews the basic issues and prior research relevant to the seismoelectric method. It discusses the motivations behind this thesis and sets out the main research objectives.

Chapter 2 discusses theoretical aspects of electrokinetic effects, relating the physical aspects most relevant to the seismoelectric phenomenon. Electrical double layer, streaming potential, and zeta potential that are the main factors in electrokinetic effects are discussed in detail to assist in understanding the phenomenon and in

interpretation of data in later chapters. The means to develop the second type of seismoelectric signals in nature (electromagnetic fields) is also described in this chapter.

Chapter 3 explains the methodology of experiments which focussed on aspects of instrumentation, electrical noise in the field and its sources, and field configurations. Sources of seismic excitation, pairs of dipoles stakes and preamplifiers, and seismograph systems as the principal instruments are explained and shown in figures. Noise is the greatest challenge in our study and is also discussed in this chapter beginning from the types, their sources, their effects on the electrokinetic signals, to how we can avoid it as optimally as possible during measurements. Field configurations that can be used as part of noise minimizing procedures are also illustrated in the end of this chapter.

The methodologies of data filtering to process field data that is still contaminated by noise are discussed in Chapter 4. Removal of powerline harmonic noise, band-pass filtering, and f - k filtering are techniques applied in our data processing. The filters are used to attenuate unwanted frequency signals, such as VLF (very low frequency) and AM (amplitude modulation) high radio frequency, low frequency of signals from Type 1 electrokinetic effects, and railways and powerline harmonics noise. It might also be used to suppress undesired signals associated with slower velocity ground-roll waves or direct waves. The criteria to identify the seismoelectric events are also delivered in this chapter.

In Chapter 5, field experiments are the focal topic. Experiments at three different test areas are discussed. This chapter discusses the electrokinetic responses seen in both raw shot records and processed data and provides some interpretation of the data, supported by seismic (refraction and shallow reflection) and geology and geophysical (well log data). Amplitude-versus-offset curve analysis as a main tool in data interpretation is also well discussed.

Finally, the conclusions are summarized and the outcomes from this study are given in Chapter 6. The overall results achieved by this study are discussed and some suggestions and recommendations are made for further study.

CHAPTER 2

THE ELECTROKINETIC EFFECT

2.1 Introduction

The seismoelectric effect may be described as a seismic-to-electrical coupling mechanism that results from a coupling between fluid flow and electric current flow in a medium containing both solid and liquid components. The coupling is facilitated by a charge distribution known as the electrical double layer (adsorbed and diffuse layers) that takes place at the solid-liquid interface within the rock matrix. Therefore, porous rocks need to be at least partially saturated by an electrolyte fluid (such as water), or no seismoelectric responses are expected since there is no electrical double layer due to a lack of a polar pore fluid (Zhu and Toksoz, 2003). The electrokinetic effect is similar to the more familiar phenomenon of streaming potential, and arises because one ion species within the electric double layer is located predominately in the liquid and is free to move within the liquid relative to the solid. Thus, when seismic P-waves induce small scale motion of the fluid/diffuse layer relative to the solid matrix/adsorbed layer an imbalance of the mobile ions versus fixed ions leads to small scale electric currents. These small currents can collectively result in macroscopic electric polarization and electric fields.

There are four principal electrokinetic processes of interest: electrophoresis, electroosmosis, streaming potential, and sedimentation potential. Electrophoresis is the motion of charged colloidal particles in an electric field. Currently, it has the greatest practical use and is used in many commercial instruments to separate macromolecules on the basis of size, electric charge, and other physical properties. The degree of separation depends upon both charge and mass forces. The electroosmosis effect, which was the most popular method in the past to determine the zeta potential, occurs when an electric field causes motion of the liquid. As the silica walls of the capillary are fixed and negatively charged, a layer of cations builds up near the surface to maintain the charge balance. It creates a double layer of ions

near the surface as well as a potential difference, which is known as the zeta potential. When the voltage is applied across the capillary the cations forming the double layer are attracted to the cathode. They, therefore, move through the capillary, and drag the bulk solution behind them as they are solvated.

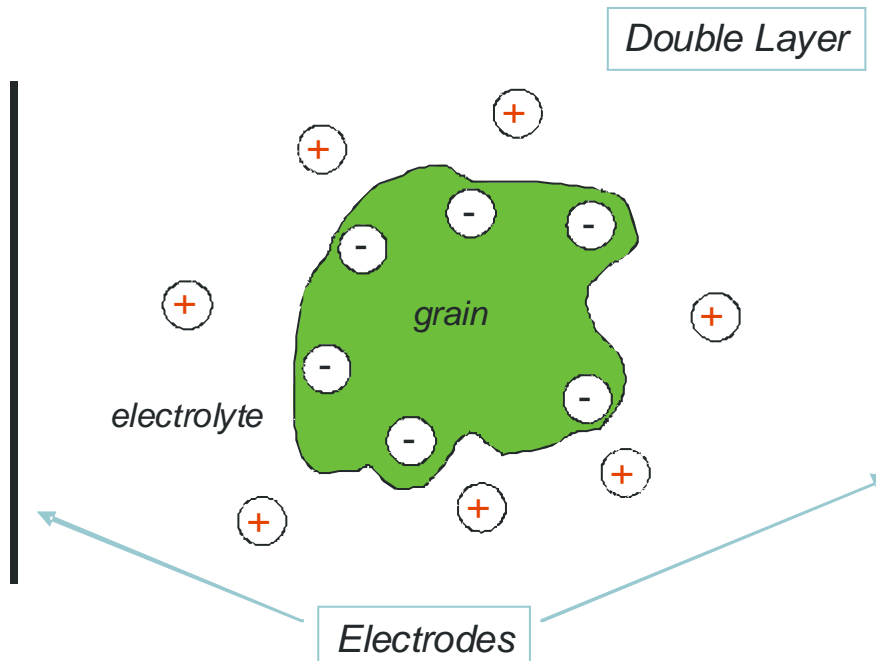
Table 2.1 Principal electrokinetic processes (after Hunter, 1981).

Technique	What Is Measured	What Moves	What Causes Movement
Electrophoresis	Velocity	Particles move	Applied electric field
Electro-osmosis	Velocity	Liquid moves in capillary	Applied electric field
Streaming Potential	Potential	Liquid moves	Pressure gradient
Sedimentation Potential	Potential	Particles move	Gravity = $g \Delta \rho$

The velocity of the colloids in electrophoresis and the difference of pressures between two ends of a capillary (or porous plug) in electro-osmosis are proportional to the applied electric field strength. These two effects are examples of electrical forces doing work. The other two effects, the streaming potential and sedimentation potential are examples of kinetic energy being converted to electrical energy. In the case of streaming potential the polar fluid is forced through a capillary or porous plug and an electrical potential difference is created. This potential difference is proportional to the applied pressure. Sedimentation potential is the forced motion of charged solid particles in a liquid (e.g. due to gravitation) to create a difference in electric potential. This potential is proportional to the velocity of the particles. For further study of all these processes we can refer to Shaw (1969) and Hunter (1981).

Electrokinetic phenomena often accompany one another, for instance, electrophoresis is always accompanied by electro-osmosis due to electric charge

build-up at the wall of an electrophoretic cell. Electro-osmosis processes are also accompanied by streaming potentials and vice versa as one tends to stimulate the other (see Figure 2.1). However, the main electrokinetic effect of interest in this study is the streaming potential. Therefore, further reference to electrokinetic processes in this thesis refers to electrokinetic effects due to the streaming potential mechanism. This study focuses upon the electrical signals recorded by the action of acoustical waves.



Electroseismic/Electro-osmotic : Apply Voltage → Motion

Seismoelectric/Streaming Potential : Apply Motion → Voltage

Figure 2.1. A simple illustration of electrokinetic processes.

The electrokinetic responses are generated when acoustic waves pass through a boundary within either fully or partially saturated media. At interfaces where contrasts in physical properties such as acoustic impedance, or fluid type occur, a portion of the incident seismic wave is converted to a Biot slow wave. The Biot slow wave at seismic frequencies is a diffusive pressure wave in the pore fluid. The

slow wave generates relative movement between the pore fluid and the rock grains. This relative motion distorts the electric dipoles on the mineral surfaces and leads to an electrical field known as the streaming potential. The streaming potential has the same time-dependent behavior as the incident seismic wave. The resulting electromagnetic wave propagates much faster than any acoustic wave to the surface where it can be detected with an array of electric field antennas.

On the other hand, the inverse of the seismoelectric conversion is attributed to electroseismic or electro-osmosis conversion. In this case energy is converted from electromagnetic energy into kinetic energy. An antenna on the surface acts as a source that generates a time varying electric field. When this electric field encounters a boundary that has a contrast in either elasticity or chemistry (e.g. ion species) a time varying pressure is generated at the boundary. This pressure fluctuation propagates to the surface as an acoustic wave, and may be recorded by geophones.

There are at least three main physical properties that influence the seismoelectric responses: porosity, permeability, and fluid-chemistry of rocks. Rock porosity is assumed to consist of a packing of solid grains which is saturated by a fluid electrolyte. High porosity may result in stronger electrokinetic effects due to a thicker double layer, which allows for more charge transport. Laboratory studies by Jouniaux and Pozzi (1995) show that the permeability of a sample strongly influences the streaming potential when fluid resistivity is high, but is less influential when the fluid is conductive. The fluid-chemistry parameter such as the salinity of water has a strong correlation to its seismoelectric response. The largest streaming potentials are associated with fresh fluid environments (Revil *et al.*, 1996), whereas, a highly conductive environment will reduce the amount of charge separation, because the electric field within a pulse is determined by the exact balance between the streaming current and the resultant conduction current (Haartsen and Pride, 1997). However, the electrical conductivity of rock strongly depends on both clay content within the rock matrix and saline water, as its fluid environments. In addition, the electrokinetic signals are directly proportional to the zeta potential (i.e. an electrokinetic parameter of the fluid–rock interface describing the potential gradient in the double electric layer). Thus, both pore fluid and rock

surface chemistry are important factors in determining the magnitude of seismoelectric responses. In summary, there are a number of factors that may influence the seismoelectric response. Some factors, such as salinity, may assist in increasing the magnitude of the response, but at high values decrease the net response. Whilst there is reasonable hope that the seismoelectric response is related to formation permeability, the interplay of other factors means that it is unlikely that we can uniquely determine hydraulic permeability via this method alone.

2.2 Electrical Double Layer

The electrical double layer is a physical phenomenon commonly found in natural environments where a plasma exists (i.e. ions that are free to move). It was first proposed by Helmholtz in 1879, and then developed by Stern from the measurements of electrode potentials and capacities and from streaming potential and electro-osmosis experiments using glass capillaries (Davis *et al.*, 1978). It plays an important role in generating the electrokinetic effect. Without an electrical double layer no seismoelectric responses are expected. What is the electrical double layer? Imagine, every morning at rush hour in a metropolitan city, such as Tokyo, at the door of an intercity train, one layer of passengers who can't move at all and are pushed against the door of the train. Behind them is a second layer of passengers who can move around a little. Similar to this analogy of door glass and passengers, one layer of ions is strongly bound to the mineral surface and a second layer of diffuse ions exist within electrolyte. This couple is named the electrical double layer.

The electric double layer of interest to us is emplaced along the capillary at the interface between the crystal and the pore fluid. It is called a “double layer” because it contains two ionic layers, which strongly differ in characteristics. There are immobile ions within the “Stern layer”, and mobile ions in a diffuse layer within the pore fluid. Due to unsatisfied bonds at the surface of the mineral grains (Fitterman, 1978) and adsorptions of ions from fluid, or other mechanisms (Neev and Yeats, 1989), a charge density develops at the surface-pore fluid interface. For silicate minerals and most crustal rocks, this layer is usually negatively charged. These

charges cannot be removed, but they can be neutralized if free charges or ions are nearby. To preserve electrical neutrality, positive ions – called counter-ions – are bonded strongly to the negative quartz surface, and form an immobile ionic zone. The ions are bonded through both van der Waals and Coulomb electrostatic forces. This layer is also known as the Helmholtz or Stern layer. Its thickness is generally less than 1 nm (Sumner, 1976).

Additional positive ions are still attracted and concentrated in solution in the vicinity of solid surface. However, in addition to the Coulomb attraction of the surface they are also repelled by the Stern layer as well as by other positive ions that are also trying to approach the surface. Thus, the positive ions have a high concentration near the surface that gradually decreases with distance, until it reaches equilibrium with the counter-ion concentration in the solution. In a similar fashion, there is a lack of negative ions in the neighborhood of the surface, because they are repelled by the negative surface. Their concentration will gradually increase with distance, as the repulsive forces of the surface charges are screened out by the positive ions, until equilibrium is again reached. These elasto-dynamic equilibriums result in a diffuse layer with mobile ions. The diffuse layer can be visualized as a charged atmosphere surrounding the mineral surface. The charge density at any distance from the surface is equal to the difference in concentration of positive and negative ions at that point. Charge density is greatest near the grain and gradually diminishes toward zero as the concentration of positive and negative ions merge together. The attached counter-ions in the adsorbed layer and the charged atmosphere in the diffuse layer are named as the electric double layer (see Figure 2.2).

**Net positive charge free
to move with pore water**

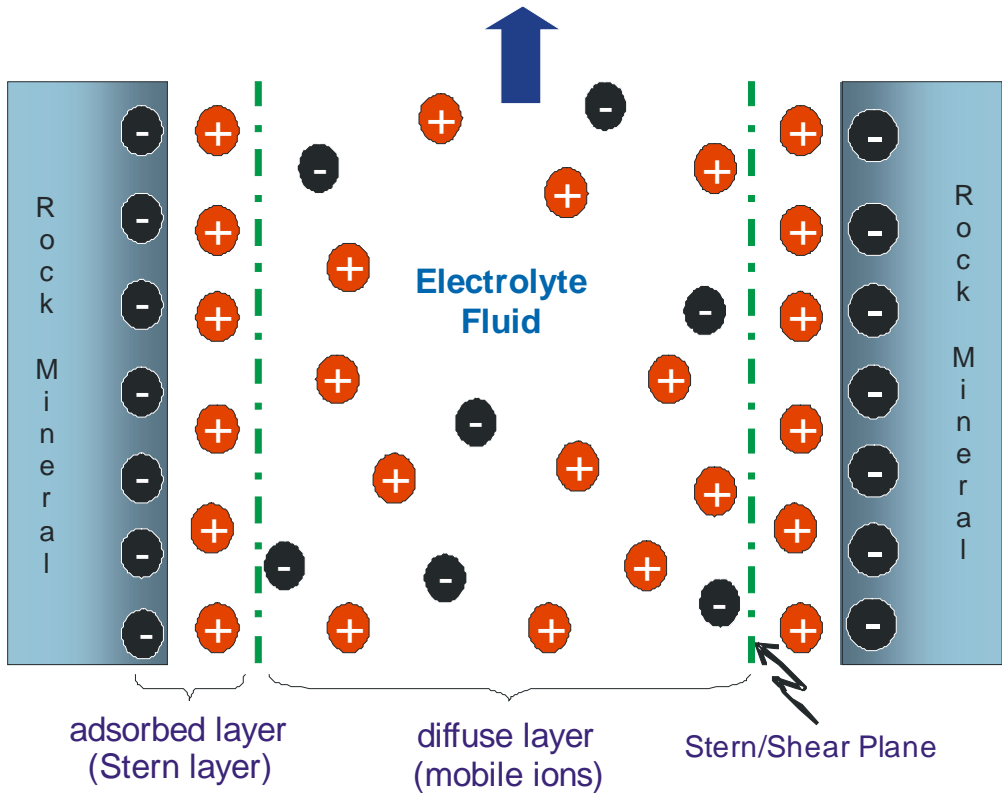


Figure 2.2. A Stern model of the structure of the electric double layer on the rock-fluid interface. Ions within first layer, named adsorbed layer, are immobile, while within a second layer, called diffuse layer, the ions are mobile. Both layers are separated by an imaginary Stern or shear plane where the electrostatic potential will be generated (after Ishido and Mizutani, 1981).

The distribution of ions within the diffuse zone is governed by the Poisson-Boltzmann equation, which accounts for the balance between Coulomb electrostatic and thermal diffusional forces. The electric potential $\psi(x)$ associated with the excess charge of the diffuse double layer can be formulated by a one dimensional Poisson's equation as

$$\frac{d}{dx} \varepsilon(x) \frac{d}{dx} \psi(x) = -\rho(x) \quad 2.1$$

where $\varepsilon(x)$ is the electric permittivity of the liquid (or dielectric constant), and $\rho(x)$ is the excess charge density. Assuming the ionic concentrations within the diffuse layer obeys the Boltzmann formula, the charge density for a symmetric electrolyte (so that $v_+ = v_- = v$ and $n_+^0 = n_-^0 = n^0$) can be defined as

$$\rho(x) = -2e v n^0 \sinh\left(\frac{v e}{kT} \psi(x)\right) \quad 2.2$$

where e is the elementary charge (1.602×10^{-19} C), v is the ionic valence, n^0 is the electrolyte concentrations far from any wall in ions/m³, k is the Boltzmann's constant (1.38×10^{-23} J/K), and T is absolute temperature in degrees Kelvin. The Poisson's equation now becomes

$$\frac{d}{dx} \varepsilon(x) \frac{d}{dx} \psi(x) = 2e v n^0 \sinh\left(\frac{v e}{k T} \psi(x)\right) \quad 2.3$$

which is the well-known Poisson-Boltzmann equation (Pride and Morgan, 1991). The solution to this equation in one dimension (e.g. for a planar interface) is well-known, and yields an electric potential profile $\Psi(x)$ that decays approximately exponentially with distance from the Helmholtz layer. Far from the shear plane, in the bulk pore fluid, the potential and net charge density are essentially zero. The characteristic of electric potential within both layers, Stern and diffuse layer, (as shown at Figure 2.3) drops off roughly linearly in the Stern layer and then exponentially through the diffuse layer, approaching zero at the imaginary boundary of the double layer.

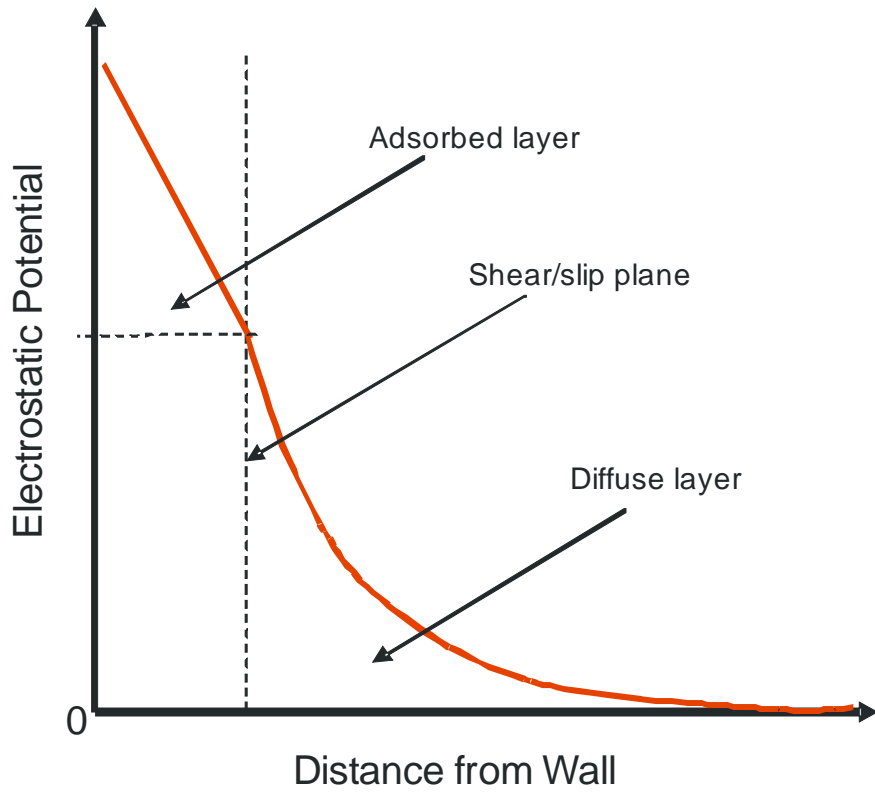


Figure 2.3. Electrostatic potential near a negatively charged mineral grain.

The thickness of the diffuse double layer is often referred to as the Debye length (also sometimes called the ion atmosphere radius), which depends on the concentration of dissolved ions and is the reciprocal of the Debye-Hückel parameter κ :

$$X_{DL} = \kappa^{-1} = \sqrt{\frac{\delta k T}{2 v^2 e^2 n^0}} \quad 2.4$$

where δ , is the dielectric constant, and is equal to 80 for pure water and most dilute solutions. Equation (2.4) (above) shows that the thickness varies inversely with the ionic valence and the square root of the concentration, and directly with the square root of the temperature and the dielectric constant of the liquid. For aqueous solutions at 25 °C and converting the ion concentrations n^0 into molar terms n yields

$$\kappa^{-1} = 2.53 \times 10^9 \sqrt{\frac{1}{v^2 n}} \quad 2.5$$

where n is in mol dm⁻³ and κ^{-1} is in m.

For typical concentrations of aqueous solutions in soils such monovalent electrolytes with concentrations in the range 10^{-3} – 10^{-1} mol/liter, the thickness varies from around 10 to 1 nm. These values are much smaller than pore radii in the majority of rocks and soils with the exception of materials such as clays (Pride and Morgan, 1991).

There is an imaginary surface between the mobile and immobile ions layer called shear/slip plane or Stern plane. The Stern/adsorbed layer (as described before) is considered to be rigidly attached to the mineral surface, while the diffuse layer is not. Moreover, when an external electric field is applied, the solution and the particles on the shear plane move in the opposite directions. As a result, the electrical potential at this shear plane, called the zeta potential, is associated with the mobility of the charges. Greater mobility of the ions within the diffuse zone leads to greater electric potential occurring. Also, as fluid velocity within a diffuse layer increases with distance from the slip plane, a thicker double layer allows for more charge transport, and may result in greater streaming potential. Therefore, rocks with high porosity and permeability may produce stronger electrokinetic responses.

2.3 Zeta and Streaming Potentials

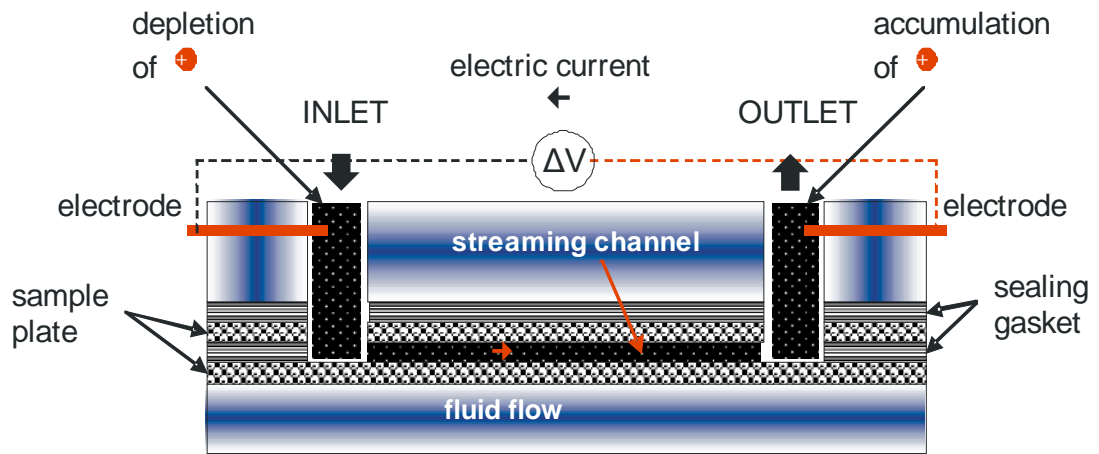
The zeta potential, which is the electric potential at a shear plane, is an important parameter characterizing colloidal dispersion and plays a central role in determining the magnitude of electrokinetic effects. In a rough approximation, the electrophoretic mobility (the ratio of the velocity of particles to the field strength), induced pressure difference in electro-osmosis, streaming potential, and sedimentation potential are proportional to the zeta potential. This potential is a measurable parameter in an electrokinetic analysis and is the potential that determines the electrophoretic mobility μ of particles and colloids as given by the Smoluchowski equation:

$$\mu = \frac{\zeta \varepsilon}{\eta} \quad 2.6$$

where μ is typically expressed in units $\mu\text{m s}^{-1}$ or in V cm^{-1} , ζ is the zeta potential in mV, ε is the liquid electric permittivity, and η is the viscosity in $\text{g cm}^{-1} \text{s}^{-1}$. In earth materials, the zeta potential is usually negative. A typical zeta potential of -10 to -100 mV has been recorded by lab measurements of Ishido and Mizutani (1981), and Morgan et al., (1989). Also values of at least -50 mV are common for quartz when in contact with an electrolyte which was the subject of further investigation of the electrokinetic effect in hydrocarbons (Pride and Morgan, 1991). The most common clays are associated with zeta potentials between 0 and -50 mV, and the lowest magnitudes of potential being associated with high salinities of pore water (Mitchell, 1993).

The streaming potential, on the other hand, is an electrokinetic process that takes place when a pressure gradient exists within the pore fluid. It quantifies an electrokinetic effect that reflects many properties of the (mineral) surfaces: the flow characteristics, surface chemistry, and the thermodynamics of the electrolyte solution. The pressure gradient induces the liquid to flow through a capillary porous medium. Positively charged liquid in the diffuse layer is displaced in the direction of liquid flow and exits one end of the tube, while neutral electrolyte enters the other. As a result, the accumulation of excess positive charge occurs at the outlet, and excess negative charge (as surface charge) at the inlet. Therefore, an electrical potential difference $\Delta\Psi$ known as the streaming potential is generated between the ends of the tube. The streaming potential $\Delta\Psi$ develops an electrical current, which flows in the opposite direction to liquid flow, to neutralize the charge build-up. The charge accumulation ceases and the streaming potential stabilizes when the electrical current developed by the electric field balances the streaming current induced by convection flow of charge in the moving liquid. This phenomenon is shown schematically in Figure 2.4.

(a)



(b)

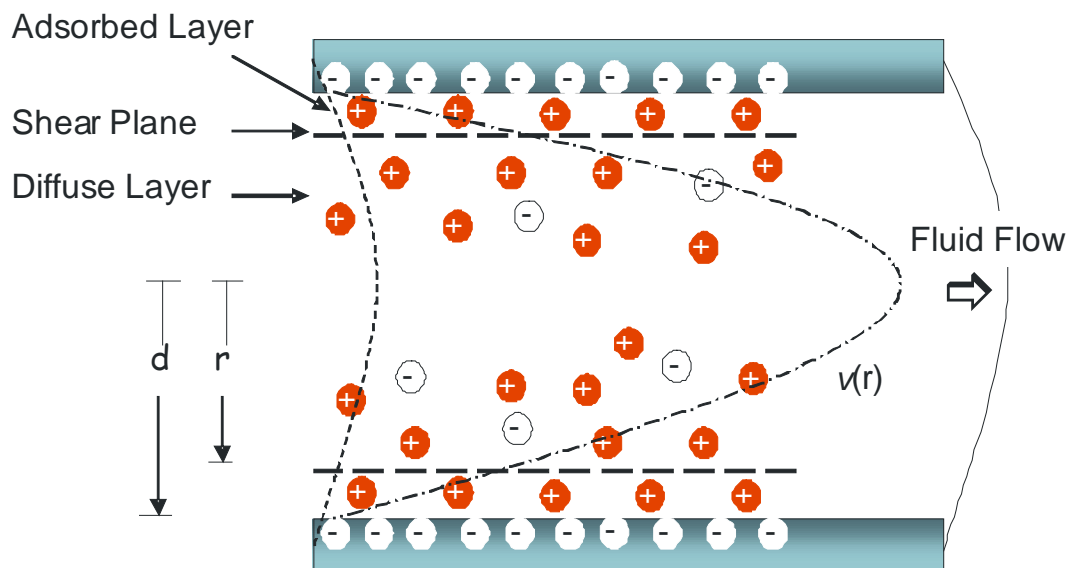


Figure 2.4. (a) Schematic of a chamber for measuring streaming potentials of a solid surface in the laboratory. (b) Cross-section of a capillary tube showing the distribution of excess charge in the electric double layer along the tube wall, and the parabolic velocity curve that is characteristic of laminar (Poiseuille) fluid flow.

As the conduction current is proportional to $\Delta\Psi$ and the streaming current is proportional to ΔP , under steady state fluid flow or equilibrium conditions (when the two currents are equal but in the opposite way) $\Delta\Psi$ must vary linearly with ΔP . The linearity and the constant of proportionality of this relationship can be shown by firstly writing I_c and I_s equations for the conduction current and the streaming current, respectively (Christoforou *et al.*, 1985).

$$I_c = \pi d^2 \sigma_f \frac{\Delta\Psi}{L}, \text{ and} \quad 2.7$$

$$\begin{aligned} I_s &= \int_0^d 2\pi r v(r) q(r) dr \\ &= \int_0^d 2\pi r \left[\frac{(d^2 - r^2)}{4\eta} \frac{\Delta P}{L} \right] q(r) dr \end{aligned} \quad 2.8$$

where σ_f is the fluid conductivity, $q(r)$ is the charge density, L is the length of chamber and $v(r)$ is the velocity of fluid given by Poiseuille's equation for laminar flow of a fluid with viscosity η through a capillary tube of radius d . The assumption of laminar flow is inherent within this equation to provide fluid flow rates that remain low enough to avoid a turbulent flow. The equation (I_c), basically Ohm's law, is dominated by the bulk conductivity of the fluid. Using Poisson's equation to substitute for $q(r)$ and some simplifying assumptions (Fitterman, 1978):

- 1- the flow is laminar
- 2- the conductance of pore fluid is large in comparison to the surface conductance; that means the surface conductivity has no effect
- 3- the radius of curvature of the pore is much larger than the double-layer thickness
- 4- the capillary geometry or parallel plates geometry exists
- 5- no axial concentration gradient occurs in the flow channel
- 6- the flow is in steady state condition ($I_c + I_s = 0$)
- 7- the (mineral) surface has homogenous properties

the correlation between pressure gradient and the measurable streaming potential is obtained as:

$$\zeta = \frac{\Delta\psi}{\Delta P} \frac{\eta}{\varepsilon_f} \frac{L}{A} \frac{1}{R} \quad 2.9a$$

or

$$C_s = \frac{\Delta\psi}{\Delta P} = \frac{\varepsilon_f \zeta}{\eta \sigma_f} \quad 2.9b$$

where ζ is the zeta potential, and ε_f is the electric permittivity of liquid. C_s is the coefficient of streaming potential, $\Delta\Psi$ is the streaming potential, ΔP is the pressure difference across the (capillary) channel, η is the viscosity of the solution, σ_f is the fluid conductivity, L , A , and R are the length, cross-sectional area, and electrical resistance of the channel, respectively. This formula is valid for either seismoelectric or electroseismic phenomenon. This equation is the well-known Helmholtz-Smoluchowski equation for streaming potential (Abramson, 1934; Ishido and Mizutani, 1981; Pride, 1994; and Revil *et al.*, 1996). Examination of equations 2.9a and 2.9b shows that the streaming potential does not depend on the capillary radius or pore size. It is clear that the strength of the electric field depends on properties of the two materials (solid and liquid) and the rate of flow. It also important to note that since ζ is usually negative in the mineral rocks, the potential gradient $\Delta\Psi/L$ is physically in the opposite direction to the pressure gradient $\Delta P/L$. In addition, we can see the linear relationship between the streaming potential $\Delta\Psi$ and the zeta potential, ζ , means that electrical $\Delta\Psi$ and mechanical ΔP coupling is proportional to this potential.

An assumption in equation (2.9a, 2.9b) that the surface conductivity is neglected represents suppression of the conductivity of the diffuse zone with its excess charge. If surface conductivity is incorporated into the conductance of the sample, a correction factor should be added into these equations (2.9a, 2.9b). In the case of a capillary tube the conduction current I_c will be corrected to be proportional to $\pi d^2 \sigma_f + 2\pi d\sigma_s$ rather than the $\pi d^2 \sigma_f$ in equation (2.7). As a result, equation (2.9b) with surface conductance on the grain surface becomes:

$$C_s = \frac{\Delta\psi}{\Delta P} = \frac{\varepsilon_f \zeta}{\eta \left(\sigma_f + \frac{2\sigma_s}{d} \right)} \quad 2.10$$

The appearance of the radius of capillary d in equation (2.10) shows that the pore size now has a role in determining the streaming potential. The role is most significant when the pore size is very small. A small pore size also means that the mobility of ions within the diffuse zone is small, which may lead to less streaming potential $\Delta\psi$. However, the effect of surface conduction in soils and rocks is only partly successfully accounted for by equation (2.10), and is relatively small compared to the observed changes in the streaming potential coefficient (Lorne et al., 1999a, b).

Another approach for reformulating equations (2.7) and (2.8) is modeling the streaming and conduction currents through a porous plug rather than through a single capillary. In this case, the appropriate conductivity to use in equation (2.7) is the bulk conductivity of sample σ_b , which refers to conduction through the fluid, along surface, and the solid grains themselves. In addition, the streaming current in equation (2.8) must be multiplied by two factors: (i) the porosity ϕ to represent the fact that only a fraction of the plug's cross-sectional area is available for fluid-flow, and (ii) an empirical factor c ($0 \leq c \leq 1$), to account for reduced fluid flow due to tortuosity of the pore network. Factor c will be 1 if the pore space consisted of an array of capillaries extending straight across the sample. The formula for the streaming potential across the porous sample is then

$$\frac{\Delta\psi}{\Delta P} = c \phi \frac{\varepsilon_f \zeta}{\eta \sigma_b} \quad 2.11$$

or

$$C_s = \frac{\Delta\psi}{\Delta P} = G \frac{\varepsilon_f \zeta}{\eta \sigma_f} \quad 2.12$$

where

$$G = \frac{F}{F_o} \quad 2.13$$

and F is called the formation factor, and F_o is the bulk formation factor. This equation is the same as that given by Ishido and Mizutani (1981) except they wrote c as a function of tortuosity τ ($c = \frac{1}{\tau^2}$), and σ_b as a function of tortuosity, fluid conductivity, and surface conductivity. The hydraulic tortuosity τ is the dimensionless ratio L_c/L , where L_c represents length of the capillary tube, and L is the length of a typical volume of electrically insulating material (Hillel, 1980). Meanwhile the relation between F and F_o can be formulated in rock conductivity σ_r as (Lorne *et al.*, 1999b)

$$\sigma_r = \frac{\sigma_f}{F} = \frac{\sigma_f}{F_o} + \sigma_s \quad 2.14$$

The quantity $\Delta\Psi/\Delta P$ is sometimes called the coefficient of streaming potential cross-coupling C_s . Laboratory measurements of streaming potential generated by a variety of electrolytes flowing through crushed samples have been done by Morgan *et al.* (1989) and Lorne *et al.* (1999a). Their results indicated that the coupling coefficient for granite, quartzite, K-feldspar, and sandstone samples varied nearly linearly with electrolyte resistivity. In addition, the effect of surface conductivity was relatively small in their samples. Most of Morgan's measurements were made for fluid resistivities in the range of about 5 – 70 Ωm which are typical resistivities for natural surface waters. For 1:1 electrolyte (monovalent ions such as KCl and KNO_3), the ratio of the coupling coefficient to the fluid resistivity was around -4 mV/(atm Ωm). While Lorne's data at higher resistivity (400 Ωm) and pH = 5.7 show that the streaming potential was -40 mV. For a 2:1 electrolyte (divalent cation with monovalent anion such as MgCl_2 and CaCl_2) the ratio was closer to -2 mV/(atm Ωm). An apparent dependence of the streaming potential coefficient with permeability was also observed during deformation by Lorne *et al.* (1999b).

2.4 Macroscopic Electric Fields from Electrokinetic Effects

As described previously, the physical nature of the streaming potential is the generation of excess positive and negative charge zones from pressure gradients. Thus, compressional P-waves may produce regions of excess positive and negative charge when passing through the porous medium due to the pressure gradients from the acoustic wave. The flow of fluid carrying excess charge in the mobile zone of the electric double layer triggers a streaming current. However, this effect does not automatically create a (macroscopic) streaming potential. The charge separation does not change in magnitude as it is carried along with the seismic wave-front in a homogeneous porous medium. In this reference frame the electric field moves with the acoustic wave-front with the charge separation stationary and constant, and there are no net external fields outside of the seismic disturbance. The P-waves produce electric fields internal to the wave that are perpendicular to the wave-front and that drive conduction currents. The existence of fluid flow and streaming current, in a homogeneous material, is not sufficient to generate a streaming potential because the conduction current is exactly balanced by the streaming current. So, the total current is zero and there are no magnetic fields. The local electric field is perpendicular to the seismic wave-front, and is only being observed as the seismic disturbance passes the sensor. This signal, as mentioned globally before, is a non-radiating field and called the Type 1 of electrokinetic effect (Butler, 1996; Haartsen and Pride, 1997). Due to the fact that this signal is contained within and travels with the seismic P-wave, on a multi-channel shot record (with an array of sensors dispersed upon the surface) the apparent velocity of the seismoelectric signal is equal to the velocity of the P-wave.

To calculate the charge accumulation associated with a streaming potential within the mobile zone of electric double layer we can consider an ideal porous plug in which the pores are straight capillaries extending from one end to the other. At one end surface, according to Gauss's Law the surface integral of the net electric flux leaving one of the samples must be equal to the total enclosed charge Q :

$$\oint_S \epsilon \vec{E} \cdot \vec{dS} = \iiint_{V(S)} q dV = Q \quad 2.15$$

If the plug's cross-sectional area A is too large compared to its length L we can neglect the contribution of the fringing field to the total flux in the same way as we neglect the fringing field of a parallel plate capacitor. The equation (2.15) can be simplified as,

$$Q = A (\epsilon_s E_s (1 - \phi) + \epsilon_f E_f \phi) \quad 2.16$$

where ϕ is porosity, and ϵ_s , E_s , ϵ_f , and E_f are the permitivities and electric fields in the solid and fluid components. Due to the boundary condition that the tangential component of the electric field is continuous across a boundary, $E_s = E_f = E$, and since $E = -\Delta\Psi/L$, equation (2.16) can be written as

$$Q = \left(\frac{-\Delta\Psi}{L} \right) A (\epsilon_s (1 - \phi) + \epsilon_f \phi) \quad 2.17$$

From this equation we can see that the charge accumulation Q is proportional to the streaming potential across the sample. In nature, the charge accumulation is caused by the pressure difference across the sample. To obtain the accumulated charge in terms of the pressure gradient $\Delta P/L$ and fundamental material properties we may substitute for $\Delta\Psi$ using equations (2.9) to (2.11). For instance, substitution of (2.11) yields

$$Q = \left(\frac{-\Delta P}{L} \frac{\epsilon_f \zeta}{\eta \sigma_B} \right) c \phi A (\epsilon_s (1 - \phi) + \epsilon_f \phi) \quad 2.18$$

or if we substitute $\Delta\Psi$ into equation (2.10) to see the role of the presence of the capillary radius d , the accumulated charge is

$$Q = \left(\frac{-\Delta P}{L} \frac{\varepsilon_f \zeta}{\eta (\sigma_f + 2 \frac{\sigma_s}{d})} \right) A (\varepsilon_s (1 - \phi) + \varepsilon_f \phi) \quad 2.19$$

From these two equations (2.18 and 2.19) above we note that in the limiting case of zero porosity, the capillary radius d must be zero, and therefore no accumulated charge results ($Q = 0$). This is intuitive as there is no fluid flow or streaming current in the absence of porosity. A similar derivation can be done for a surface enclosing the excess charge to obtain another accumulated charge of equal magnitude but opposite sign at the other end of the sample.

The existence of the fluid flow and the streaming current, as described above does not generate a macroscopic streaming potential. The charge separation that leads to a macroscopic electric field (and the streaming potential detectable outside of the local region) is produced when a steady, streaming current encounters a physical discontinuity. This electric response, called the Type 2 of electrokinetic effect, is created when the acoustic P-wave propagates through a boundary that contains a significant contrast in elastic, electrical/hydraulic conductivity, and/or change in fluid-chemistry properties. The variation in the streaming current, with time, depends upon the time dependence of the pressure gradients of the seismic wave. This time-varying charge separation generates an electrical disturbance that propagates independently of the seismic wave, and diffuses rapidly to the sensors. Thus, the apparent velocity of this type of signal is much faster than any seismic wave. Note that the arrival time of the signal is expected to be at a time equal to one-way seismic travel time to the interface, and nearly simultaneously across an array of widely spaced dipole sensors. This is the signal that may provide direct information about the interface characteristic as the response is sensitive to abrupt changes in permeability. Therefore, these signals may be the most useful in determining hydrogeological properties and the aquifer quality.

The second type of electrokinetic response is generated at the boundary-interface right below the shot point within the first Fresnel zone. To understand why the signal occurs only in a region on the boundary surface right below the shot point, we

consider the following approach by Thompson and Gist (1993). The horizontal resolution is derived from the Fresnel zone. We assume that a spherical acoustic wave hits a horizontal interface with contrast in mechanical or electric properties. On such an interface circular regions of positive and negative displacement develop, moving outward along the interface from a point right below the shot point. These regions are called Fresnel zones of the seismic wave. The first

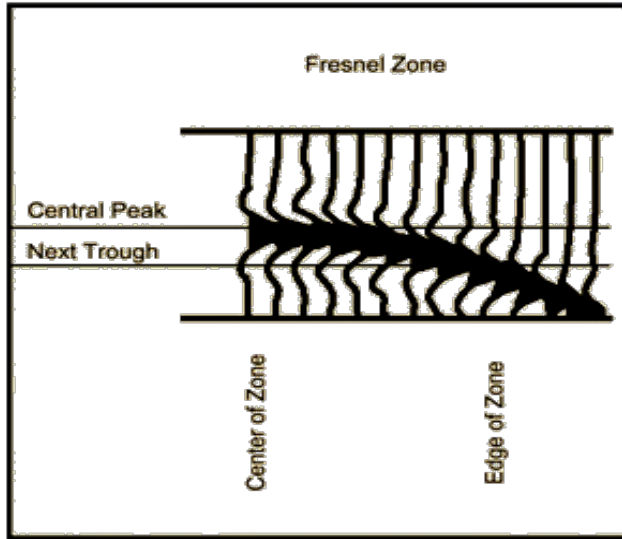


Figure 2.5. Reflection wave contributions within a Fresnel Zone arrive coherently and thus reinforce. Outside peaks and troughs tend to cancel each other and thus make little net contribution. The zone is constructed where the travel paths differ by less than a half wavelength (after Sheriff, 1996).

Fresnel zone is the first circular region of a horizontal layer reached by the seismic waves that are within one-half wavelength from the initial arrival (see Figure 2.5). The first Fresnel Zone is also defined as the area where the waves interfere with each other constructively. The dimensions of the Fresnel Zones can be easily determined by a simple geometry as shown in Figure 2.6.

The seismic wave exhibits successive Fresnel zones at later times. For seismoelectric processes each Fresnel zone acts as an electrical source of EM radiation, which can be represented by an electric multipole. The first Fresnel zone

has dipole symmetry. Then the electric octupole is the next lowest order of multipole created when the first and second Fresnel zones are the same area. The electric field from sources of successive Fresnel zones falls off with distance r as $1/r^5$ and $1/r^3$ from an octupole and a dipole, respectively. Thus, the electric field from the higher-order Fresnel zones can be neglected compared to that from the first Fresnel zone due to the rapidly diminishing amplitude with distance of higher order zones, and we can approximate the behavior of the total of the Fresnel zones as a dipole. In calculating the surface fields we may then assume that the source of the EM radiation is a vertical electrical dipole corresponding to the first Fresnel zone below the shotpoint.

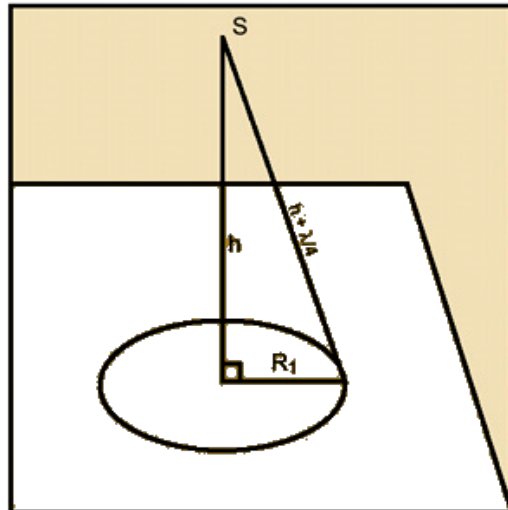


Figure 2.6. Using a simple Pythagorean theorem to calculate the radius of the Fresnel Zone for two-way travel time (after Sheriff, 1996).

The phenomenon of electric field creation from the first Fresnel zone can also be seen from a different way. We assume that each successive Fresnel zone contributes to the EM signal with an alternate phase. Each term increases the degree of cancellation that occurs to the potential at the surface at finite offset, and a sharply peaked potential focused around the shot point results. Therefore, the seismoelectric conversion can be recognized by two important facts: the arrival at all receivers

which is approximately simultaneous, and the strong decay of pulse amplitudes with increasing offset from the shot point as well as with increasing time (depth). The main and decisive factor in the argument used here is that the seismic wave velocity is much slower than the electromagnetic disturbance/wave speed. Therefore, non-ephemeral conversions from seismic waves to electromagnetic waves occur only for very small angles of incidence. In other words, the non-evanescent reflections from seismic waves to electromagnetic waves occur below the shotpoint only.

As the electrokinetic effect is a seismic-to-electric coupling mechanism, the general theory of coupled flows provides a framework for the study of streaming potentials in the Earth. Following the development presented by Fitterman (1978) and Sill (1983) the origin of the streaming potentials can be investigated. The cross-coupled equation relating current flow to fluid flow can be simplified as

$$\begin{bmatrix} \mathbf{J}_e \\ \mathbf{J}_f \end{bmatrix} = \begin{bmatrix} L_{11} & L_{12} \\ L_{21} & L_{22} \end{bmatrix} \begin{bmatrix} -\nabla \Phi \\ -\nabla P \end{bmatrix} \quad 2.20$$

where \mathbf{J}_e is the current density, \mathbf{J}_f is the fluid flow, Φ is the electric potential, P is the fluid pressure that can cause fluid flow, and L_{ij} are generalized conductivities. In an electrokinetic system L_{11} is the electrical conductivity of medium σ from Ohm's law, and L_{22} is the hydraulic mobility K from Darcy's law ($K = k/\eta$ where k is permeability and η is viscosity). The ratio L_{12}/L_{11} is the streaming potential coefficients C_s , and L_{21}/L_{22} is the electro-osmotic coefficient. By Onsager's reciprocal relationship the L_{ij} must be equal to L_{ji} (let $L_{ij} = L_{ji} = \chi$) in order to maintain time reversal invariance. The equation (2.20) may be re-written as

$$\mathbf{J}_e = -\sigma \nabla \Phi - \chi \nabla P = -\sigma (\nabla \Phi + C_s \nabla P) \quad 2.21a$$

$$\mathbf{J}_f = -\chi \nabla \Phi - K \nabla P \quad 2.21b$$

Since the total electric potential (or streaming potential) is defined

$$\Psi = \Phi + C_s P \quad 2.22$$

and the electric current flow is given by

$$\mathbf{J}_e = -\sigma \nabla \Psi \quad 2.23$$

in the absence of current source and conditions of steady (dc) flow,

$$\nabla \cdot \mathbf{J}_e = 0 \quad 2.24$$

and then for homogeneous media,

$$\nabla^2 \Psi = 0 \quad 2.25$$

Sources for streaming potential Ψ , therefore, can only occur at interfaces. The streaming potential sources can then be seen from following description. As we assume there are no external electric field sources, the primary driving force is a fluid pressure gradient. In addition, the influence of the induced potential gradient $\nabla \Phi$ on fluid flow is also small. Hence the first term in equation (2.21b) can be neglected. The fluid flow equation is therefore decoupled and reduces to

$$\mathbf{J}_f = -K \nabla P \quad 2.26$$

As the electric current J_e seems to be the sum of a streaming current and a conduction current, the equation (2.21a) can be modified as

$$\mathbf{J}_e = \mathbf{J}_{e,st} + \mathbf{J}_{e,cond} \quad 2.27$$

where

$$\mathbf{J}_{e,st} = -\chi \nabla P \quad 2.28$$

and

$$\mathbf{J}_{e,cond} = -\sigma \nabla \Phi \quad 2.29$$

Conditions within equation (2.24) break J_e into its streaming and conduction current components,

$$\nabla \cdot \mathbf{J}_{e,cond} = -\nabla \cdot \mathbf{J}_{e,st} \quad 2.30$$

and substituting the equation (2.28) into equation (2.30),

$$\begin{aligned}\nabla \cdot \mathbf{J}_{e_cond} &= \nabla \cdot (\chi \nabla P) \\ &= \nabla \chi \cdot \nabla P + \chi \nabla^2 P\end{aligned}\quad 2.31$$

Finally, substituting equation (2.26) into equation (2.31) to replace $\nabla^2 P$ and yields

$$\nabla \cdot \mathbf{J}_{e_cond} = \nabla \chi \cdot \nabla P - \frac{\chi}{K^2} \nabla K \cdot \mathbf{J}_f - \frac{\chi}{K} \nabla \cdot \mathbf{J}_f \quad 2.32$$

The equation (2.32) above shows that the conduction current is generated from three different sources in steady fluid flow conditions. According to equation (2.30), the term in equation (2.32) is also the source for the streaming current. Therefore, the streaming potentials are created by:

- 1- fluid flow perpendicular to an interface where the coupling coefficient χ changes;
- 2- fluid flow perpendicular to an interface where the hydraulic mobility K changes; and,
- 3- sources or sinks of fluid.

However, the above analysis is focused on the condition that a streaming potential is generated by steady fluid flow. When the seismic wave exists can the equation (2.32) be used? The existence of seismic waves that induce fluid flow can be accommodated if we assume that the equation also approximately holds for the fluid flows that vary in time. A fourth source of streaming potentials then can be expected. If there is a compressional P-wave, a relative flow between the solid rock and electrolyte fluid occurs and hence $\nabla \cdot \mathbf{J}_f \neq 0$. Thus, when the seismic waves are passing the media, the third term on the right hand side of equation (2.32) is non-zero and streaming potentials may exist even in homogeneous media.

To sum up the analysis above, within porous rocks containing fluid the compressional seismic P-wave produces regions of excess positive and negative charge parallel to the seismic wavefronts. The electric fields are generated and then observed when (a) the seismic wavefronts pass a receiver, and (b) the spherical symmetry of the charged wavefronts is broken by an interface or other

heterogeneity. The first type of electric field accompanies and travels in a homogeneous medium at the same velocity as the seismic wave, while the second type of electric fields, which generates a macroscopic streaming potential, occurs in layered media. This EM disturbance diffuses rapidly to the antennas which record a simultaneous arrival time. The schematic illustration of both types of the seismoelectric responses can be seen in Figure 2.7 below. It was predicted by a conceptual model developed by Butler et al. (1996) and verified by numerical simulations by Haartsen and Pride (1997).

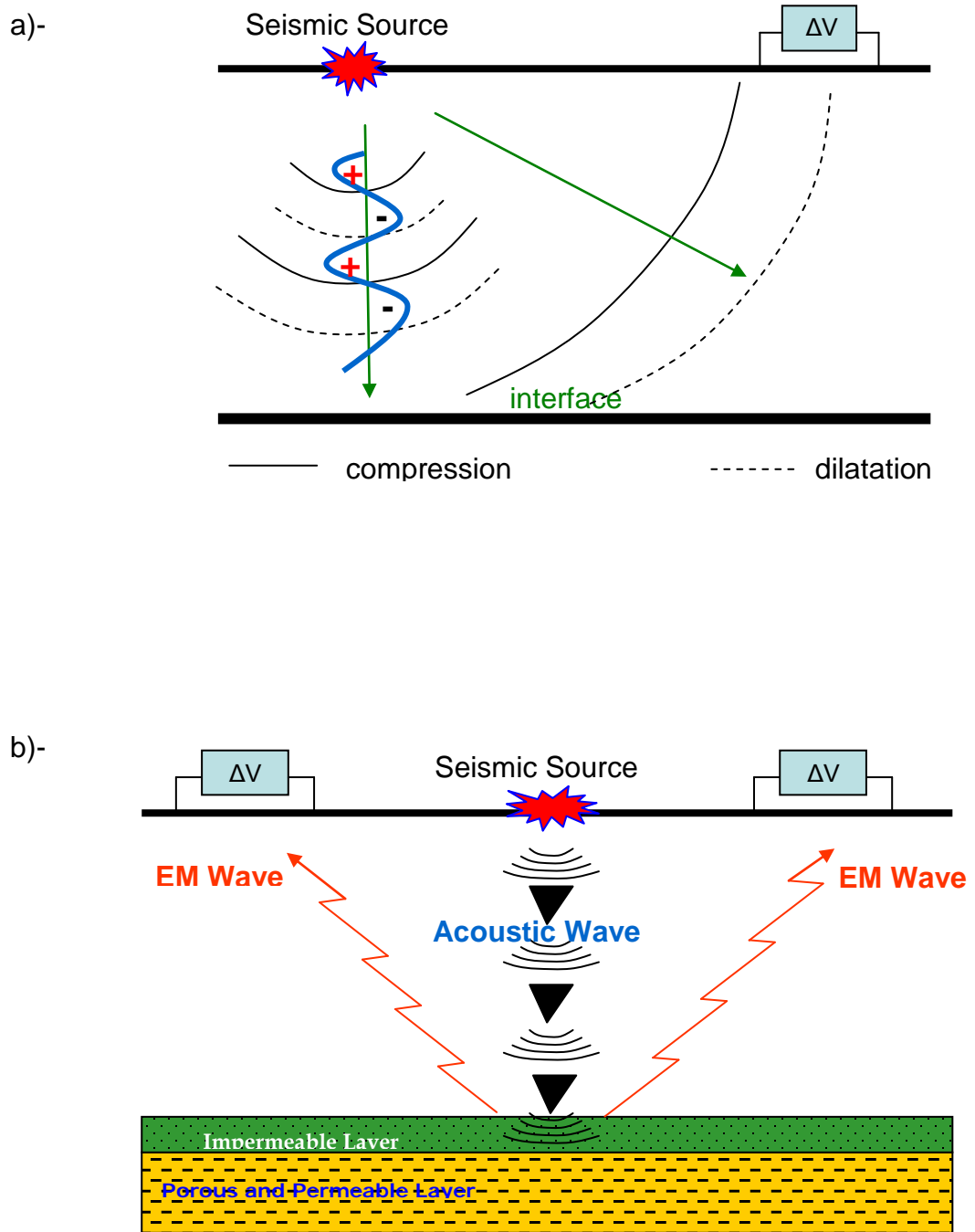


Figure 2.7. Two types of seismoelectric response seen in experiments
a) Type 1 in homogeneous media. The electric fields are detected when the seismic waves pass the dipole sensors; b) Type 2 is a rapidly diffusing electric field generated at an interface, travels at EM wave velocity and is detectable essentially simultaneously by widely separated antennas (after Butler *et al.*, 1996; and Haartsen and Pride, 1997).

CHAPTER 3

ACQUISITION METHODOLOGY

3.1 Introduction

The seismoelectric method is not an established geophysical technique, such as seismic refraction/reflection and electromagnetic methods that have specific instrumentation and standardized field methodology for making field measurements. Even though the seismoelectric method has been postulated since 1930s (as described in Chapter 1), commercially available specific instruments and standardized field methods for making seismoelectric measurements are still unavailable.

The electric signals recorded in seismoelectric records are presented in a manner very similar to conventional seismic recording. However, the measurement of very small seismoelectric signals in the presence of cultural noise that is usually much greater in amplitude is difficult. Therefore, the acquisition of seismoelectric data either requires carefully designed instrumentation, or careful use and modification of existing instruments. Standard seismic acquisition systems provide the best ready-made solution. They are multi-channel data acquisition systems that have a large dynamic range and have many features needed for collecting seismoelectric data. Thus, seismographs are our main instrument used to collect the electrokinetic data.

The principal challenge in acquiring seismoelectric/electrokinetic data is to obtain data with sufficient signal-to-noise ratio, and to minimize acquisition artifacts. Minimizing of acquisition noise is extremely important as special care is needed to ensure that measurement procedures do not introduce transient effects that could obscure the true signals, or be mistaken for the true signals. This chapter explains the instrumentation I used to make field measurements, the types of noise that have influenced data, and field methods used to reduce the noise and to enhance seismoelectric responses.

3.2 Instrumentation

3.2.1 Overview

The field instrumentation used in my tests consisted of a 48-channel seismograph (OYO DAS1 or Bison 9000) equipped with roll box, CDP cables and single cables, seismic source, geophones, pre-amplifiers, and grounded dipole antennas. In order to minimize the electrical noise produced by portable generators, the instruments were battery-powered.

Geophones were used to detect the seismic response at the earth's surface. The geophones were conventional vertical component, similar to those used for land oil exploration surveys. To achieve strong and reasonable mechanical coupling of primary waves (P-waves), the geophone's spike was driven several centimeters into the ground in a vertical orientation. The geophones were a critically damped system with a resonant frequency of 28 Hz.

To detect the electrokinetic signals (arising from subsurface interfaces when seismic waves hit significant physical properties changes in the medium) an array of electrode stakes (dipoles) was set into the earth. The electric field sensors consisted of a 24 grounded dipole array, each consisting of a pair of 50 cm long stainless steel stakes. Electrical signals from each dipole are transmitted to a battery-powered differential preamplifier box via single-wire leads. The preamplifiers, which were designed by Dr. Anton Kepic (Curtin University, Perth), provide high input impedance (20 M Ω differential), a maximum electronic gain of 30 times, and a bandwidth frequency of 2 Hz to 30 kHz. The preamplifier boxes were located approximately half-way between the dipole stakes. Note that this is different from the typical seismic survey configuration where the geophone signals are simply connected by wires to the seismograph (via multi-channel cables). The amplified signals are then transmitted along conventional reflection (CDP) seismic cable to the recorder.

Seismic and seismoelectric data from sensors were transmitted along seismic reflection cables to the seismograph. The seismic cables used for the OYO DAS-1 were heavy 96 pair CDP cables with 10 m take-outs. In contrast, relatively light 24

pair cables were used for the Bison instrument with 5 m take-outs. However, the electrical performances of the cables used with the DAS-1 were superior in terms of cross-talk and noise pick-up (Kepic and Rosid, 2004). The two systems were used independently at different sites so a direct comparison is not available. The Bison seismic acquisition system (and its seismic cable especially) was simpler and more convenient to use in the field than the OYO. In field measurement, however, the seismic cables (especially in seismoelectric acquisition) were extended independently and placed as far away as possible from the electrode arrays to avoid electrical cross-communication. The cables were used for both seismic and seismoelectric data acquisition, but not simultaneously to prevent cross-talk from the much stronger geophone signals. In addition, the seismograph was typically located more than 15 m away from the dipole array to reduce any effects from radiofrequency and other electrical noise from the computer system. The data were recorded and saved in the seismograph's computer within the OYO DAS-1 system, and saved separately via a cable link to a laptop for the Bison seismograph system.

In general, the seismoelectric data is recorded from signals from the dipole array with up to 24 channels of data. The sampling rate was set to 0.1 – 0.25 ms and the number of samples set so that a record length 300 – 1000 ms resulted. The sampling rate was set to capture the highest frequencies of the seismoelectric signals, which are usually in the range of 500–1000 Hz. Acquisition band-pass filters were normally set from 4 Hz to 2 kHz in the seismograph in order to capture the widest range of amplitudes and frequency content in the anticipation that further filtering can be done later numerically.

3.2.2 Seismic Sources

Seismoelectric signals are directly, and linearly, related to the seismic waves generated by the seismic source. The seismoelectric response is generated by relative motion between the solid and liquid phases in porous media, which happens under the compression and rarefaction accompanying the seismic P-wave. Thus, seismoelectric signal properties, such as frequency content and amplitude, are strongly dependent upon seismic source characteristics. Our experiments rely on the

generation of seismic compressional waves (P-waves) rather than shear waves (S-waves). Electrokinetic theory predicts that electrokinetic effects are induced by compressional waves. Thus, a hammer (or explosive) is a suitable source as most of the body waves generated by vertical impact are P-waves. However, a significant portion of the impact energy is converted into Rayleigh waves, which provide interference. S-waves produce very weak magnetic fields in theory (Pride and Haartsen, 1996), probably too weak to detect and so we did not pursue this path of investigation. Instead, our measurements concentrated on detecting the electric fields produced when seismic waves pass through a boundary and generate electromagnetic waves.

There are many types of seismic energy sources available to use for shallow seismic studies, such as: sledgehammer, weight drop, blasting caps/explosive, rifle and shotgun, buffalo gun, and MiniSOSIE (Steebles and Miller, 1990). To select from the array of possible sources, field factors such as cost, repeatability, spectral characteristics, convenience and efficiency, amount of energy needed, and safety, need to be considered when we select a source of impact. Steebles and Miller (1990) who have successfully used sledgehammer, blasting caps, buffalo guns and rifles for shallow seismic surveys in the range of depth of 15 to 45 m, discuss the relative merits of these sources, but there is no clear winner. In our surveys, a sledgehammer provided the main source of seismic excitation (with small explosives used in one field experiment) because it is convenient, reliable, provides sufficient energy when stacked, and has no regulatory restrictions. The sledgehammer was swung onto a plastic-aluminum base plate. The base plate was constructed with a hard plastic disc implanted in the middle of a thick aluminum metal slab. This design was found to efficiently couple the impact into seismic P-waves and avoids metal impacting upon metal, which can result in electrical noise (Butler et al., 1996).

A sledgehammer struck against a metal plate on the ground is often used as a P-wave energy source, as seismic instruments designed specifically for shallow-target studies have been produced to use such sources since the mid-1950's (Yilmaz, 2001). Even though the sledgehammer is inexpensive, relatively safe, and easily moved along the survey line, it does not impart much energy to the ground. In order to obtain a better signal-to-noise ratio in the seismoelectric record, we stacked as

many hammer blows as could reasonably be demanded from the hammer operator; typically, 20 impacts of a 7 kg hammer. Further stacking requires a change in operator or a brief rest. Most of the seismoelectric data is derived from a stack of 50 to 100 impacts. The repeatability of the source is important in order to enhance the signals which are in-phase (seismic related) and similar in spectral characteristic. If many impacts are stacked then there is the possibility of a large random noise event corrupting the record. Thus, a balance was struck between the number of impacts to produce a shot record and the number of repeat experiments (to produce a shot record comparison for repeatability).

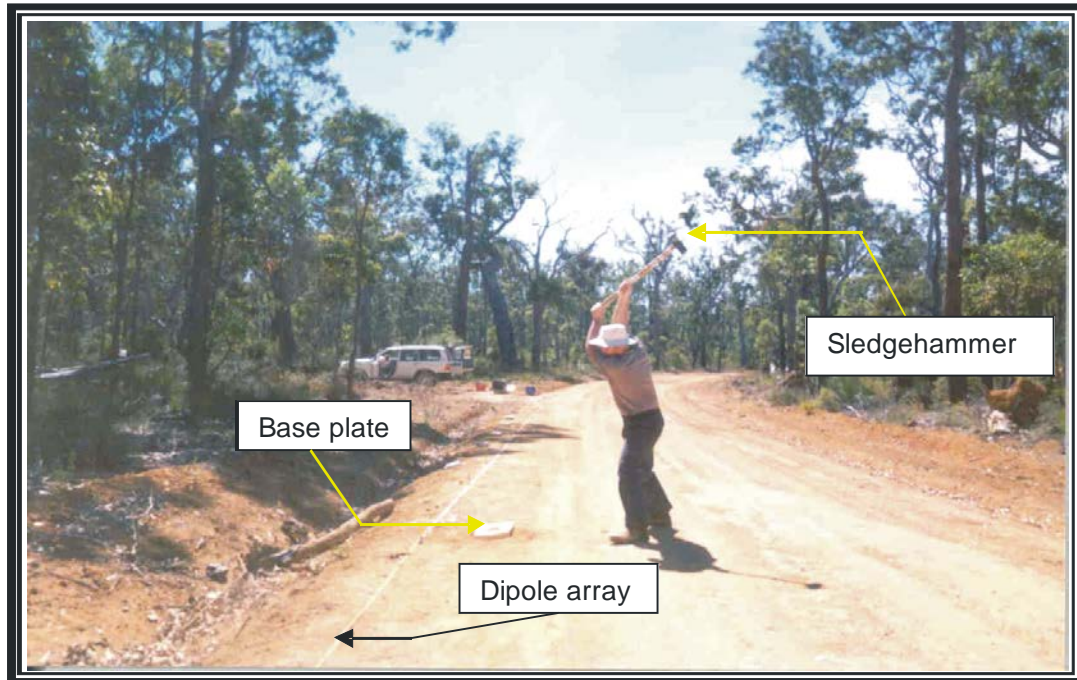


Figure 3.1. The source of seismic excitation in the Nannup measurements is a sledgehammer that swung onto an aluminum base plate. Each seismoelectric record resulted from stacking 50 blows of hammer, and 15 blows for seismic data.

A conventional zero-delay method to trigger the seismograph was used to produce records when the hammer impacted upon the base plate. Triggering was signaled by a small piezoelectric accelerometer mounted on the hammer. The accelerometer, made from a piezoceramic audio transducer set in epoxy, had a resonant frequency

in the range of 1–5 kHz and acted as impact detector. The electrical signal was transmitted along a simple two wire cable up to the seismograph (with one end taped to the sledgehammer). To avoid interference and cross-talk with seismoelectric signals the trigger cable was placed away from both the seismic cable and the array of dipoles. The trigger times within the shot record were set on either 0 ms (for the Bison seismograph) or 10 or 50 ms (for OYO DAS-1). Pre-trigger information was required for data processing and noise analysis, mainly to assist in removing harmonic noise from the data records.

An explosive seismic source was used in only one experiment, at Nambi station near Leonora. This high-energy source was used to produce both seismic and seismoelectric records over an expected deep layer target with a wide spread of 48 geophones and 16 dipoles. It was the first seismoelectric experiment with Curtin University equipment. The explosive was a single 100-gram booster (high velocity pentolite) that was detonated in a shallow hole augered to depths between 0.5 and 1 m. Deeper holes would have been more desirable in order to properly contain the blast, but the depth of the hole was often limited by the presence of a cemented calcrete/ferricrete layer. The material above this layer was principally weakly cemented sand. This material did not contain the blast very well despite the addition of water, and it appears that much of the energy went into surface waves rather than P-waves (see Figure 3.2).

The large initiation current associated with conventional electric detonators can contaminate the seismoelectric records at the time of detonation. So, instead of using conventional zero-delay caps or seismic caps we used fuse caps or electrical delay caps to separate in time the initiation and the blast. During blasting, the data acquisition (seismograph) was triggered by the flash of light that accompanied cap detonation. This flash was transmitted to the seismograph by a fiber optic cable in order to minimize blasting-related noise. The plastic optic fiber was inserted into the explosive package to detect the onset of the blast. Kepic and Russell (1996) reported that this method of triggering is reliable and accurate. In addition, the method does not produce the electromagnetic noise associated with other triggering methods that rely on the termination or production of an electrical current at the time

of detonation. Consequently, the method electrically isolates the recording equipment from the ionizing blast plasma.



Figure 3.2. A shallow shot (80 cm deep) is blowing out at the Nambi survey. The explosive was a single 100 g booster (high velocity pentolite). This source was used to collect both seismic and seismoelectric data that were acquired simultaneously using two different seismographs located separately.

The explosive source, in the single field trial it was tested (the Nambi test site), produced a preponderance of guided waves and multiples; thus, producing uninterpretable data. The geological conditions, with a thick high velocity layer above the target, were conducive for this to happen, and it is debatable whether another source would have been better. However, the high frequency content of seismic waves produced by an explosive may have made the problem worse.

As in seismic surveys guided waves can appear in seismoelectric data as an interface wave trapped within a layer that propagates in the horizontal direction with a characteristic velocity. This wave often occurs in shallow seismic reflection data where there is a geological setting with hard bottom (e.g. shallow marine records in areas with a large contrast in impedance near the water bottom). The near-surface geology in the Nambi test area consisted of unconsolidated red earth and/or red colluvial gravel or sand and silts on the surface overlaying a well consolidated ferricrete layer (see Figure 5.1). This situation is similar to the water layer of sea which makes a strong velocity contrast with a hard substratum, or is the inverse (in a seismic impedance sense) to the example of coal seams where a low velocity layer is sandwiched between high-velocity layers, as most of the energy is trapped within and guided laterally through the low-velocity layer. In the case of tests at Nambi, and to lesser degree at the Nannup test area, there were high velocity layers near the surface that trapped some of the seismic energy as guided waves. The lateritic weathering profile in these areas often forms hard layers from groundwater precipitating minerals that cement the unconsolidated matrix to form calcretes, silcretes and ferricretes. In addition, the phenomenon is more trapping the seismic energy as guided waves rather than absorption and attenuation energy due to high frequency of seismic waves.

Guided waves will occur if conditions are right no matter what source is used as the physical properties of the geology determine whether there is a condition for energy trapping. However, the relative amount of energy within the guided wave versus the propagating P-wave does depend upon the location of the source and the source energy spectrum. The resonant nature of the trapped energy means that certain frequencies are more likely to be trapped and a source rich in high frequencies may have a greater proportion of energy in this undesirable mode. Additionally, if the impact point of the source is on the boundary between the contrasting layers then there will also be a greater proportion of energy trapped within the wave-guide. The tests at the Nambi test site managed to combine the worst of both of these conditions as the explosive is rich in high frequencies that propagate well in the ferricrete in that area, and the explosive was placed upon the ferricrete as the auger drill would go no further into the ground. In hindsight a hammer impacting upon a plate on the near surface would have put a greater amount of energy into the desired modes of

seismic propagation. However, a hammer source is not likely to be the solution as the use of a hammer source did not prevent guided waves from dominating the seismoelectric records in other areas with laterite geology (for example some test locations in the Nannup test area).

3.2.3 Pre-Amplifier and Grounded Dipole Sensors

A simple means to detect seismoelectric signals is to use a pair of metal stakes driven into the ground to form a grounded dipole sensor and a differential pre-amplifier to amplify and buffer the signal. A grounded dipole sensor measures the difference in electric potential between two points in the earth, and the average electric field can be inferred from this potential difference and the length of the dipole. Almost without exception, the seismoelectric sensors used in my field studies were grounded dipoles. The dipoles, which were set to record vertical electrical fields, are made from a pair of 50 cm stainless-steel electrodes. The stakes were driven 30–40 cm into the ground, to ensure good electrical contact between the stakes and ground, and water was often poured near the stakes to further reduce contact resistance. Stakes were then paired to form 5–6 m dipoles to achieve a sufficient potential difference from the small electric fields resulting from electrokinetic effects. The grounded dipole was chosen over a radio antenna style arrangement (such as a long wire antenna which some researchers have used) because we are interested in frequencies below 1 kHz and an arrangement that minimizes AM radio signal content is preferable. Even though the seismoelectric response diffuses as an EM wave only the electric field component was measured as it is predicted to be much easier to detect than magnetic fields (Pride and Haartsen, 1996; Russell et al., 1997; and Garambois and Dietrich, 2001). Significant magnetic fields are expected to be accompanied by the shear waves (Pride and Haartsen, 1996; and Garambois and Dietrich, 2001).

Every dipole was connected, via wire leads, to a battery-powered differential preamplifier. Much consideration went into the design and application of the preamplifier electronics as the electrokinetic signal amplitudes were expected to be millivolts to sub microvolts in magnitude, and the measurement of such signals in

the presence of cultural interference that is often greater in magnitude was expected to be challenging. Connecting the dipole stakes directly to the seismograph was not seriously considered as this would likely result in noisy data due to poor magnetic noise immunity (from relatively high sensor source impedance) and an unpredictable frequency response from capacitive loading of the dipole by stray capacitance within the seismic cable (Kepic and Butler, 2002).

The pre-amplifier design used in my field tests provided very low intrinsic noise (less than 80 nV rms of noise over an acquisition bandwidth of 500 Hz), high input impedance (20 MegaOhm), and high radio-frequency interference immunity (better than 60 dB attenuation before amplification) with a moderate gain of either 10 or 30 (selected by jumper on the circuit board). These qualities are essential to cope with the varied conditions encountered in field surveys. A passive band-pass filter (using three RLC stages) to reject very low and very high frequencies was placed before the active electronics (the components of the circuit that need power to operate – containing BJT and FET transistors) in order to capture signals in the seismic frequency range, 10 Hz to 1000 Hz. The necessity of removing very high frequencies before the active parts of the circuit became apparent when early field tests demonstrated that measuring electric fields without the preamplifier produced records severely contaminated with either AM or FM radio broadcast signals. This behavior was not unexpected as both Kepic (1995) and Butler (1996) have seen this behavior and provided a similar remedy. However, modern seismographs tout the use of delta-sigma analog converters that sample the signal at several mega-samples per second (at low resolution), thus, requiring a much simpler anti-alias filter. The field tests demonstrated that these devices are just as prone to radio frequency interference as older devices despite the high sampling rates.

In order to achieve an accurate measurement the preamplifier's input impedance must be significantly higher than the resistance between the electrodes. In the field, the contact resistances of ground stakes depend on the soil type and its moisture content. In our field trials we found that the grounded dipole contact resistance was often greater than 10 kOhm when the surface soils were very dry (e.g. summer season measurements), which added another 300 nV rms of noise due to the Johnson (thermal) noise from the extra series resistance. On rare occasions we found dipoles

with very high contact resistances of several MOhms. However, as most of our surveys were done in winter, contact resistances measured before acquisition were principally in the range of a few hundred Ohms to few kOhms. The preamplifier with its 20 MOhm input impedance was designed to anticipate the highly resistive conditions often encountered.

Although the pre-amplifier was well designed in many respects it was not without fault. The biggest problem encountered was unstable behavior, or positive feed-back causing oscillation. Often a faulty channel would affect its neighbors, even the whole array, due to the sharing of ground stakes between neighboring amplifiers. The problem appears if there is a high contact resistance of a dipole and poor cabling (such as the input wires crossing over the seismic trunk cable). These conditions tend to lead to positive feed-back into the preamplifier system. In resistive conditions and with poor quality seismic cable (such as the cable we used with the Bison system) even careful cable layout could not always guarantee a working arrangement at first. The high resistance may be due to either improper connection between dipole stakes and the ground or between dipole stakes and wire cables. Diagnosing the problem is also difficult as the oscillations cannot be directly seen in the seismic records as the oscillations are more than 100 kHz in frequency. However, unusual low frequency behavior (aliased noise) is diagnostic of the condition. Solving this problem proved time consuming (some times requiring two hours of testing) as only a few amplifiers out of twenty four are the cause, but often a particular pair of amplifiers would not work together.

A setup and testing strategy was devised to minimize the disruption caused by the feed-back problem. Firstly, the background noise level of each channel is checked one by one (i.e. only one pre-amplifier is powered on at a time) in order to find the defective channels. We then look for the main cause of the problem; either from poor contact between stakes and ground, or a bad connection between stakes and wire leads, or a defective preamplifier (low battery, broken leads, etc). To remedy the problem of high contact resistance we can pour sufficient water into the ground in the vicinity of the dipole stakes to lower resistance, or move the stakes into a lower resistance area, or exchange the stakes with buried aluminum foil. We may also check the quality of the connection of wire cables to stakes and the operation of

the pre-amplifier. Other solutions are to change the gain to 10 (less gain means less coupling back into the pre-amplifier inputs) as well as to place the input cable well away from the output cable to avoid the cross-communication problems.

3.3 Noise

3.3.1 Seismic Related Noise

According to Dobrin and Savit (1988), in the context of seismic prospecting, noise is defined as spurious seismic signals from ground motion, which are not associated with reflections. Analogous to this definition with respect to seismoelectric measurements noise is any electrical signal unrelated to those from geological interfaces of interest that can obscure or completely overwhelm seismoelectric signals. The work in this thesis regards the seismoelectric signals that arise when the P-wave crosses a boundary (the first time) as the signal. This is the Type 2 seismoelectric signal mentioned in Chapter 2. There are two main types of noise: electrical noise that is associated with seismic waves, and that not associated with the seismic wave (mostly due to external electromagnetic fields). Type 1 signals are considered to be seismic-related noise as these are not used for interpretation in this thesis (although they do contain information about the earth and could be signals for other purposes).

The principal types of seismoelectric noise produced by the seismic source are associated with surface and near-surface waves, scattered or incoherent noise, multiple reflections and head waves. Effects from surface waves are the most visible artifact in shot records and consist of electric fields that are produced by ground roll/Rayleigh waves. Effects from direct P-waves as well as guided and multiple waves are often visibly apparent as well, but nearly every seismoelectric shot record clearly contains electrical signals that are ground roll-related (see Figure 3.3 for an example). Type 2 electrokinetic responses appear as simultaneous signals, but are rarely visible without further signal processing to remove the ground roll related signals as well as other electrical signals associated with refraction, and direct P-waves. So, for quality control of data in the field, the presence of the undesirable Type 1 signals is at least diagnostic that the acquisition system is

functioning as we have found it very difficult to see directly the Type 2 signals within the records.

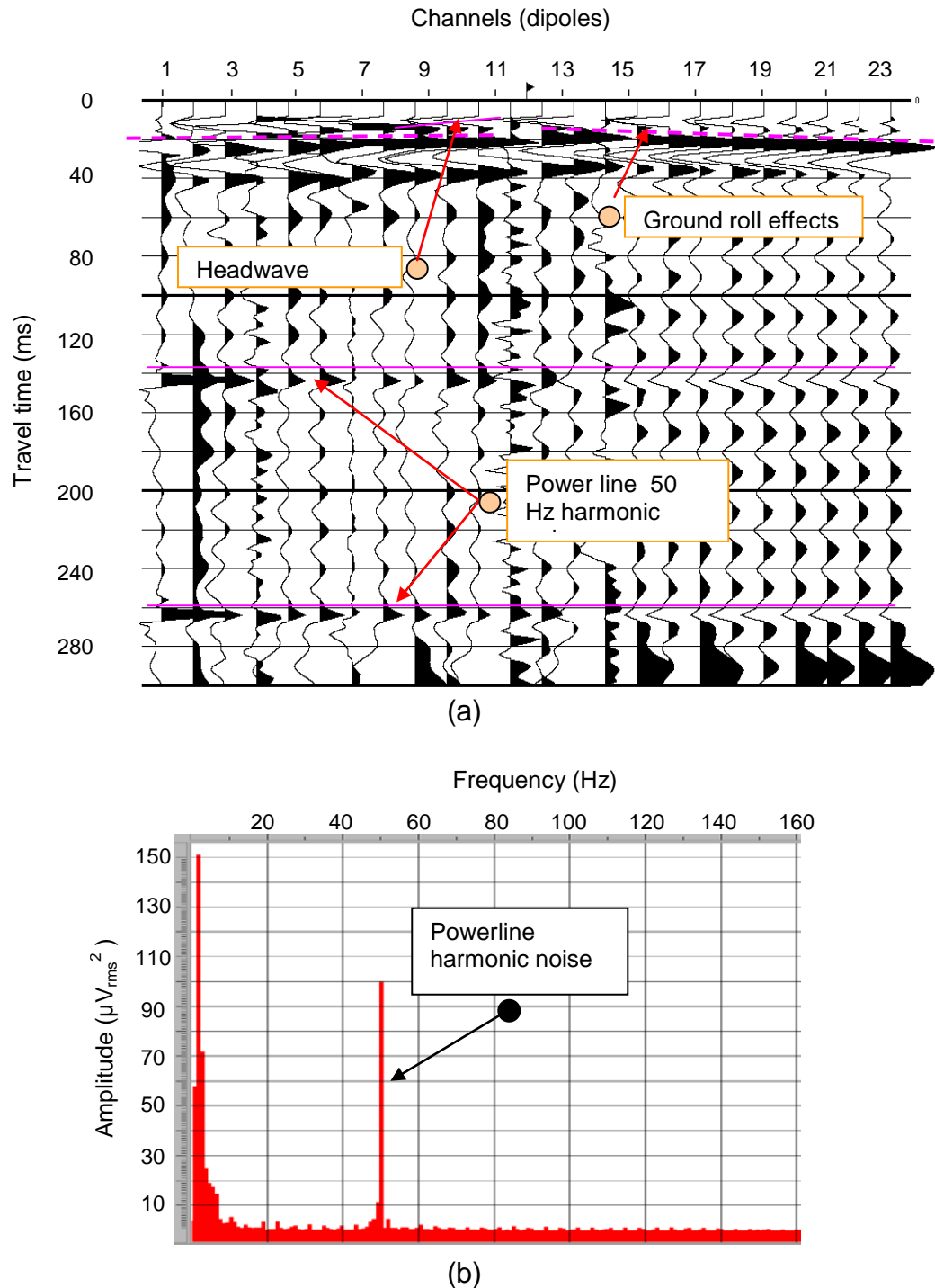


Figure 3.3. (a). Coherent noise in a Lake Bryde seismoelectric shot record. The noises sources are ground roll and head waves and power line harmonic noise. (b). The power spectrum shows the 50 Hz power line noise characterized in the time domain by reversal polarity on opposite sides of the shot-point (shown in part a).

Multiple reflection associated signals (multiples) are secondary reflections, often associated with interbed or intrabed ray paths. This noise looks so similar to the primary reflection that we may not be able to identify the multiple as such as it is generated by the same type 2 seismoelectric signal. Strictly speaking it is not noise, but an undesirable outcome of the electric fields from Type 2 signals decaying so quickly with depth to the interface, that a relatively strong reflection from deeper interfaces may propagate upwards to a shallow interface and create a Type 2 signal that appears deeper due to the extra travel time. However, the Type 1 seismoelectric signal may be recorded as a multiple Rayleigh or other related seismic wave. If the coefficient of reflection is very large, it is possible to detect the wave-front making a third or even fourth trip back to the acoustic-impedance boundary. This produces a set of approximately equidistant reflections, each weaker than the one above and with alternating polarity, beneath the primary event.

Like guided waves (described previously), multiples can be generated strongly enough to be recognized as events only if strong impedance contrasts exist as well. It occurs because the amplitude of the multiple is proportional to the reflection coefficient, which is very small for most interfaces. Guided waves, however, include supercritical multiple energy. Multiple waves may distinguish into two classes, namely long path and short path. A long path multiple is one whose travel-path is long compared with primary reflections from the same deep interfaces, and hence long-path multiples appear on a seismoelectric record as separate events. A short-path multiple, on the other hand, arrives so soon after the associated primary reflection that it interferes with and adds a tail to the primary reflection. Its effect is to change the wave shape rather than producing a separate event.

Head-waves or near-surface refractions are the cause of another of the Type 1 seismoelectric noise sources. This type of wave is a seismic wave that is refracted at the critical angle θ_c . At the θ_c the head-wave principally carries no energy. The transmitted energy, which is the product of the intensity and the beam width, is zero as the beam width becomes zero at θ_c . However, at angles slightly smaller than θ_c , the narrow beams do carry a finite energy. As the velocity layer usually increases slightly with depth, the refracted energy will be bent back within the lower medium toward the surface, and its travel-path is almost the same as that along the interface.

Thus, the result is nearly the same as if energy had been refracted along the interface. Head-waves can contain a significant proportion of the seismic energy and the proximity of the electric fields associated with the wave near to the dipoles allows these Type 1 signals to be seen. In our data records the presence of electric signals associated with the compressional head-wave is often visible as first arrivals on the near-offset traces (see Figure 3.3).

3.3.2 Electrical and Other Sources of Noise

The ambient or background noise is the pervasive noise associated with an environment, which is a composite of both near and far sources. This noise can be caused by wind motion, poorly planted electrodes, electrical noise from the recording equipment, power-line harmonics, VLF (very low frequency) and AM (amplitude modulation) radio transmissions, and natural atmospheric electricity (spheric noise). The noise produced from these sources is either random or not related to any action by ourselves. Another form of noise is acquisition related artifacts, which are generated in form of leakage currents, radiation or crosstalk from geophones or other sensors. In addition, EM fields associated with the impact or detonation of the seismic source are another type of artifact noise. These noise sources are associated with the gathering of data. Such acquisition related artifacts can often be eliminated, or controlled, by the careful design of instruments and field method.

Harmonic noise generated by power lines and generating systems is nearly always present to a greater or lesser degree, and is often the major obscuring element in a seismoelectric record (Butler, 1996). Not every record collected for my thesis is dominated by power line noise, but it is usually present to some degree. It is seen even in remote areas that are far from cultural activity, industrial areas, and power lines. Although the amplitude of noise may vary, depending on the ground resistivity around each dipole, it tends to be relatively uniform in character over the survey area. The ambient electric field (mostly from power-line noise) in the earth measured in field tests around Curtin University, Perth, is 2 mV/m peak-to-peak, at the Pingrup test site it is around 20 μ V/m (see Figure 5.10), and it is about 800

$\mu\text{V/m}$ at Nannup test area (Figure 5.20). Much of the harmonic noise in our data is not only at 50 Hz, but also at harmonic frequencies at 100 Hz, and 150 Hz, and sometimes 250 Hz or 2500 Hz. Application of the sinusoidal subtraction technique described by Butler and Russell (1993) can be used to remove most of the power-line noise. This method proved capable of suppressing numerous frequencies without distorting or attenuating the signal of interest.

VLF and AM radio signals are another ambient noise source, which is transmitted all over the globe. High-powered VLF transmitters which are scattered around the world and use frequencies in the range of 15–30 kHz, are usually used for naval communication with aircraft, ships, and submarines. AM radio which has carrier frequencies of hundreds of kHz is also prevalent in remote areas despite being transmitted from a local radio station. The frequency ranges of both signals are actually well outside the range of the acquisition band of 1 Hz to 1000 Hz, thus, these signals should not introduce any noise. However, at the electrodes of a grounded dipole (especially at metal-electrolyte interface) some demodulation of radio frequency signals can occur, but it appears that such effects were not significant in the data in this thesis. The possibility of strong AM signals leaking into the audio band was monitored by listening to the analog output of the dipole with headphones and no distinctive tones or music were heard.

The source signal for natural-field EM with the frequency range 0.0001 to 10,000 Hz is located outside the earth (Dobrin and Savit, 1988). At frequency range above 1 Hz, the energy comes from electrical phenomena in the atmosphere, such as thunderstorms. This locally generated energy propagates over great distances in the space between the conductive surface of the earth and the ionospheric cavity. The resulting **E** field is induced by the interaction between the magnetic field of the EM wave and the geoelectrical structure of the earth. These signals were at times obvious in records as events appearing at late times, but could be mistaken for seismoelectric events at earlier times. If the dipole array is set in a split spread configuration the signals will appear with reversed polarization on opposite sides of the shotpoint and stacking all the channels will eliminate the noise. In addition, repeat shot records allow screening for this type of noise.

Electrical artifacts that are generated by coupling of geophone signals onto dipole channels (from cable leakage, radiation or cross-communication) are of concern because that could cause misinterpretation of seismoelectric signals. To avoid this noise, seismic and seismoelectric data acquisition were carried out independently. In addition, the seismic cable, the dipole array, preamplifier boxes, and the trigger cable were placed as far away from each other as possible (see Figure 3.4 below).

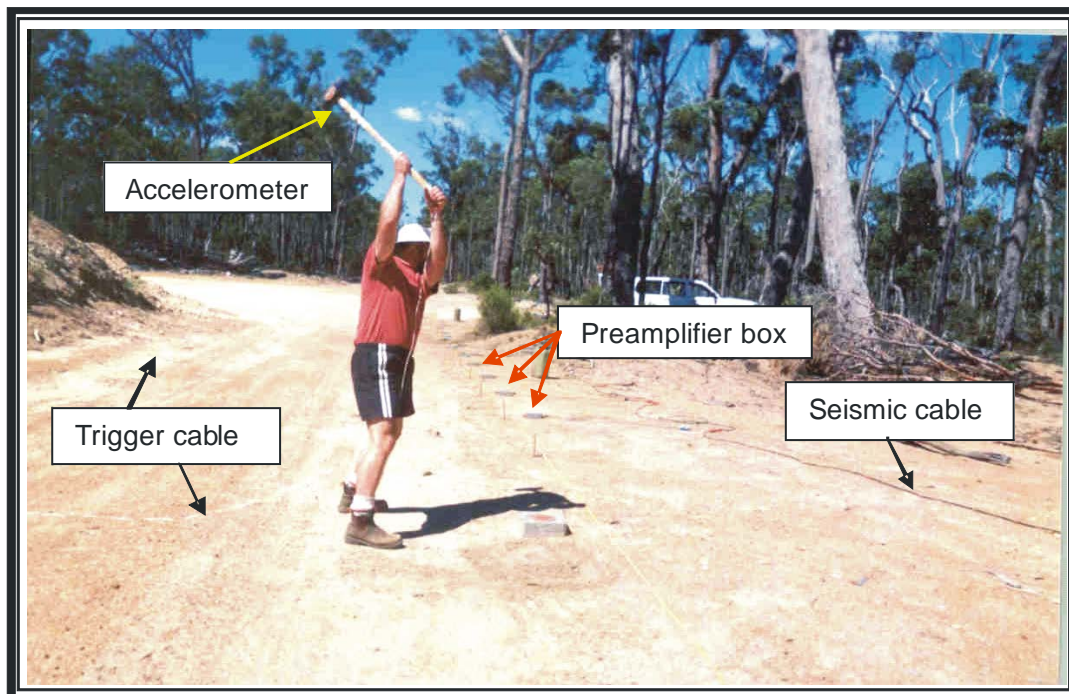


Figure 3.4. Field illustration how to avoid noise during data acquisition. Half of the dipole array is visible with trigger cable, preamplifier boxes, and seismic cable set away from each other to avoid cross-communication and other electrical artifacts during acquisition.

Electrical radiation from the accelerometer used to trigger data acquisition is evident in almost every recording, and proved to be impossible to eliminate with the seismic acquisition systems on hand. The interference takes place at time zero, or the impact time, and even though it arrives simultaneously along the dipole array it could be recognized and distinguished from electrokinetic signals because it is of short duration and dominated by frequencies higher than 1 kHz. However, further

processing with band-pass filters can cause this signal to obscure early seismoelectric signals. Other similar acquisition artifacts are those produced by the impact or detonation of seismic source. Sledgehammer blows and explosions will generate electromagnetic transients (Kepic, 1995). The interference of the hammer striking metal was avoided by removing the metal strike plate and using one with a large plastic plug inserted. As the impact was on the plastic the impact related artifact was not observed. It should also be noted that impact related noise would most likely be obscured by the trigger noise mentioned previously and difficult to observe.

3.4 Field Configuration

In the field measurements, up to 28 dipoles and preamplifiers were deployed to observe the seismoelectric fields. Twenty-four channels were always arranged on the ground to form a dipole array either in-line or as a split spread configuration. Two dipoles with preamplifiers were set as a remote reference set of sensors. These two dipoles were located far from the last dipole (usually more than 50 m in line away) to ensure that the seismoelectric signal does not make a significant influence on the reference measurement. In the tests described in this thesis the data from the remote dipoles were only used to monitor noise from distant sources such as power-line harmonic noise and spherics. There was little advantage in subtracting noise from the shot record using the remote dipoles as other processing or interpretation procedures were sufficient. Two preamplifiers were kept in reserve in case something happened (such as low battery or a broken connection plug) to one of the 24 preamplifiers collecting shot data.

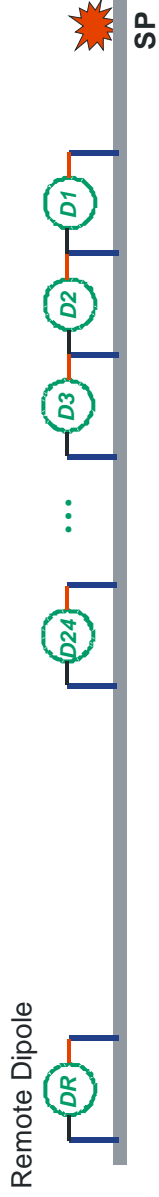
The 24 dipoles were arranged either in a contiguous or an overlapping configuration. The layout of a 24 channel scheme can be seen in Figure 3.5. The figure shows both contiguous configuration with a remote dipole and an (50%) overlapping split spread dipole configuration. The remote dipoles were only ever used with the contiguous dipole configuration. This is simply due to the fact that both the use of remote dipoles and contiguous configuration were later dropped in favor of a simpler overlapping configuration. The continuous dipole configuration was generally

arranged with a 1 or 2 m distance between stakes due to early studies being more focused on relatively shallow targets. This configuration has the advantages that the signals measured from one dipole are independent of another dipole. However, the contiguous dipole configuration did not record the signals well, as the signals are too weak, especially on the far-offset dipoles, compared to the ambient noise.

The split-spread configuration, as seen in layout (b) Figure 3.5, provides better records. This configuration, exploits the radial symmetry of the electrokinetic response, allowing easy recognition of many types of noise. The symmetry of signal polarity is an important characteristic to distinguish the seismoelectric response based on electrokinetic effect, from those caused by the modulation of earth resistivity (Broding et al., 1963). In order to capture the same polarity of seismoelectric response at both sides of the shotpoint, the negative electrode of each dipole were arranged closest to the shotpoint. The background noise, on the other hand, is recorded in reverse polarity on either both sides. So, this configuration does not really need remote dipoles to confirm the presence of external noise because of the polarity reversal of this type of noise. This technique has successfully been used by Thompson and Gist (1993), Butler et al. (2002), during their field experiments. The configuration is not ideal for investigating signal amplitude versus offset. However, if enough dipoles are used over a wide enough range of offsets then amplitude versus offset measurement is viable.

Overlapping the dipoles provide better shot records than a series of dipoles as the lengths of dipoles are greater in the former case. Distance between stakes could be set to 5 – 6 m versus 1 – 2 m in continuous/series dipoles configuration. Longer dipoles provide greater electric potential difference between stakes and thus, more signal. Even though the length of dipoles is greater, the distance between successive dipoles can be arranged either 25 cm, 50 cm, 2 m, or any other distance that divides the dipole length. The optimal configuration that I have found is a 50% overlapping dipole configuration because the signals are not too correlated with neighboring dipoles (due to overlap), and it still provides wide range of shot-to-dipole offsets to cover a wider range of depth of investigation. Butler et al. (2002) note that the strongest seismoelectric signal is at a shot-dipole offset of about half of the boundary depth.

a)- Contiguous Configuration



b)- Overlapping Configuration

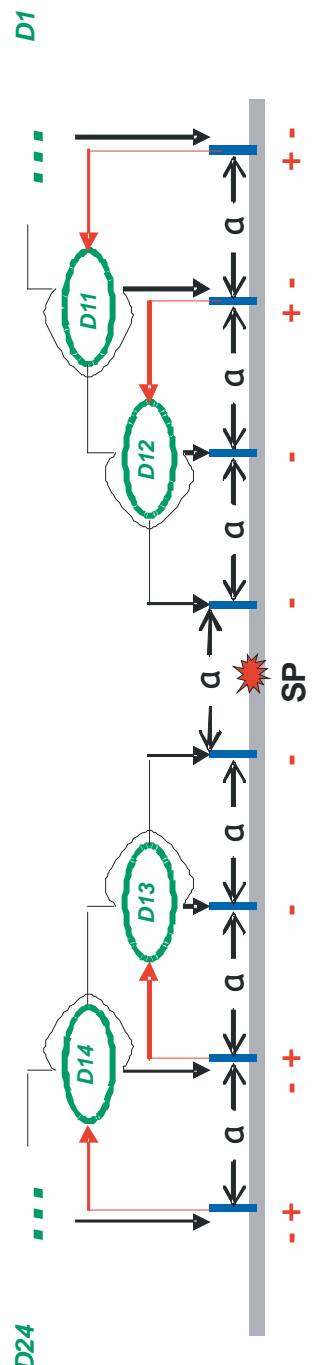


Figure 3.5. Geometry of 24 dipoles configurations . It was used in our seismoelectric measurements. Layout a) is contiguous dipole configuration with a remote dipole located more than 50 m away from dipole array, and b) is overlapping dipole with split spread configuration.

As the wavelength of type 1 seismoelectric signals are relatively short (due to wide-bandwidth and slow apparent velocities) aliased data are more easily avoided by using an overlapping configuration rather than series dipole configuration because for a given length of dipole successive dipoles may be placed closer to the shot-point. As one type of signal arrives simultaneously (or near enough) and the other propagates outward from the shot-point with seismic velocities an $f-k$ or $\tau-p$ filter should be able to isolate and eliminate the interfering signals. However, for such filters to work effectively with such narrow band-pass requirements the spatial sampling of the signal should be relatively dense. As the seismoelectric signal tends to contain relatively wide bandwidth pulses (significant energy from 100 to 500 Hz, Rosid and Kepic, 2003) spatial aliasing can become a problem too. Thus, an acquisition system with a fairly large channel capacity (>100) is needed to produce an array that will collect unaliased data and also has sufficient source-to-sensor offsets to effectively capture the distribution of electric fields from deeper sources.

The solution to the problem of needing a large number of channels to satisfy the two criteria is to use a 24 channel system with 5 or more shots to produce a single shot record with an equivalent of 120+ channels of data. This is done by moving the shot-point in the center of the electrode array by small increments to emulate the effect of shifting all of the electric potential stakes closer or further from the array centre. For example, if the ground stakes were set in a staggered array where successive dipoles are offset by 2m then combining data from shot-points at 0, +0.4, +0.8, -0.4, and -0.8m from the array centre would provide an equivalent to a single 120 channel record. The equivalent record would contain sensors spaced at 0.4m offset increments; thus, giving a high spatial density of data.

This method works on the assumption that the earth has a 1-D structure (i.e. properties vary only with depth). The seismoelectric signal of the first type is laterally invariant with respect to arrival time. However, arrival times of signals of the second type will change with shotpoint-to-dipole offset. A possible weakness with the proposed scheme is if there are significant lateral changes in seismic velocity within the centre of the array then there can be distortion in the created shot gather leading to artifacts. However, it would require extreme near surface changes to create significant artifacts in the virtual shot gather.

Unlike seismic exploration and other well developed geophysical methods, the seismoelectric prospecting method does not have any standardized procedures for data acquisition. However, some principles are outline below that may be used as a guide to choosing source – receiver geometry:

- a- Arrange as many seismoelectric channels as possible. Twenty four channels and a virtual 100+ channels have been used successfully. Arrange the dipoles over a wide enough range of shot offsets to enable the interpretation of the simultaneous electrokinetic events;
- b- Place geophones at the same position as dipole stakes to see the correlation between seismic and electric events, and to identify the possibility of artifacts associated with shaking of electrodes;
- c- Repeat shot records. The consistency of simultaneous arrivals is an important criteria in later interpretation;
- d- To suppress regional coherent noise such as powerline harmonics and spherics waves a remote reference dipole may be used, or apply a split spread configuration. The polarity of expected seismoelectric events will be the same either side of the shot-point, but the noise will have reversed polarity;
- e- Seismic refraction or reflection data acquisition or invasive investigation is needed to provide some information about geological structure and seismic velocities. It also aids later seismoelectric data analysis and interpretation.

CHAPTER 4

METHODOLOGY OF PROCESSING AND DATA ANALYSIS

4.1 Introduction

Electric signals recorded in the field tests have a waveform very similar to conventional seismic records. Also similar to seismic field records, the seismoelectric records contain different wavefields and modes of conversion associated with surface (Rayleigh) waves, compressional head waves, as well as converted electrical waves from boundaries (Figure 4.1). This means we should be able to separate the different wavefields, or types of response, with tools similar to those as used in seismic processing. However, as the signal-to-noise ratio in seismoelectric data is worse than in seismic records, and the properties of the desired signals are different from those in conventional seismic data a straightforward implementation of conventional filtering and stacking is not always applicable.

The first two signals (effects from Rayleigh and head or direct waves - the Type 1 electrokinetic response), as mentioned in the previous chapter, are easily observed across the whole array of receivers, whereas the last signal (the desired electrokinetic signal) is not easy to identify directly from raw data. As the Type 1 electrokinetic effect is contained within and travels with the seismic wave in homogeneous media, the signal has little information about geological boundaries. The Type 2 effect, on the other hand, is an electrical response from abrupt changes in physical properties (that quickly propagates or diffuses to the sensors); thus, it is deemed to be the most useful signal in determining hydrogeological properties. Unfortunately, the simultaneous Type 2 electrokinetic signal is usually hidden beneath the Type 1 signals and other noise. Therefore, to clearly identify Type 2 signals requires some sort of post-acquisition data processing. A principal means of separating this desirable signal (the Type 2 electrokinetic response) from the others is to exploit the fact that it has a simultaneous arrival time at all antennas. The noise that could not be avoided during acquisition is filtered/processed digitally with either

proMAX software (Landmark product running on a Unix system) or with ReflexW (by Sandmeir software running on a Microsoft Windows platform).

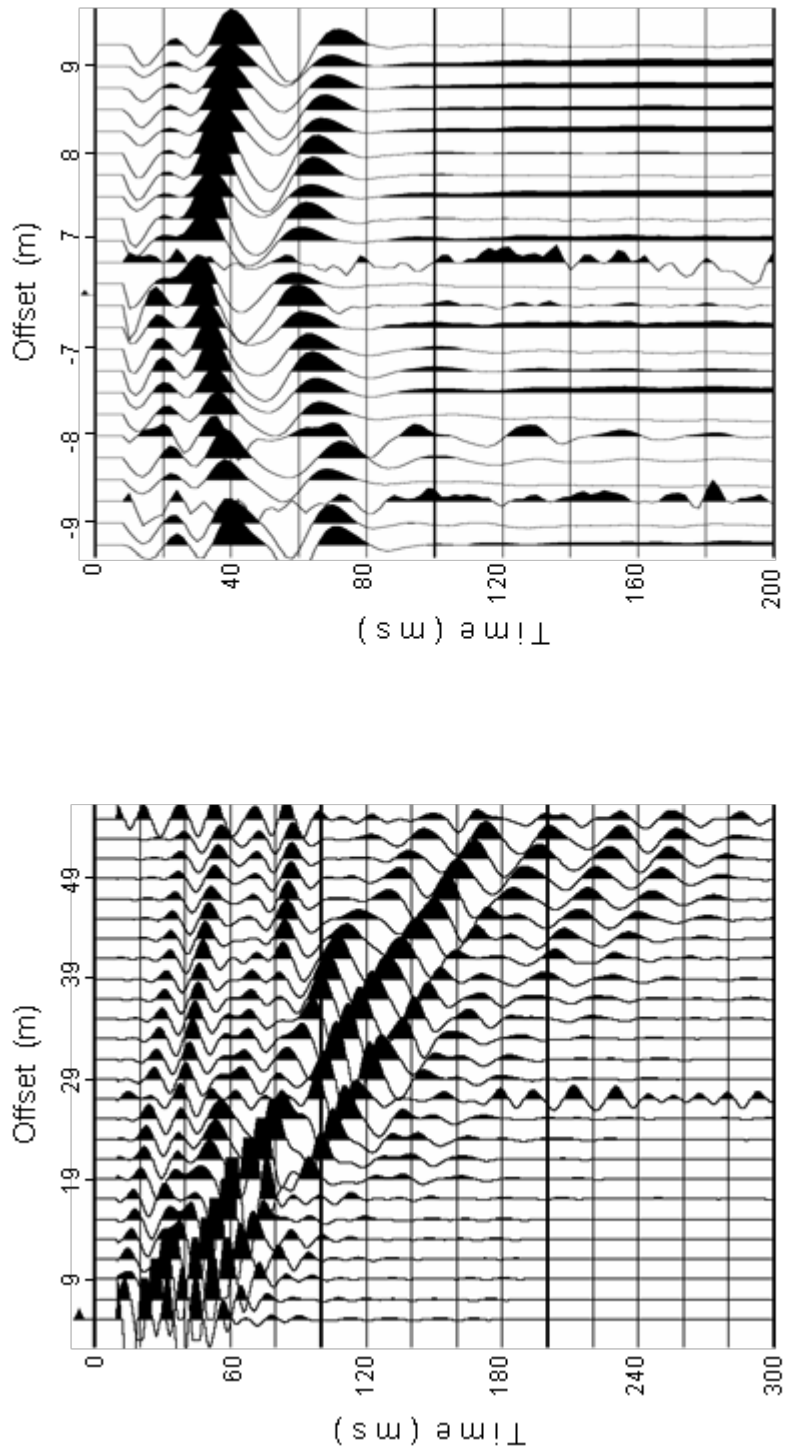


Figure 4.1. An example of raw seismoelectric data (right) in comparison with raw seismic data (left). The data were acquired from same location at Lake Bryde site using a hammer source. Both data examples have similar waveforms and are dominated by Rayleigh waves and direct waves.

This chapter discusses my approach to the problem of removing noise such as: narrow-band noise at frequencies of 50 Hz, and harmonics, band-pass filtering to suppress many types of seismic related noise, and f - k filters to reject relatively low apparent velocity signals that are generally associated with coherent linear noise (e.g. surface waves, direct waves, and all electrokinetic signals of Type 1). At the end of this chapter, I also describe the criteria used in the picking of seismoelectric events that may be used in the interpretation of seismoelectric data.

4.2 Removal of Powerline Harmonic Noise

A digital processing technique developed by Butler and Russell (1993, 2003) (the software implementation of the algorithm is called ‘HSUB’) has been occasionally applied in our data processing to suppress harmonic noise and is used as the main means of removing powerline noise. In most cases the powerline noise consists of a strong fundamental (50 Hz in Australia) and odd harmonics that are substantially less in amplitude than the fundamental. The data collected in this thesis, generally, did not have substantial harmonic components other than the fundamental.

The approach of Butler and Russell (1993) is to model the harmonic noise, $p(t)$, with a fundamental frequency f_0 as:

$$p(t) = \sum_{k=1}^{\infty} c_k \cos(2\pi k f_0 t + \phi_k) \quad 4.1$$

and this estimate is to be subtracted from the record $r(t)$ that also contains a signal $s(t)$, and non-harmonic noise $e(t)$

$$r(t) = s(t) + e(t) + p(t) \quad 4.2$$

It is assumed that amplitude, phase, and frequency of all powerline harmonics are constant over the length of the record. A least squares linear inversion approach is used to estimate $p(t)$. The algorithm was formulated to estimate the amplitude and

phase of each of the harmonics contributing to $p(t)$ and remove them from the record. To simplify the process the algorithm assumes that the fundamental frequency f_0 is known. It then allows us to use amplitude and phase estimation as important parameters in a least-square minimization problem and carry out an analysis of the sources of estimation error. We can eliminate the error associated with the presence of multiple powerline harmonics using calculated estimates over an interval that is an integer number of cycles of the fundamental frequency. The principal issues in the use of this algorithm are selection of a suitable time interval to estimate the noise amplitude and phase, setting the frequency search step for searching for a better fundamental frequency estimate, and what time interval for this search to take place.

Before running the harmonic subtraction (HSUB) software, filter parameters are set in a command file such as fundamental frequency and search limits, harmonic frequencies as range of integer number of cycles of the fundamental frequency, and a data interval for signal estimation that is ≥ 0 . For Australia (in our field data), the fundamental frequency was set to 50 Hz with a search step of 0.05 Hz. While smaller step value (e.g. 0.02 Hz) may produce better results, but these values sufficed for further analysis. The iteration process may not converge properly if the step value is set too small. In setting the data interval, the HSUB algorithm considers time zero to be at the start of the data traces regardless of whether we have recorded pretrigger data. To find the exact fundamental frequency, it is usually desirable to use a long interval, but a shorter interval is used (for instance in range of the pre-trigger time) for the amplitude and phase estimation window in order to exclude portions of the record where there are large signals or non-harmonic noise present. However, if we have applied any kind of filter to the data before the HSUB process then HSUB may not work well if the ends of the record (inside either the frequency estimation window or the amplitude or phase window) are included. Filter artifacts (end-effects) in these areas can negatively impact the HSUB estimates.

The sinusoid subtraction technique performs well when applied on real data. Butler and Russell (1993, 2003) claim to routinely subtract 10 to 25 harmonics of 60 Hz from their electrokinetic records, where the method has reduced the noise level by

up to 45 dB relative to the original trace. A principal advantage of this algorithm over many conventional filters is that by assuming that the harmonic noise is stationary in its properties it does not tend to introduce the damped ringing effects that other notch filters introduce with transients present in the record. However, if a large transient is present in the estimation window then the energy at the fundamental and harmonics will be spread across the whole record.

Figure 4.2 provides an example of powerline harmonic noise at 50 Hz (and 2500 Hz) in a plot of the amplitude spectrum from a seismoelectric data trace. The data were acquired from Nannup test area at borehole 17 (see Figure 4.2). The 50 Hz powerline noise is dominant as its amplitude (1.1 mV/m) and is much greater than (more than 10 times) the 2500 Hz signal (0.1 mV/m only). The harmonic noise was removed using both the ‘HSUB’ software with filter parameters as stated above and an 80 –1000 Hz band-pass filter.

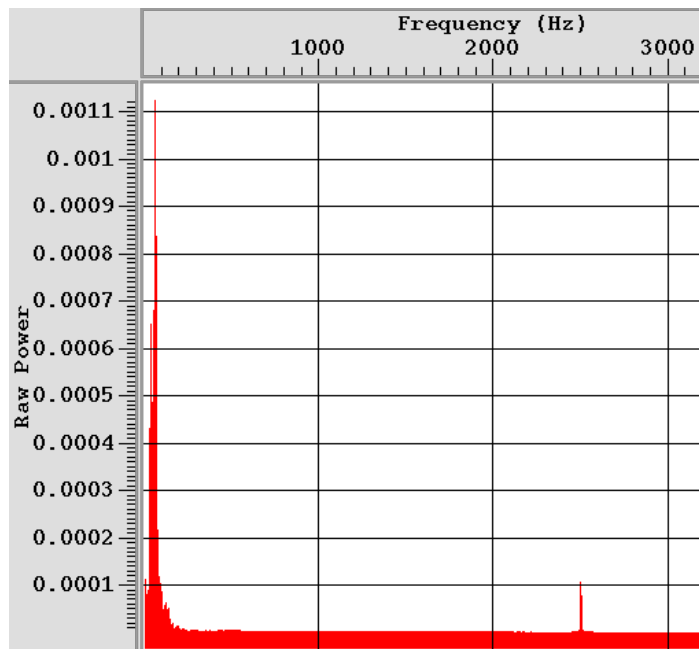


Figure 4.2. Powerline harmonic noise of 50 Hz and 2500 Hz. A spectrum analysis shows the noise that is clearly apparent in an electrical raw record (BW17 as shown in Figure 5.20). The magnitude of 50 Hz noise is much greater than the 2500 Hz signal and other seismoelectric signals.

4.3 Band-Pass Filter

A band-pass filter (BPF) is a filter that passes frequencies in a desired range and attenuates frequencies below and above. It can be created as a combination of a low-pass filter and a high-pass filter. Figure 4.3 illustrates an amplitude-vs-frequency graph, also called a spectral plot, of the characteristic curve of a hypothetical band-pass filter. The cutoff frequencies, f_1 and f_2 , are the frequencies at which the output signal power falls to half of its level at f_0 , the center frequency of the filter or resonant frequency. It is calculated as geometric mean,

$$f_0 = \sqrt{f_1 \cdot f_2} \quad 4.3$$

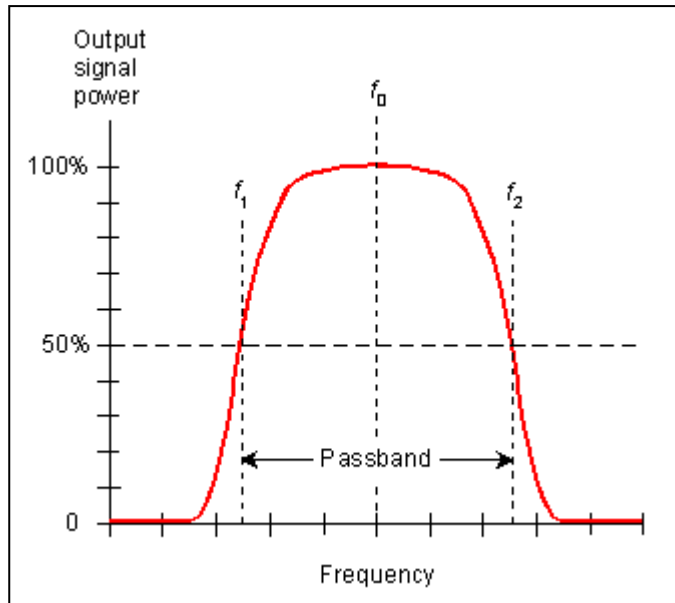


Figure 4.3. The characteristic curve of a hypothetical band-pass filter.

The quality factor Q is another parameter of the band-pass filter that is considered in data processing. It refers to two characteristics of the band-pass filter: the "purity" (bandwidth) of the signals and the persistence of the signals. The Q factor is defined

as the center frequency of a filter divided by the bandwidth, which can be formulated as,

$$\begin{aligned} Q &= \frac{f_0}{f_2 - f_1} \\ &= \frac{f_r}{\Delta f} \end{aligned} \quad 4.4$$

A "high Q" band-pass filter will respond to a short voltage pulse with a relatively long lasting vibration. A "low Q" band-pass filter, on the other hand, will vibrate for only a short time period. In the processing of data in this thesis a "low Q" BPF has been applied with as wide bandwidth Δf as possible in order to prevent the oscillatory ringing effect that (may) precede and follow the processed signal.

A digital band-pass filter was commonly used as the next stage in data processing after removing the powerline harmonic noise. It was applied in order to attenuate all ambient high frequency noise, in one side, such as VLF signals, high order power line harmonic noise, and natural electrical tellurics, and to attenuate Type 1 electrokinetic low frequency noises, on the other side. This process often improved the signal-to-noise ratio significantly (e.g. allowing signals with amplitudes as low as from 15 μ V to 1.1 mV to be interpreted (see Rosid and Kepic, 2004, 2005). A typical band-pass frequency filter used was 100 – 1000 Hz. Sometimes this filter worked very well, where simultaneous electrokinetic events are interpretable without the implementation of other filters such velocity filter.

The band-pass filter in the proMAX package software provided many alternatives to select the parameters which most suited our data. However, only two types of frequency pass-band filters were applied to all of the thesis data: Ormsby filter and Butterworth filter. Both filters are similar. The difference between them is largely in how to set the low-cut and high-cut ramp. The Ormsby filter arranges the ramp using a frequency interval directly, while the Butterworth filter ramp is set by the order of the filter (dB/octave roll-off). The Ormsby filter (often set to 40 – 50 – 1000 – 1100 Hz) was generally used to remove unwanted low frequency signals such as ground roll. While a Butterworth filter (e.g. in Nannup data processing 100

$-36 - 1000 - 96$) was applied to resolve the high-frequency seismoelectric signals generated from interfaces. Both filters are operated with either zero phase, or minimum phase (the preferred option as it is causal). Each filter is specified by a set of four integer numbers separated by dashes (as seen above). For the Ormsby filter the numbers represent sequentially the 0% and 100% points of the low-cut ramp (such as 40 – 50 Hz that creates a 10 Hz wide low-cut ramp), and the 100% and 0% points of the high-cut ramp (such as 1000 – 1100 Hz that creates a 100 Hz wide high-cut ramp). With the Butterworth filter, the numbers are divided into two pairs of frequency-slope values where the frequency values represent the -3dB points of the amplitude spectrum. For instance, specifying 100 – 36 – 1000 – 96 creates a 100 – 1000 pass-band filter with a 36 dB/octave low roll-off and a 96 dB/octave high roll-off. The 100 and 1000 Hz values correspond to the -3dB points of the filter. The low cut-ramp has been set with a moderate value to achieve as smooth (but steep) frequency changes as possible to avoid the artifacts from edge effects. The Ormsby ramps are formed by a cosine taper in the frequency domain, while the ramps for the Butterworth filter are formed by:

$$\frac{1}{\sqrt{1 + \left(\frac{f}{f_0}\right)^{2P}}} \quad 4.5$$

where f_0 is the center frequency of the pass-band and P is the order of the filter and is calculated for the lower and upper slopes to get the correct dB/octave roll-off.

Band-pass filtering of seismic data is commonly applied to enhance seismic reflection signals relative to some accompanying noise. A seismic trace often contains low-frequency noise, such as ground roll, and some high-frequency ambient noise. The usable seismic reflection energy is usually confined to a bandwidth of approximately 10 to 70 Hz, with a dominant frequency about 30 Hz (Yilmaz, 2001). This bandpass processing also allows us to do data filtering using one of three types of band-pass filter:

- i. Single band-pass filter, which applies a single filter to all traces at all times.
We only needed to specify and to input the four corner frequencies for the

Ormsby filter, or only one group of frequency1-slope1-frequency2-slope2 for the Butterworth filter.

- ii. Time variant filter. The parameters specify a time-varying filter (i.e. properties of filter change smoothly within a time window), which is then applied to all traces. The first filter starts from the beginning of the trace to the end of the first window, then (with decreasing linear taper) to the beginning of the second window. The second filter is applied with increasing linear taper from the end of the first window to the beginning of the second window, and so on. The last filter is then held constant through the last window to the end of the record. Filter windows may overlap.
- iii. Time and spatially variant filter. It applies a series of time varying filters which vary along the seismoelectric line.

The seismic processing software available provided two types of filter only: single filter, and time and space-variant filter. As the expected field geology was not so complicated to warrant the use of a spatial and time variant filter the single filter type was always implemented in seismoelectric data processing.

Most of the simple filtering implemented on the data collected in this thesis was with a Butterworth filter. This class of filter has a Maximally Flat response within the pass-band in the frequency domain because for a response of order n , the first $(2n - 1)$ derivatives of the gain with respect to frequency are zero at frequency $f = 0$. There is no ripple in the pass-band, and DC gain is maximally flat and monotonic overall. The Butterworth is the only filter that maintains its shape even for higher orders (just with a steeper decline in the stop-band). Other classes of filter (such as Bessel and Chebyshev) vary in the pass-band shape at higher orders. Furthermore, the phase response and the group delay of the Butterworth is a compromise between Bessel and Chebyshev filters (see Figure 4.4). The Chebyshev filter has a steeper roll-off and is characterized by a uniform ripple in the pass-band. With a Bessel filter there is no ripple in the pass-band, but it does not have as much rejection in the stop band as a Butterworth filter.

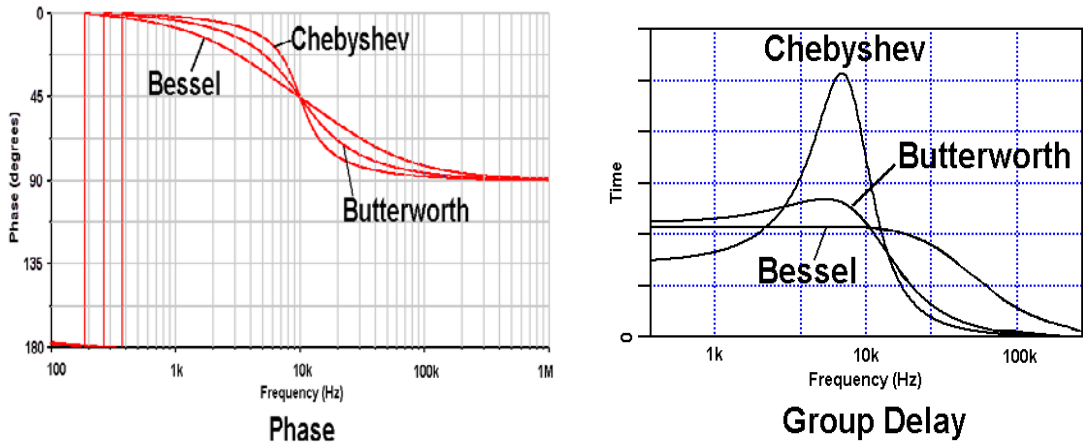


Figure 4.4. Butterworth response of phase and group delay. The response is shown in a compromise response between Bessel and Chebyshev response in the phase (left) and the group delay response (right) (after Carter, 2002).

The impulse response of the Butterworth filter used in data processing was studied in order to check whether the steep roll-off of the filter would introduce excessive ringing that may be confused with later arrivals. Note that the use of an AGC gain function in plotting can scale the ringing of high order filters so that multiple arrivals may appear from one impulsive event. Figure 4.5 shows the impulse response of Butterworth band-pass filters at different orders of n . The responses were created using Matlab system with a 150–800 Hz band-pass filter and the Nyquist frequency f_N of filter is 4000 Hz. The Butterworth impulse responses vary with order n . With a medium order ($n = 3 – 9$) the response generates significant artifacts. The higher the order n ($n = 7 – 9$), the longer the ringing. The impulse responses can ring with a periodicity that last for a relatively long duration.

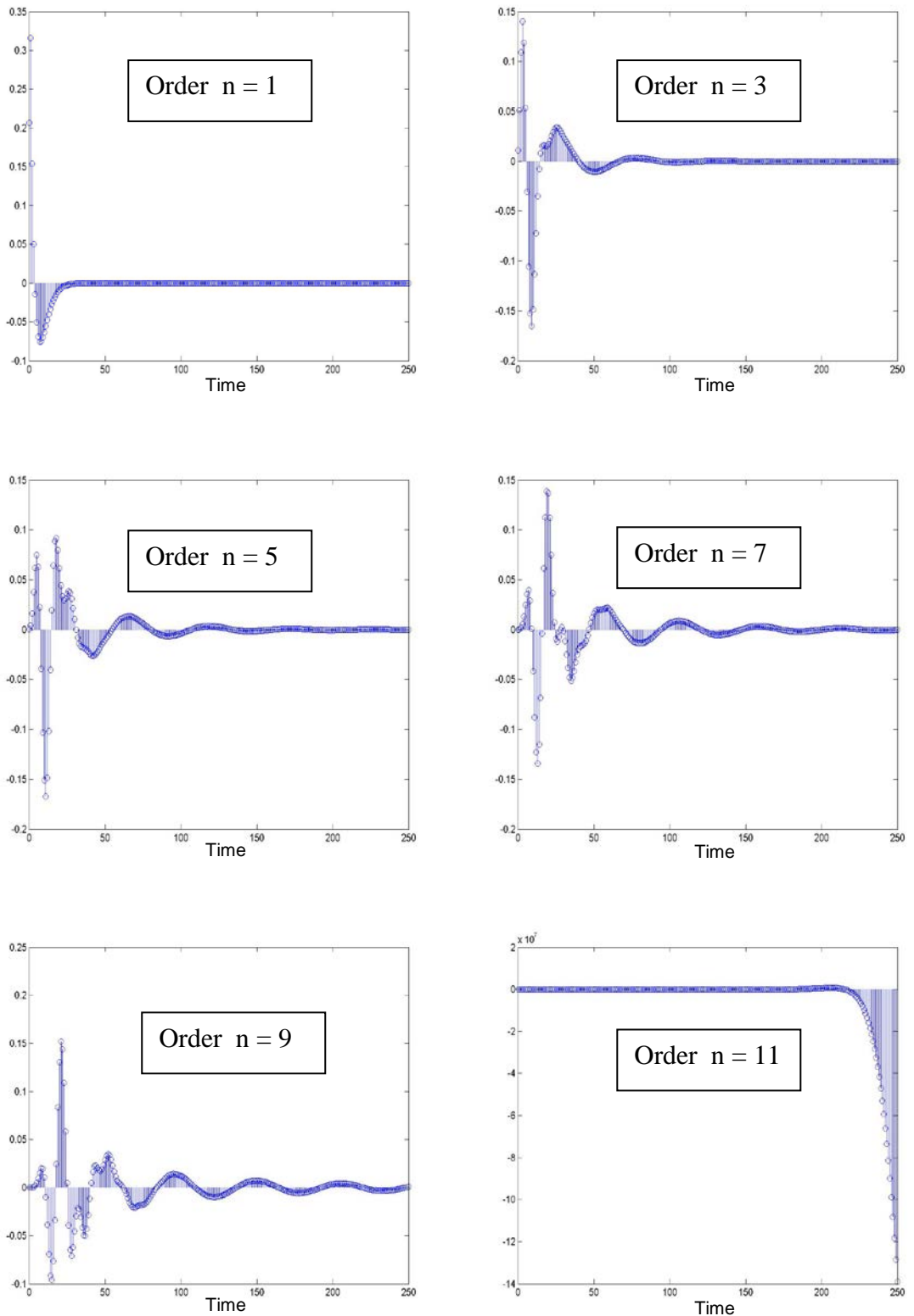


Figure 4.5. Impulse responses of Butterworth band-pass filter. The responses are shown at many different orders of n . It was produced from a 150 – 800 Hz pass-band filter on a time series with a Nyquist frequency f_N of 4000 Hz. The higher the order the longer the ringing.

A comparison between a filtered impulse response and real filtered data was made to test whether any of the electrical signals interpreted in the thesis data could be plausibly reproduced by passing the trigger impulse noise through a high order filter. The trigger impulse is the most likely signal component in the record that might cause ringing as it is impulsive and often very high in amplitude relative to the later seismoelectric signals. These comparison tests (Figure 4.6) show that the impulse response curves do not resemble the filtered signal (data processed using order $n = 5$). This is partly because there is not the same high frequency content in the field data.

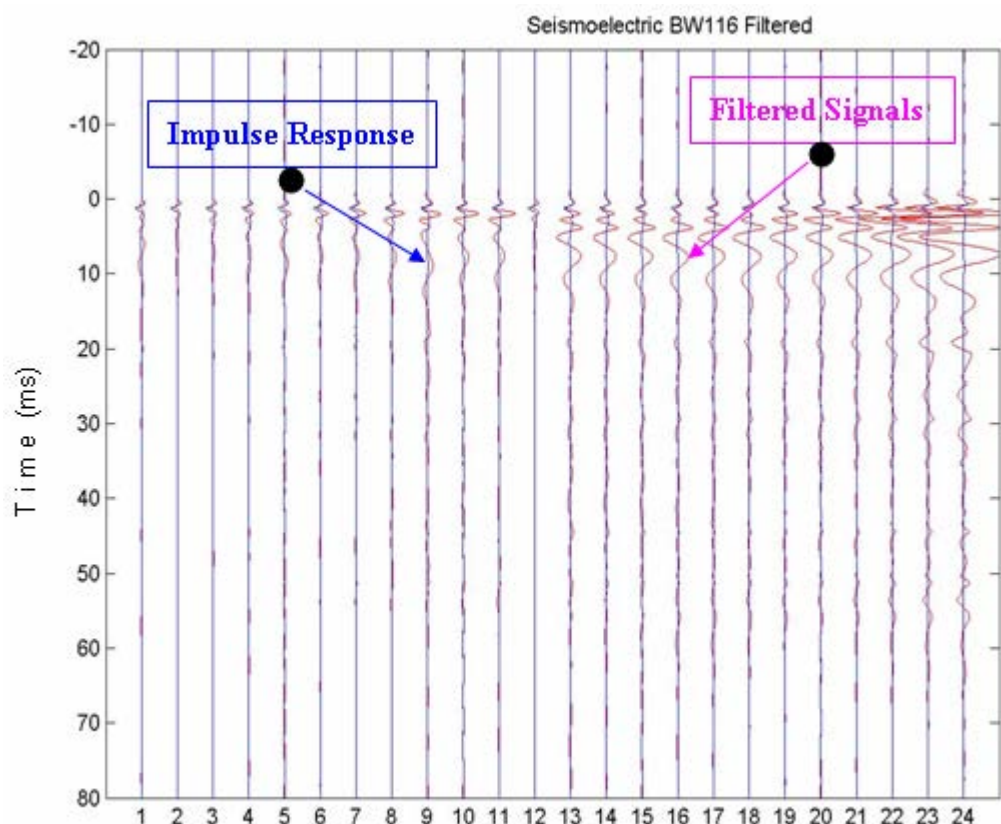


Figure 4.6. An example of Nannup seismoelectric data that were filtered using a Butterworth 80 – 1000 Hz band-pass filter. It shows the difference between filtered signals and a filtered impulse response in pink and blue colours. The impulse response amplitudes abruptly decline, whereas the filtered signals are more oscillatory in nature.

Amplitudes of the electrical data show that the energy rapidly decays at frequencies above 400 to 500 Hz. The impulse responses (in blue colours) match the filtered signals (in red colours) for perhaps the first simultaneous arrival, but are much better damped than the real signals. Thus, the filtered signals differ greatly in characteristics compared with the impulse responses, and I believe that all the filtered seismoelectric signals are genuine electrical fields generated from subsurface boundaries (or Type 1 signals). In addition, muting of the trigger signal (accidental in the case of some of the Pingrup data due to setting a post-trigger instead of pre-trigger) did not significantly change electrical signal characteristics.

4.4 F-K Filtering

The seismoelectric signals of most interest (Type 2 SE signals) are frequently obscured by ground roll, guided waves, direct waves, and refraction related events (Type 1 SE signals). It is a problem in common with the seismic reflection method, and similar means to remove these interfering signals, such as velocity or dip-moveout filters, may also be used to reduce the influence these signals have on the data. Type 1 electrokinetic signals propagate outward from the shotpoint within the seismic waves. However, Type 2 signals arrive at receiver array nearly simultaneously. Thus, a velocity based filter designed to principally pass those signals that have very high apparent velocities, and tuned to efficiently remove signals with characteristic velocities (of the Type 1 interference) can markedly improve the ability to detect Type 2 signals. Where the electrokinetic events are still hidden after band-pass filtering the next stage of processing is the use of an f - k filter to suppress the low velocity signals.

It is well known in seismic data processing that for enhancing the reflected wave signals, f - k filtering can be successfully used to eliminate noise such as coherent linear noise (e.g. ground roll, guided waves, and side-scattered energy), random noise, and multiple waves (Dobrin and Savit, 1988; Telford et al., 1996; Yilmaz, 2001; and Sheriff, 2002). Intermingled events recorded in the t - x domain become separated in the f - k domain by the dip angle, and then we may attenuate the unwanted signals. The unwanted signals are grouped separately from the reflection

energy where the reflection type of signals are situated around the frequency axis and coherent linear noise tends to be located close to the wave number axis. The undesired signals then are rejected, in the f - k domain, using one of three types of filters: fan filtering, arbitrary polygon filtering, or power exponent. The data is converted from t - x to f - k domain via a two-dimensional Fourier Transform. Due to the irregularity of the coherent linear noise distribution an arbitrary polygon filter mask was typically used to filter the data. Once the f - k filter is applied, the data is converted back to the t - x domain by the inverse Fourier Transform. The filtered data then are displayed and compared to the original data within the t - x domain.

Application of the f - k filter was limited to only some of my seismoelectric field data because it is a process that may create artifacts. However, it was sometimes necessary to use an f - k filter to remove low velocity signals that could not be sufficiently attenuated with simpler filtering. To avoid producing artifacts I used the following precautions:

- a- To avoid wraparound noise, which is produced when we implement the conventional Fourier transform, the data were extended beyond the ranges of the spatial and temporal axes by padding with zeroes.
- b- The fan filter width (or arbitrary polygon) should not be too narrow, because a narrow band-width can create a large array of nonzero elements in the t - x response of the dip filter. It will also stimulate ringing artifacts as impulse responses of f - k filter.
- c- The amplitude spectrum of the f - k filter must not have sharp boundaries. There should be a smooth transition from the reject zone to the pass zone, because sharp boundaries create end-effect artifacts or ringing in the time domain.
- d- Perform gain normalization to equalize amplitudes between traces. Otherwise traces with large amplitudes “bleed” into adjacent traces. With the Promax software AGC can be reversed after f - k filtering, thus, preserving to some degree relative trace amplitudes.

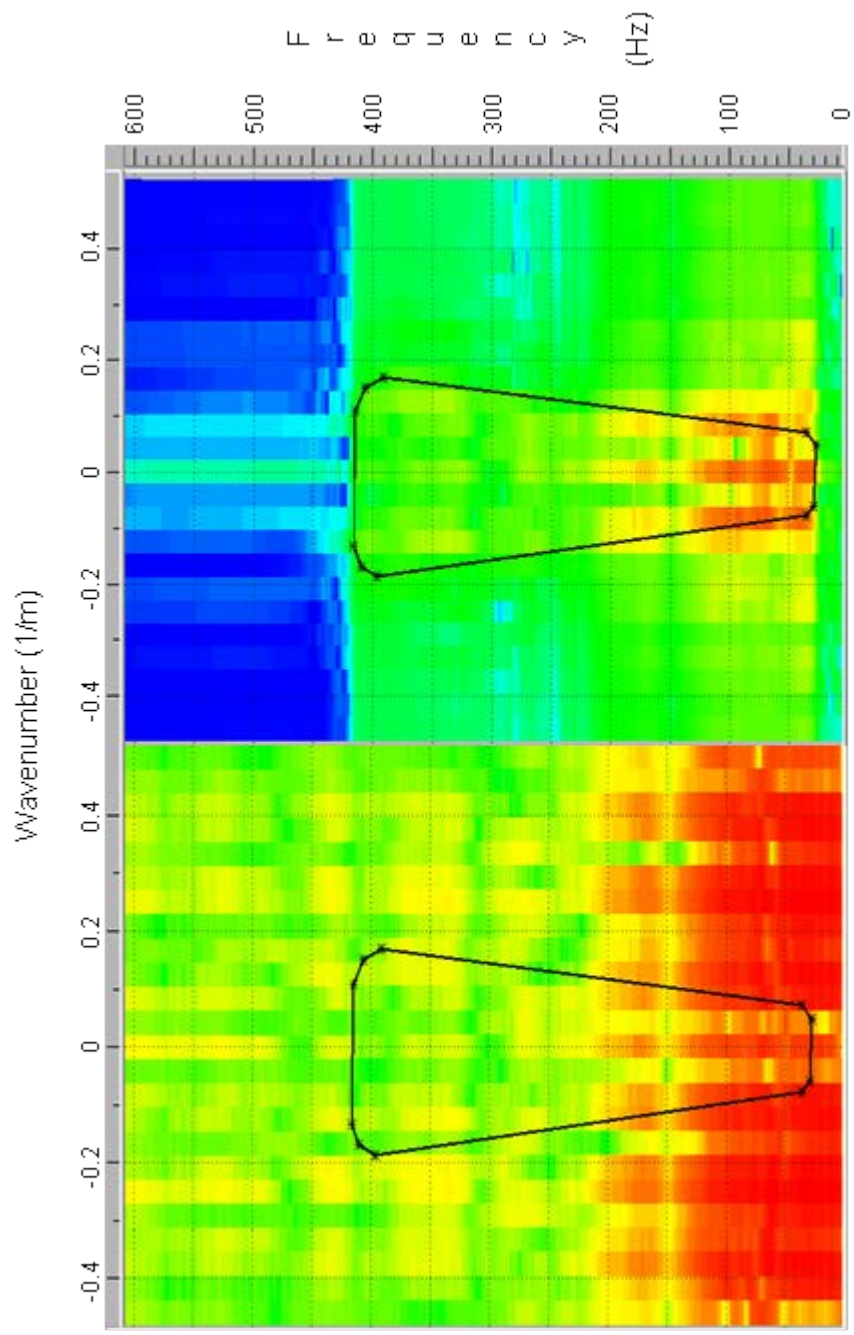


Figure 4.7. An $f\text{-}k$ analysis of seismoelectric shot record (left), and then filtered using arbitrary polygon filter (right side). The filter is designed as ‘pass’ filter, which gives little attenuation of the data within the polygon, and strongly suppressing the data outside of the polygon.

The f - k filter function in ProMAX system takes a different approach compared to many conventional methods to control the spatial extent of the impulse response. ProMAX filters are designed by explicitly specifying the limits of the impulse response in the t - x domain and then converting this to a mask in the f - k coordinate space rather than directly applying a taper to the filter in f - k space. In order to compute an exact t - x filter for a given pass or reject zone of the f - k plane, the filters are designed using Green's theorem. This t - x filter is then spatially and temporally tapered and transformed to the f - k domain with a 2-D Fast Fourier Transform (FFT) to create the mask. Typical taper parameters used with my data condition are spatially and temporal extents which are limited to 50 traces and 500 ms with a 90% flat taper. For large spatial and temporal extents of the filter, the taper length becomes less important because the amplitude tends to fall off naturally as the distance from the increasing impulse. For short extents, conversely, the taper has a large effect on the separation between the “accept” and “reject” zones. Principally, in smaller extents, to increase the separation between the keep and kill zones we should use smaller percentage number for the “flat” portion; thus, more tapering is needed (0% and 100% flats mean full Hanning taper and no tapering of the filter, respectively). In polygon and fan filter masks, the pass mode presents little attenuation of the data within the specified zone, but strongly attenuates to the data outside of this region. A reject filter, on the other hand, strongly attenuates the data within the specified region, while leaving the data outside this region relatively unaffected.

In practice, an f - k filter works with f - k analysis to interactively arrange filter parameters to optimize the filter size and windowing parameters. Using f - k analysis before applying f - k filter is an easier task than trying to input the parameters as text file of f - k pairs to design an arbitrary polygon filter. This way we can ensure that the polygons do not overlap, and to correctly specify frequency and velocity limits of the fan filter. Even though the filters used in the fan or polygon modes can be designed in the t - x domain I found it more practical to develop the filter within f - k domain for a specific size and then use an elliptical Hanning taper for the window. Less attenuation and a smoother response from the resulting f - k filter occurs when the t - x filter is smaller.

Despite the above mentioned precautions it still proved challenging to produce good results using the f - k filter upon seismoelolectric data. There are at least three important constraints that explain this difficulty. The apparent velocities of expected electrokinetic events are much higher than all seismic events. Normally, the f - k filter is commonly designed to attenuate low velocity coherent noise and enhance the relatively high velocity reflection energy. Therefore, a problem will emerge when we attempt to attenuate all Type 1 electrokinetic signals as these types of signals can have apparent velocities up to 5000 m/s. The problem becomes that of applying a very narrow fan or arbitrary polygon filter around the frequency axis in the f - k domain, which tends to stimulate artifacts in the impulse response of the filter. The problem of a very narrow fan filter can be largely surmounted if the spatial sampling of the signal is relatively dense. Unfortunately, we have a limited number of seismoelectric field sensors (up to 24 dipoles) and cannot match the multiplicity of seismic sensors (geophones) often used to surmount this problem. In addition, there is a limitation on the number of acquisition channels available for a groundwater surveying system. Another constraint in using an f - k filter to process the electrokinetic data is that the pulses tend to contain relatively wide bandwidth data (200 to 800 Hz), which causes a well known spatial aliasing problem with f - k filters. If an array of sensors covers a reasonable area to optimize signal strengths at different depths then spatial aliasing of the Type 1 is likely to result and will limit the effectiveness of the filter. An acquisition system with a fairly large channel capacity is required to completely solve the last two problems. In conclusion, use of a regular f - k filter for enhancing the seismoelectric events is difficult and these aspects should be considered: spatial aliasing, avoiding very narrow fan filters or arbitrary polygons, equalizing trace amplitudes, and making the edges of the fan/polygon as smooth as possible.

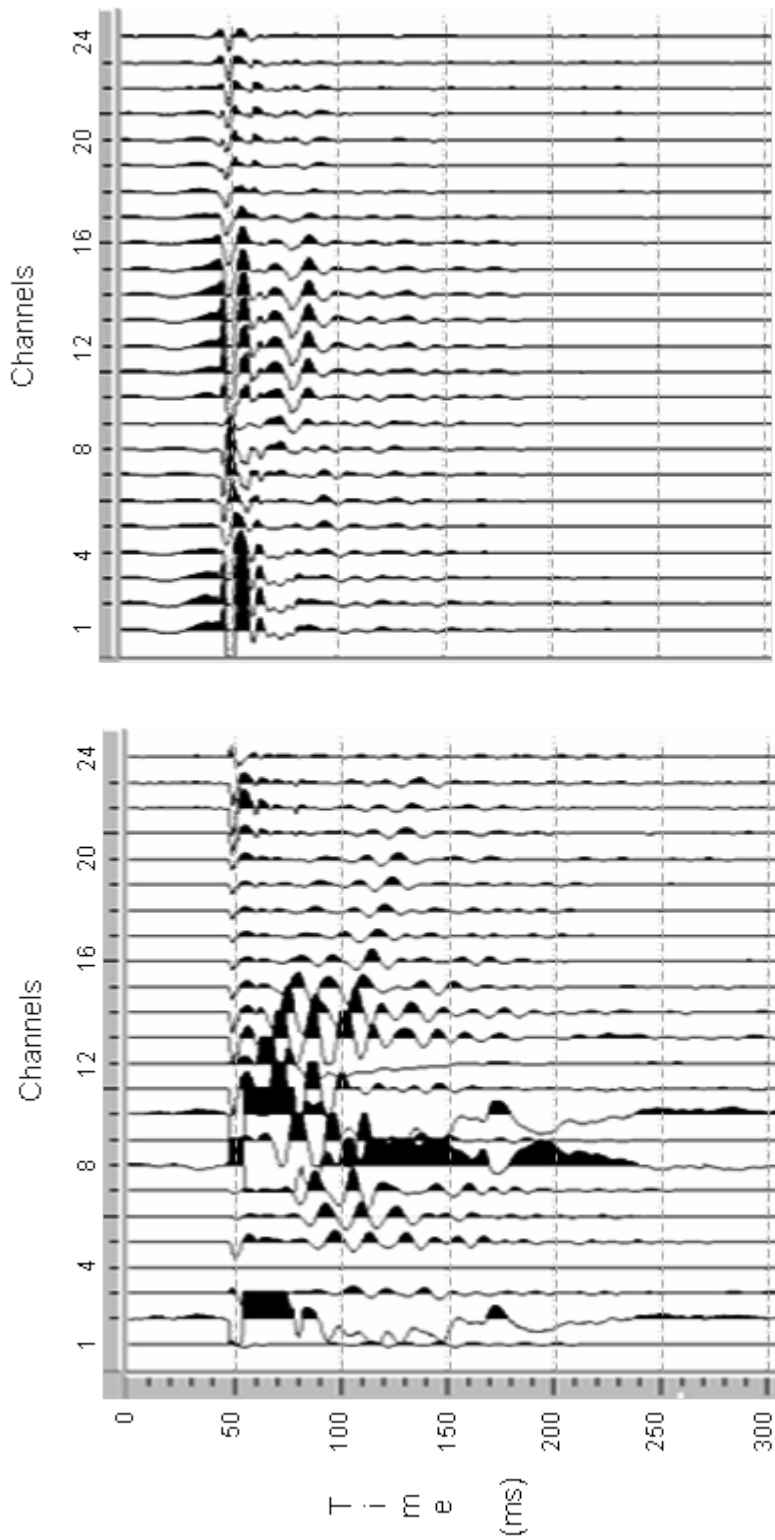


Figure 4.8. An example of $f-k$ filtered electrokinetic data recorded at Nannup area. The moment of hammer impact is at 50 ms. The seismograph was set to a sample rate of 0.125 ms and acquisition filter to 4 – 2000 Hz producing the data in the left panel. The $f-k$ filtered section is displayed on the right hand panel using the type of filter shown at Figure 4.7. Trace amplitudes have been normalized for display purposes.

4.5 Data Analysis for Interpretation

There are two stages of data analysis used to analyse our seismoelectric field data. The first stage is pre-interpretation analysis that is done during data processing to confirm that the signals result from seismoelectric responses originating from interfaces or boundaries. Secondly, an interpretation of the geological cause of the seismoelectric events is performed. The first stage uses the kinematic and dynamic criteria of Thompson and Gist (1993) and Butler et al. (1996) to distinguish seismoelectric events (Type 2) from both background noise and coseismic signals at dipoles. The criteria are:

- a- The seismoelectric signal wavelet is similar to the seismic wavelet;
- b- Seismoelectric signals reach all dipoles at virtually the same time;
- c- Signals are converted at a horizontal interface and originate from the first Fresnel zone centered directly beneath the shot point;
- d- Same signal polarity on the opposite sides of the shot point (if the “positive” electrode is closest to the shotpoint);
- e- The signal spatial pattern should have symmetry about the shot point;
- f- Signals are consistent from shot-to-shot;
- g- Signals are expected to have relatively low amplitudes and higher frequency content than coseismic signals; and
- h- The maximum amplitude of the electric field decreases as the depth of seismoelectric conversion increases, and the distance from the shotpoint of this maximum increases with depth.

Many seismoelectric events are clearly visible after applying a filter such as a bandpass or f - k filter (for examples see Figures 4.8, 5.11, and 5.22). Note that the events are relatively high-frequency signals, exhibit the same polarity on either side of the shotpoint, and the amplitudes decrease as a function of time. Arrival times of the signals are approximately the same. Upon very close examination many signals exhibit a very small apparent moveout, with measured apparent velocities of 56,000 m/s, 107,000 m/s, 215,000 m/s in the examples displayed in Figures 5.11 and 5.22. These are very fast (almost immeasurably fast given the 0.25 ms sample rate used in acquisition) velocities, but are in the range expected of EM waves in a moderately resistive medium. If the signals are consistent from repeat shots/measurements and

meet the above mentioned criteria we may then believe that the observed electric-field signals could be due to a conversion between seismic and EM waves at subsurface interfaces. Now the problem is to establish a causal link between the observed signals and hydrogeological lithology.

Borehole log data used in my work usually consisted of geophysical logs (natural gamma log and induction log), geology/lithological logs and sometimes a single probe resistivity log. These logs are compared with the seismoelectric field data to see if any wavelets (of either polarity) occur at the right depth/time of physical or lithological changes. To support the seismoelectric data interpretation, extensive use of geology and geophysics logs have been implemented. Alluvial clay, silt, sand, and gravel are the primary sediment types in the shallow subsurface of most survey areas in my study. Uranium and Thorium are concentrated in clay by the processes of adsorption and ion exchange and many clays are also rich in Potassium. Therefore, the following general assumptions were applied in making interpretations: (1) clay and silt have the highest levels of gamma radiation; (2) sand and gravel have the lowest levels. Gamma radiation of coal, limestone, and dolomite are less than clay and silt. Although these general assumptions may not be true elsewhere, they generally are confirmed for the Pingrup and Nannup areas by geologists' logs.

Seismoelectric events can be interpreted with the support of seismic refraction and borehole log data. Signal arrival times are converted into depth using seismic velocities generated from seismic refraction or reflection data. The signals are then compared to borehole logs to find what physical contrasts may have been detected. One issue in this method of interpretation is the interference of wavelets from closely spaced layers. Generally, the wavelet appears to have three lobes, but in the near surface (<10m) the signals have higher frequency content and at depth there is some evidence of dispersive effects changing the seismic wave shape. Therefore, when layers are relatively thin at depth it can be challenging to correctly identify the presence of another interface and choose the correct polarity of onset.

Unresolved layers proved to be a particular problem in interpreting the Nannup datasets where several layers appear to produce signals with a ringing nature. Thus

another approach was used in the interpretation of seismoelectric data. In this approach the depths of geological boundaries in the log data are converted into seismic signal transit times using a seismic velocity model generated from seismic refraction or reflection data. Then the predicted signal arrival times are compared to and matched with seismoelectric data to find if it is plausible to relate a seismoelectric event to a particular interface. Thus the lack of resolving power of the seismic input leads to uncertainty in many cases about the true cause of a seismoelectric signal as the earth often has many closely spaced layers with differing physical contrasts.

A more serious problem is that of multiples. Multiple events are divided into two types: the first type is associated with the Type 1 seismoelectric response associated with guided waves, which can be thought of as a type of interbed multiple (mentioned in the previous chapter - see Figure 3.4); the second type of multiple waves is a Type 2 seismoelectric effect from a primary seismic multiple. This type of problem arises because the electric fields from the seismoelectric conversion decrease very rapidly with depth (as an inverse cube approximately), but seismic waves attenuate mostly from spherical spreading (as an inverse of distance). Thus a strong reflection from a deeper interface may come back to the surface and generate a seismoelectric signal near the surface on its way up. This type of signal was seen in the Pingrup dataset, where apparently deep events were in fact traced to an origin near the surface. In the case of the Pingrup data the deep events were suspicious because the groundwater was hyper-saline and deep events should have been below our detection threshold.

To identify multiple events an AVO analysis (Amplitude Variation with Offset) can be applied to help distinguish between near surface signals and deeper signals. AVO analysis is widely used in petroleum exploration and employs the knowledge of reflected-wave phenomena to constrain the physical properties of two media at an interface. On seismic reflection data it is used in certain instances to obtain information about the subsurface that is not revealed by traveltimes-offset relationships. The method can be used to determine quantitatively, porosity, density, velocity, lithology and fluid content of rocks (via various sets of assumptions and prior knowledge). Here, in seismic-to-electrical conversion case the AVO variation

technique may be applied by employing an approach based on the Fresnel zone concept to estimate qualitatively the depths of interfaces (if the signal-to-noise ratios were very good then it could be used quantitatively). As the velocity of seismic and EM waves are very different, the size and shape of the seismoelectric Fresnel zones are almost independent of source-receiver offset. Therefore, the trace amplitudes versus offset at certain times in seismoelectric records may be plotted and analyzed for depth or similarity. In theory, multiple events can be characterized by a decrease in the maximum amplitude as a function of time due to the weakening of the seismic stimulus, but the spatial distribution of amplitude versus offset is relatively unchanged as it is from the same interface and characteristic of that interface depth. However, the wavefront will encompass a larger area due to flattening of the wavefront curvature and so it will not necessarily have exactly the same spatial distribution of electric fields as the first (primary) seismoelectric signal. In addition, amplitude variations may also be caused by geometric focusing, velocity focusing, interference, and processing errors. Nonetheless, clear seismoelectric AVO behavior characteristic of a conversion at a boundary has been confirmed by the analytic models and field measurements of Butler et al. (1996), full-waveform numerical simulation of Haartsen and Pride (1997), and the effect with multiple events experimentally seen by Garambois and Dietrich (2001). Thus, if there is sufficient signal-to-noise ratio AVO provides an important tool in analyzing seismoelectric signals.

Listed below are some characteristics of seismoelectric signal (Type 2) amplitude versus offset behavior that is sought in the second stage of data analysis:

- a- Distribution of the electric field amplitude as a function of source-receiver offset should form two asymmetric bell-shaped lobes about the shotpoint.
- b- The amplitude of any signal recorded on the surface should vary strongly (decrease) with depth of the interface or with time.
- c- The bell-shaped distribution of electric field broadens with the depth to the seismoelectric conversion interface.
- d- Maximum electric-field amplitudes move towards larger shot-sensor offsets as the depth of seismoelectric conversion increases.

Not all simultaneous seismoelectric (interpreted) events that appeared in my seismoelectric field records were generated from different interfaces. Some seismoelectric events occurring at different times had identically shaped AVO curves and further analysis of borehole logs and seismic velocity information led to the conclusion that the latter event was a multiple occurrence of the first event. If the events fulfill only the first two above mentioned criteria, then the event may be a multiple reflection. Thus, for a seismoelectric event to be uniquely associated with an interface it should entirely fulfill all four criteria above and not share the same AVO properties as an earlier event.

CHAPTER 5

FIELD EXPERIMENTS

5.1 Introduction

A series of field experiments were carried out over a period of three years to methodically investigate the capability of the seismoelectric method to provide useful information on groundwater problems. The resulting case studies (Butler et al., 2002; Rosid and Kepic, 2003; 2004; 2005 and Kepic and Rosid, 2004) show that the seismoelectric method has the potential to detect major changes in hydrogeological properties to depths of approximately 50 metres. However, at this stage the method does not always produce interpretable data. The results of these studies are summarized in this chapter and represent a major contribution to resolving the uncertainty of applying the seismoelectric method of prospecting.

The field experiments and surveys for this thesis were carried out at several sites as shown chronologically in Table 5.1. The three main areas that seismoelectric data were acquired were the: Nambi area, near Leonora (a paleochannel in a desert area near a lateritic nickel mine); Lake Bryde area, near the town of Pingrup (marginal wheatbelt farming area in southwest Western Australia); and the Blackwood catchment, near the town of Nannup (a region known for forestry with deep aquifers). These aquifers are important as sources of water for mineral processing (in the Eastern Goldfields of Western Australia, where the predominant fresh water supply is sourced from Perth via a 500 km pipeline), for drinking and farming use (livestock and crops), and for sustaining the local wetlands and flora/fauna. The paleovalleys hosting saline groundwater are sought in the Lake Bryde area for wetlands preservation via dewatering. This area is dominated by more than 10 saline paleovalleys. At Nannup, there are fresh water aquifers within the thicker sand/gravel layers in the Yarragadee and Leederville formations (40-1500 m and 1-30 m, respectively) that are being evaluated to supply 40-50 gigalitres of water to Perth (a city with more than 1 million in population located 300 km to the north of the aquifer) annually. Measuring aquifer quality and thickness is an important part

of evaluating the water reserves within a reservoir. This large aquifer is the target of an ambitious project by the West Australian government to provide domestic water for a large percentage of WA's population. Therefore, each experiment site not only represents a different environment, but also reflects the widely varying needs serviced by aquifer management.

Table 5.1. Field experiments carried out as part of this research. Each seismoelectric data acquisition was accompanied by seismic acquisition.

Date	Location	Data collected
14 – 16 July 2001	Murra-Murra Mine bore field, Nambi Station, Leonora, approximately 900 km northeast of Perth, WA	48 channel seismic and 16 dipole seismoelectric
16 – 17 May 2002	Line 01 Lake Bryde, Pingrup, approximately 400 km southeast of Perth, WA	24 channel seismic and 26 dipole seismoelectric (including 2 remote dipoles) measurements. Another group collected TEM data and down-hole logging data (induction and natural gamma).
13 – 14 July 2002	Line 03 and line 02 Lake Bryde, Pingrup, WA	24 channel seismic and 26 dipole seismoelectric (including 2 remote dipoles) measurements. Another group collected TEM data.
22 – 23 May 2003	BW 17 and 25 Blackwood Catchment, Nannup, approximately 300 km south of Perth, WA	24 channel seismic and 24 dipole seismoelectric. Another group acquired TEM data.
19 – 21 August 2003	BW 17 and 27 Blackwood Catchment, Nannup, WA	24 channel seismic and 24 dipole seismoelectric.
12 – 13 March 2004	BW 17, 25, and 16 Blackwood Catchment, Nannup, WA	24 channel seismic and 24 dipole seismoelectric acquisition. Forming virtual 100+ channel shot records.

5.2 Experiments at Nambi, Leonora

5.2.1 Field and Hydrogeological Description

The Nambi (Station) survey area is located in an arid and topographically flat area near Leonora, approximately 900 km northeast of Perth, Western Australia. The area was subject to exploration for fresh water in an extensive paleochannel system with the water to be used in nickel laterite mineral processing. The paleochannel is largely clay-filled with sand and gravel pockets present at the base of the channel where it has incised the underlying granitic bedrock. A geological section of the survey area based on a geological model and two boreholes located 50 m from the line is shown in Figure 5.1 and has five distinct layers: (i) surficial silty sand with

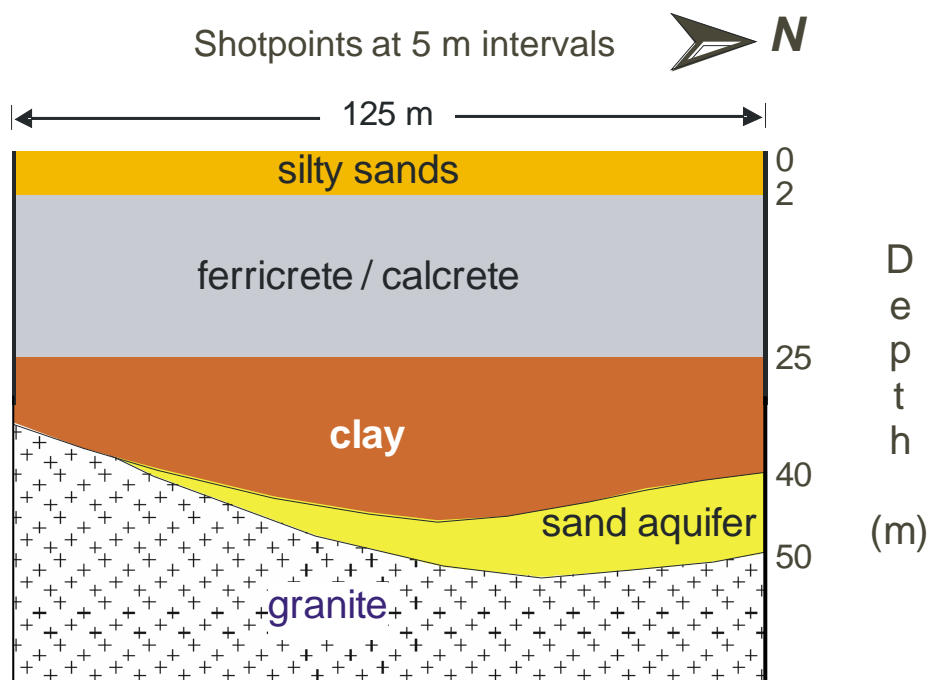


Figure 5.1. A geological section of the Nambi seismoelectric survey area based on geological model and data from two boreholes. It shows a sand body at the base of the paleochannel that thins towards the margins of the channel and overlying granitic bedrock (after Butler et al., 2002).

thickness of less than 2 m, (ii) a layer of fractured calcrete/ferricrete consisting of cemented sands and pisoliths approximately 23 m thick, (iii) wet clays up to 20 m in

places, (iv) coarse sands and gravel up to 10 m thick and, (v) saprolite and granitic bedrock. The water table depth was measured at approximately 20 m. The groundwater is relatively fresh and potable. A ground TEM survey in the area showed resistivities of the order of 5 ohm-m for the first 50 meters.

5.2.2 Results and Discussion

Figure 5.2 shows an example of raw seismic and seismoelectric shot records recorded at the Nambi field site. Both types of data were acquired simultaneously with two separate seismographs located away from each other to avoid cross communication. The seismic recording (seismograph OYO DAS1) site was located away from the seismic line at a fixed position. On the other side, the seismoelectric recording (Geometrics Geode) site was moved successively after a few shots to a

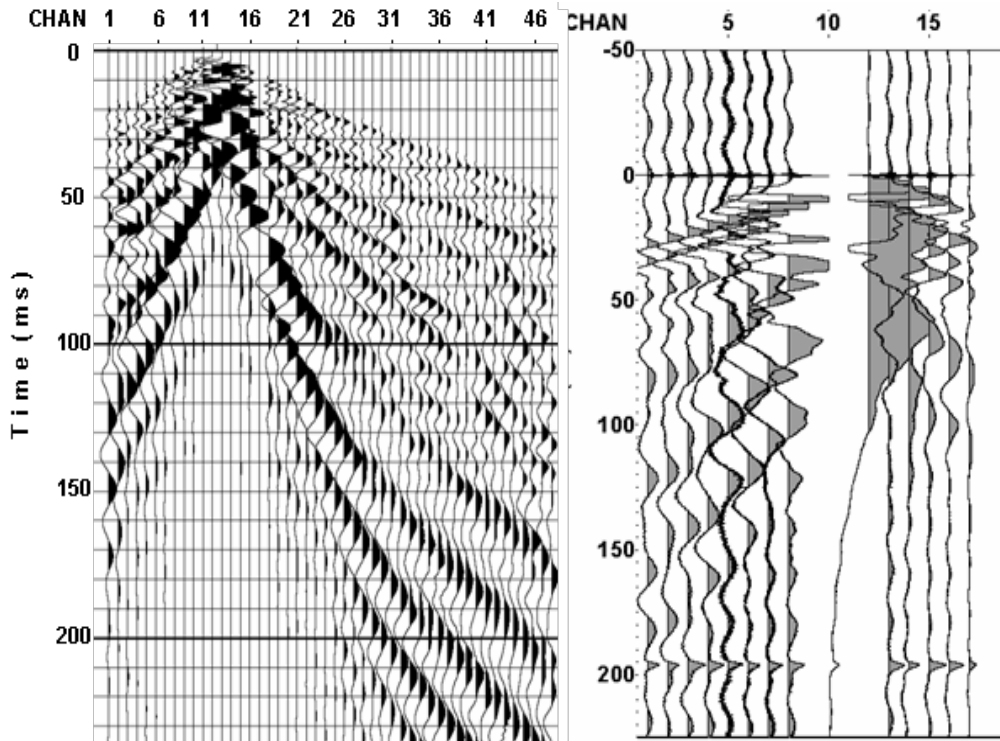


Figure 5.2. Raw 48 channel seismic (left) and 14 channel seismoelectric (right) shot records recorded at the Nambi site. Both sections are dominated by surface waves as well as powerline noise in the seismoelectric record (which appears before the impact time at 0 ms).

new position. A small 100 gram booster explosive placed into a shallow hole was used for seismic excitation, with the seismic and electric signals detected using 48 geophones and 14 – 16 dipole antennas, respectively.

The seismic and seismoelectric acquisition were done simultaneously to achieve good subsurface information as the hydrogeological target is very shallow. The seismic acquisition parameters were designed to provide reasonable seismic reflection signals (but were not optimized for reflection). As the primary sand/gravel target was at a depth of 40 – 50 m, the 48 geophones were arranged at 2.5 m intervals in an asymmetric split spread geometry. The fourteen grounded dipoles were arranged at 5 m series intervals in a nearly-symmetric split spread configuration. Seismic excitations via explosives were positioned along the seismic line at 5 m intervals. The raw data is dominated by waves trains from both ground-roll and guided waves. In addition, low frequency powerline noise (from nearby borehole pumps) is clearly present in the seismoelectric record. In short, the raw seismoelectric data did not display any obvious Type 2 seismoelectric signals, but had many co-seismic signals. The higher frequency character of the seismic record might be explained by the fact that it was acquired using 28 Hz geophones and a 50 Hz low cut filter whereas for the seismoelectric acquisition, the low cut filter was set to 2 Hz.

Even though the seismic record in Figure 5.2 shows some evidence of two weak reflections in the first 50 ms, it is difficult to find many clear reflections in the seismic field records. There is little in the way of refractions in the data due to the near surface presence of the ferricrete layer (and a velocity inversion at the ferricrete-clay interface). Thus, producing a seismic velocity model to be later used in determining the depth of electrokinetic interfaces cannot be easily obtained from either the reflection or refraction seismic data. The seismic data are dominated by guided waves that are trapped within the ferricrete layer, and traveling in the horizontal direction with a particular velocity that produces “ringing” in the records. This becomes evident in the seismic section shown in Figure 5.3 (after removal of ground-roll) as coherent waves which linearly repeat. Moreover, velocity picking in

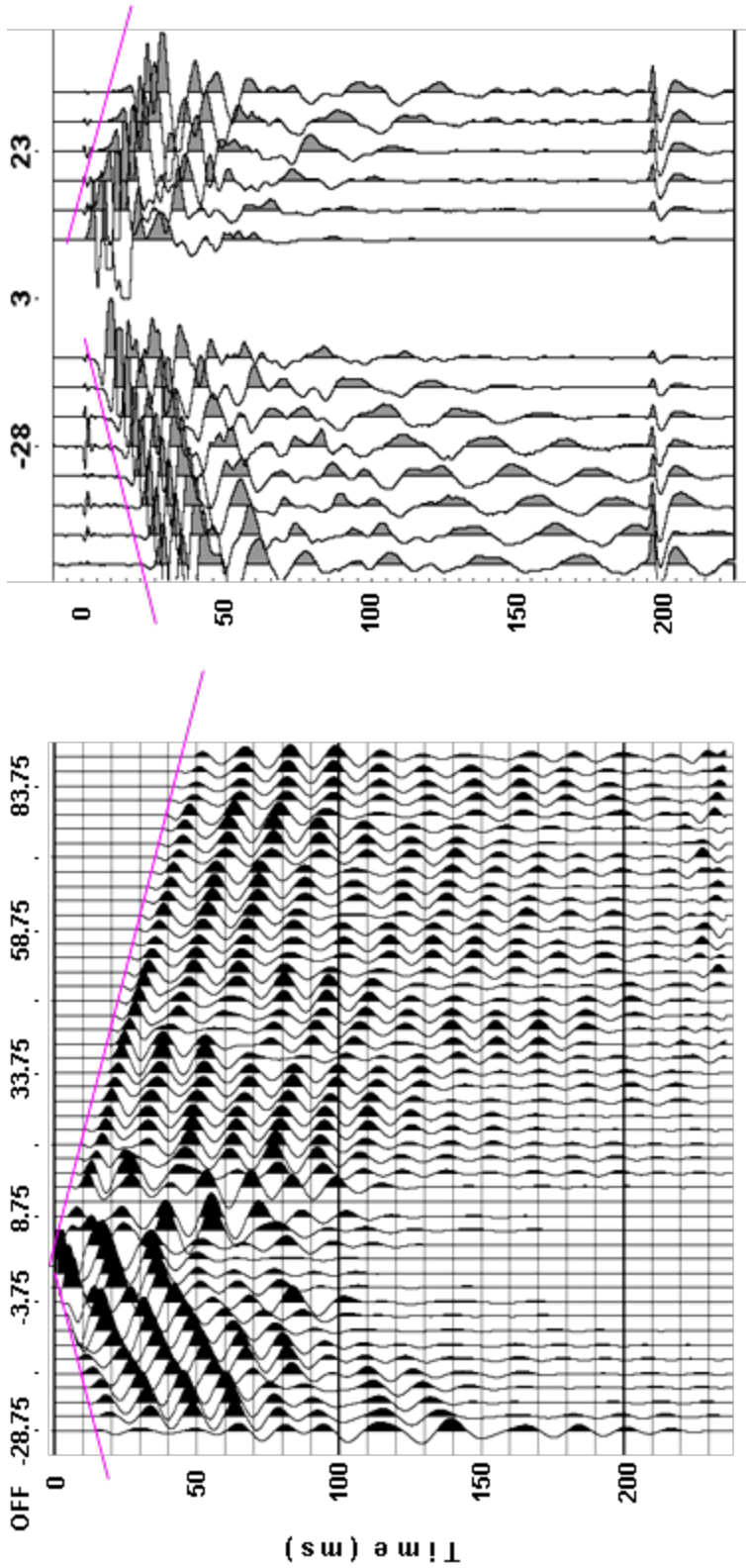


Figure 5.3. Processed Nambi seismic (left) and seismoelectric (right) data. Data are plotted trace-equalized. Powerline noise has been subtracted from the seismoelectric record and ground-roll removed from the seismic record. Both records have been filtered using a 50 – 500 Hz Butterworth minimum phase band-pass filter. The uniform polarity of the impulse at 200 ms, observed simultaneously across all dipoles in the seismoelectric record, indicates noise from a distant source.

velocity analysis for NMO (Figure 5.4) shows that the seismic velocity does not increase with depth as would be expected from a reasonable seismic velocity model for this environment. Indeed, most results from apparent reflections tend to pick a similar NMO velocity and some show a decreasing velocity with depth. Additionally, the linear slope in first arrival picks for the refraction velocities produced only one useful value of velocity (of the ferricrete layer, about 1800 m/s, see Figure 5.5). The velocity yielded from NMO velocity analysis in the reflection processing is a “constant” velocity layer of approximately 500 m/s which could be attributed to the surficial silty sand layer.

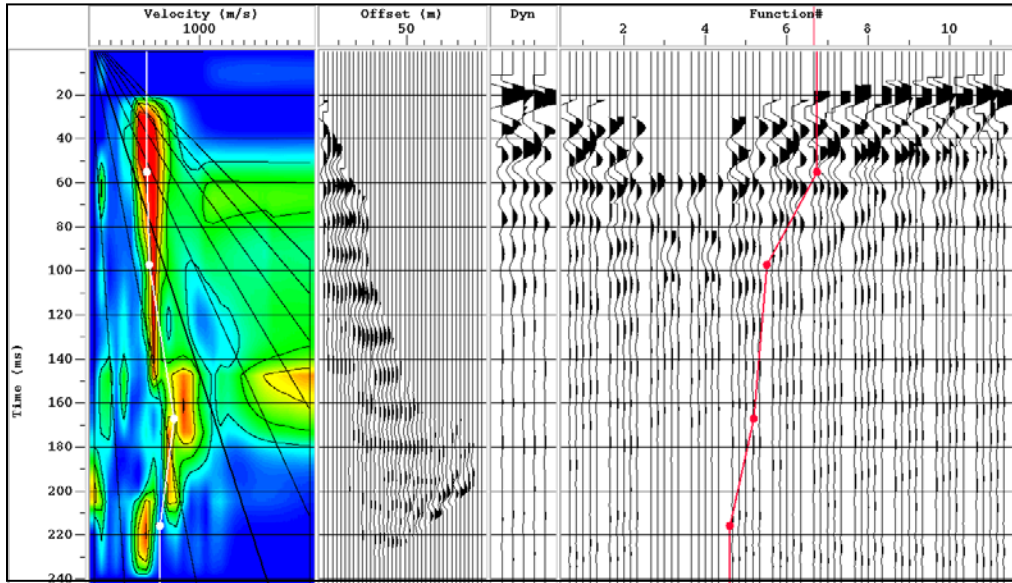


Figure 5.4. An example of velocity picking to find a velocity model using velocity analysis. The velocity model tends to pick a constant value of approximately 500 m/s with depth (increasing time). Flat NMO traces in the CMP gather column normally indicate good velocity picking.

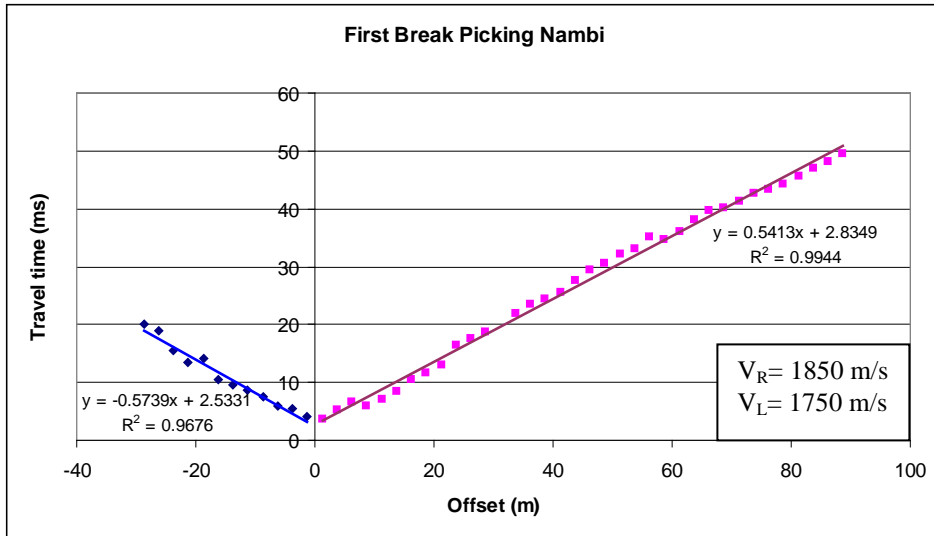


Figure 5.5. Time to offset curve plotted the first break picking of seismic Nambi data. The seismic refraction data shows that the seismic waves propagate only within a certain layer as the velocity is constant at about 1800 m/s.

In common with the seismic data, the seismoelectric records are also dominated by similar guided waves. This is most evident at early times (see Figure 5.3) and appears as three to four parallel bands of (Type 1) seismoelectric events recorded by the dipole array with the same apparent velocity. At later times, on the other hand, the seismoelectric record is dominated by lower frequency surface wave trains (i.e. ground-roll waves) similar to those seen in the seismic record. The amplitudes of these events range from a few tens of microVolts/m at the farthest offsets to several hundred microVolts/m at the near offsets. Note also that the seismoelectric signals accompany the first seismic arrivals. Low frequency powerline noise is also noticeable in the pre-blast time of the raw seismoelectric traces. The amplitude of this 50 Hz noise is approximately 15 μ V/m. This noise is largely removed from the seismoelectric traces (Figure 5.3) after applying a sinusoid subtraction algorithm (Butler and Russell, 1993).

Two events that appear essentially simultaneously across all dipoles are evident in the seismoelectric section shown in Figure 5.3. The first event is seen at time zero and the second simultaneous arrival is recorded 200 ms after the shot. Both events however, do

not represent an electrokinetic conversion from an interface at depth. The first high frequency pulse is correlated with the blast pulse which is seen repeatedly at zero time on various shot records, and is likely due to some blast related effect (Kepic, 1995). Although the amplitude and amplitude variation with offset were not consistent, the event is believed to be related to the trigger time. The inconsistency in amplitude may be due to the blast itself or possibly cross-communication between the trigger cable and the dipole antenna. The second strong pulse is rejected because the signal polarity does not flip from one side of the shot to the other as is expected for dipole sources within the array. As the polarities of all dipoles were arranged with electrode orientation in the same way, locating a shot point in the middle of the array should produce a seismoelectric event record with a reverse polarity pattern across the shot. It is most likely a noise spike from a remote source. The apparent increase in amplitude with offset in the processed record is due to the trace equalization scaling applied for display purposes.

Unfortunately, the Nambi data could not be usefully interpreted in terms of the available seismoelectric signals and the geological information. The prevalence of guided waves masks and interferes with any possible seismoelectric signals that might have been recorded simultaneously at the dipoles. The arrival times that may contain useful information are masked by events that appear to be associated with seismic waves sweeping by the dipole antennas. As the seismic (both refraction and reflection) data are also overwhelmed by guided waves, the apparent velocity of layers could not be obtained either. As a result, it would be difficult to identify the interfaces that produce seismoelectric signals.

5.3 Experiments at Lake Bryde, Pingrup

5.3.1 Field and Hydrogeological Description

Lake Bryde is situated in a semi-arid area with little or no topography near the town of Pingrup, approximately 400 km southeast of Perth, Western Australia (see Figure 5.6). The area provides poor yielding aquifers due to a shallow, predominantly crystalline basement, and relatively thin weathered profiles. In addition, the aquifers have low permeability due to their silty and clayey nature of the near-surface. However, sandy



Figure 5.6. Location of the Lake Bryde catchment, Pingrup, and boreholes used in interpretation (from Geological Survey of Western Australia, 1984).

intervals in the regolith with high intergranular porosity, and the alluvium layer are significant local aquifers and a source of groundwater for watering farm stock (Dodson, 1999). A geological and geophysical log (Figure 5.7) from a nearby borehole offset 2 m

from the seismoelectric acquisition line shows an example of the lithology in the test area. Single Pole Resistivity (SPR) log data were acquired from another borehole drilled to basement (less than 60 m depth) at LB05 in the Lake Bryde area. There are four main layers to be classified as: (i) a layer of alluvial sands and clays up to 18 m thick, (ii) a carbonaceous sand unit up to 14 m thick, (iii) a silty sand layer up to 23 m thick, and (iv) a saprolite/granite bedrock.

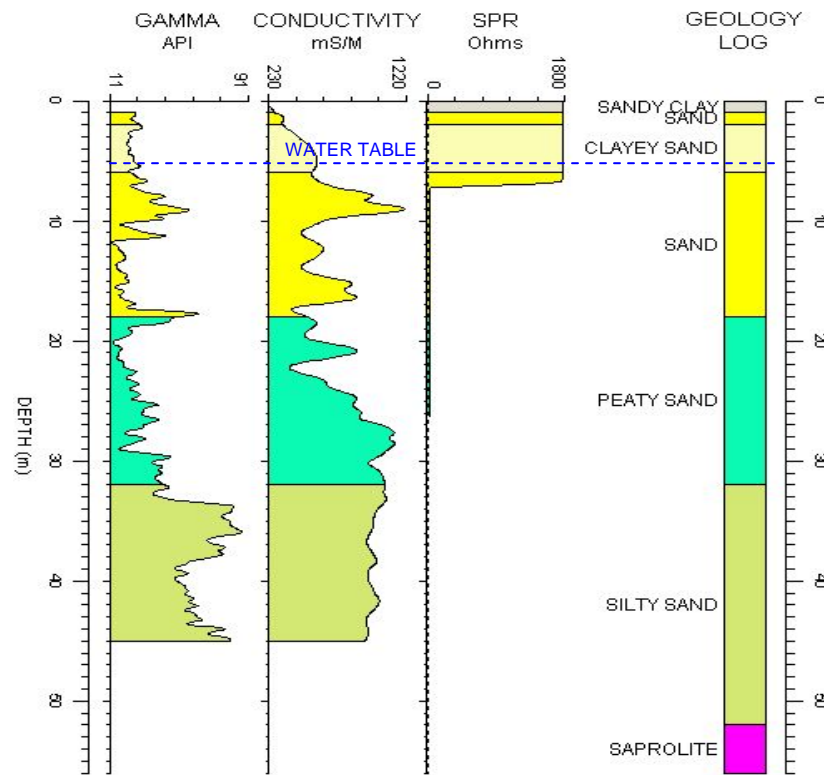


Figure 5.7. Borehole logs data of Lake Bryde site. It shows natural gamma ray, induction, SPR and geological logs (from left to right). The sequence is predominately sand/sand-clay mixtures. In detail, the log shows the alluvial sand unit as being interbedded with thin clay layers as well as peaty and silty sand. These sediments overlie a saprolite/weather granite. The log data also show that natural gamma ray and induction logs indicate more structure than the geological log.

The salinity of groundwater in this area varies widely. Chemical pH analyses show the groundwater to be acidic, with a pH range from 3 to 7. Sodium and chloride are the most dominant ions in groundwater in this area. Accumulation of salt carried by rainfall is the assumed source of these ions (Hingston and Gailitis, 1976). In general, the groundwater in the area is saline to hypersaline, ranging from less than 1,000 mg/L to more than 60,000 mg/L with an average of 37,000 mg/L. These salinity values can be compared to seawater at 35,000 mg/L. Low salinity groundwater may be located within the first few meters of the water table within sandy surficial sediments, but the salinity tends to increase dramatically with depth (Dodson, 1999). The increasing water salinity with depth is also shown in SPR log data (Figure 5.7), which indicates a general increase in conductivity with depth within the saturated zone (Rosid and Kepic, 2003). The maximum resistivity obtained from ground TEM measurements is of the order of 0.3 to 5 ohm-m for the first 50m, also indicative of a saline and/or clay-rich zone.

In this area, the conductivity of rock materials may be influenced by at least three factors: salt, clay, and peat content within rock matrices. This condition may assist to answer the geological anomaly which occurred within sand and peaty sand layer at 12 to 32 m depth. In the gamma log, increasing/decreasing Total Counts usually coincides with increasing/decreasing clay content (as mentioned in Chapter 4 for general assumption of natural gamma log – clay content relation) and electrical conductivity also rises with clay content. As shown in Figure 5.7 above, however, at this interval (especially at 12m to 22m depth) the curves differ with increasing conductivity related to decreasing gamma ray logs. The increased conductivity is probably due to increasing salinity (salt content) rather than increases in clay content as the groundwater becomes saltier with depth. However, the regolith products of mafic and ultramafic basement rock can also produce lower gamma counts than their felsic counterparts, but the basement is felsic in this area. Also, the peat content within sand layers creates more acid, lowering the pH levels and so the rock materials can become more conductive. Based on the log data, the conductivity changes with depth are likely to be associated with salt and peat content rather than with clay content. The peat soil is a light, fibrous material with very high water retention capabilities. Thus, the presence of peat within sand mixtures should slow water

movement through the layer and that means less permeability. So, in the peaty sand layer the chemical and fluid property contrasts are expected to influence fluid conductivity more than the clay content.

The watertable in the survey area varied slightly. At the time of the surveys the water table was at 8, 3, and 5-m depth, for boreholes at TEM survey lines LB01, LB02 and LB03, respectively (these parallel lines were approximately 1 km long (E-W), about 5-6 km apart, with line LB01 the northmost). Such significant differences might be attributable to subsurface barriers to water flow such as dolerite dykes, which are more resistant to weathering. For the purpose of this thesis only the data from LB03 is considered, where the watertable is situated within a clayey-sand interval. The watertable in the area fluctuates with the amount of rainfall and seasonal variation in evapo-transpiration rates from extensive salt lakes. The main aquifer is a relatively thick sand unit that overlies the saprolite/granite bedrock. This unit appears to be part of the paleovalley sediment.

5.3.2 Results and Discussion

Due to time constraints, the velocity models of this area were obtained from seismic data acquired from seismic refraction, and not a reflection configuration. Twenty-six geophones were planted with 2-m interval spacing. The field data were recorded with the two opposite end-on shot-point configuration. Three different shot point offsets (distance from the nearest geophone to shot point) of 3 m, 5 m, and 23 m were implemented to produce deeper and more reasonable refractors, or refraction waves. The data from 10, 20, or 30 sledgehammer blows were stacked for each record.

The seismic refraction data (as shown in Figure 5.8) were processed using the time-intercept method to provide P-wave velocities and layer dips as well as depths (Palmer, 1986; Burger, 1992). Four near-surface layers were identified. In terms of matching to the available geological log data, these layers may be referred to as: an unsaturated

alluvial sand to sandy clay; a semi-saturated alluvial clayey sand layer; a saturated sedimentary sand; and a saturated peaty sand layer. The apparent velocities of these layers (as shown in Figure 5.9) are 690, 1260, 1990 and 2400 m/s, respectively. With regard to the seismic shot records, which show similarity and symmetrical pattern, the layers appear flat (i.e. no apparent dip). These layers were identified from the calculation of refraction data as having thicknesses of 2, 4, and 9 m respectively. The velocity layer model is summarized and viewed in Table 5.2.

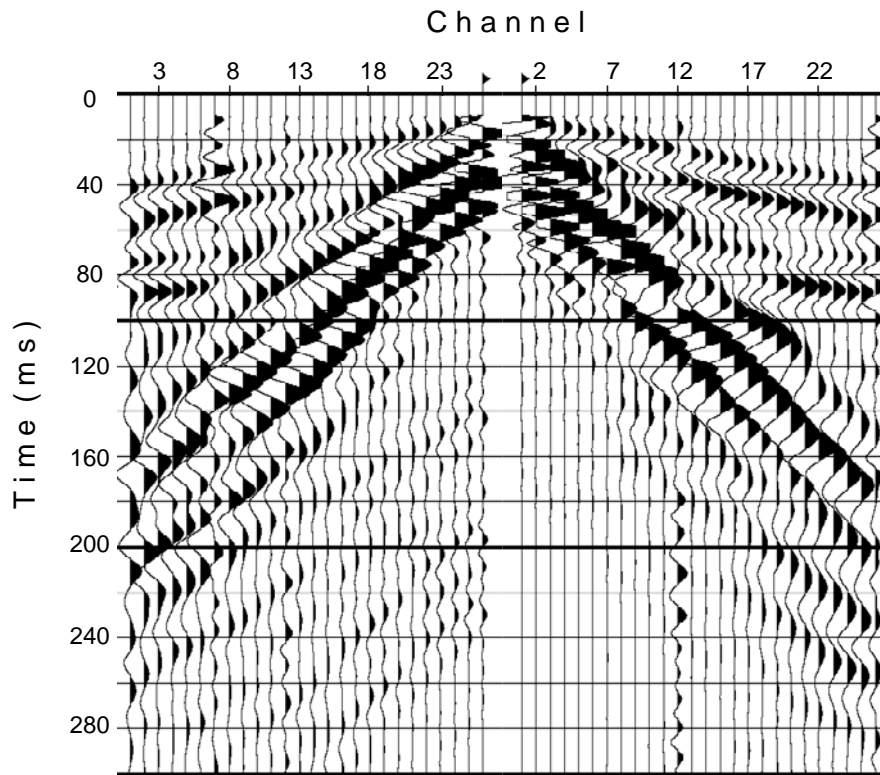


Figure 5.8. Two seismic shot records recorded at LB03 Lake Bryde field site using 26 geophones with 2 m interval spacing. Array configuration is end-on with the shot points located 5 m away from the end and the first geophone for left and right array, respectively. Both records are similar and symmetrical. The time of impact is set at 10 ms.



Figure 5.9. Time to offset curves used to determine a velocity model. Picked from 26 channels of Lake Bryde seismic refraction data. Four layers are identified, where the depth to the top of the 4th layer is 15 m.

Table 5.2. The velocity model obtained from LB03 seismic refraction data

V_{app} (m/s)	Thicknesses (m)	Depth of top layer (m)
$V_1 = 690$	$Z_1 = 2$	0
$V_2 = 1260$	$Z_2 = 4$	2
$V_3 = 1990$	$Z_3 = 9$	6
$V_4 = 2400$	$Z_4 = \sim$	15

Figure 5.10 shows examples of raw electric-field data and raw amplitude data collected at three different locations (LB01, LB02, and LB03) in the Lake Bryde area. The data were recorded using 24 dipoles with a dipole sensor spacing of 25 cm for both LB01 and LB03, and 50 cm for LB02 positions. At position LB02 the trigger setting on the DAS-1 was set to post-trigger instead of pre-trigger, thus, the first 50 ms of data is absent. This

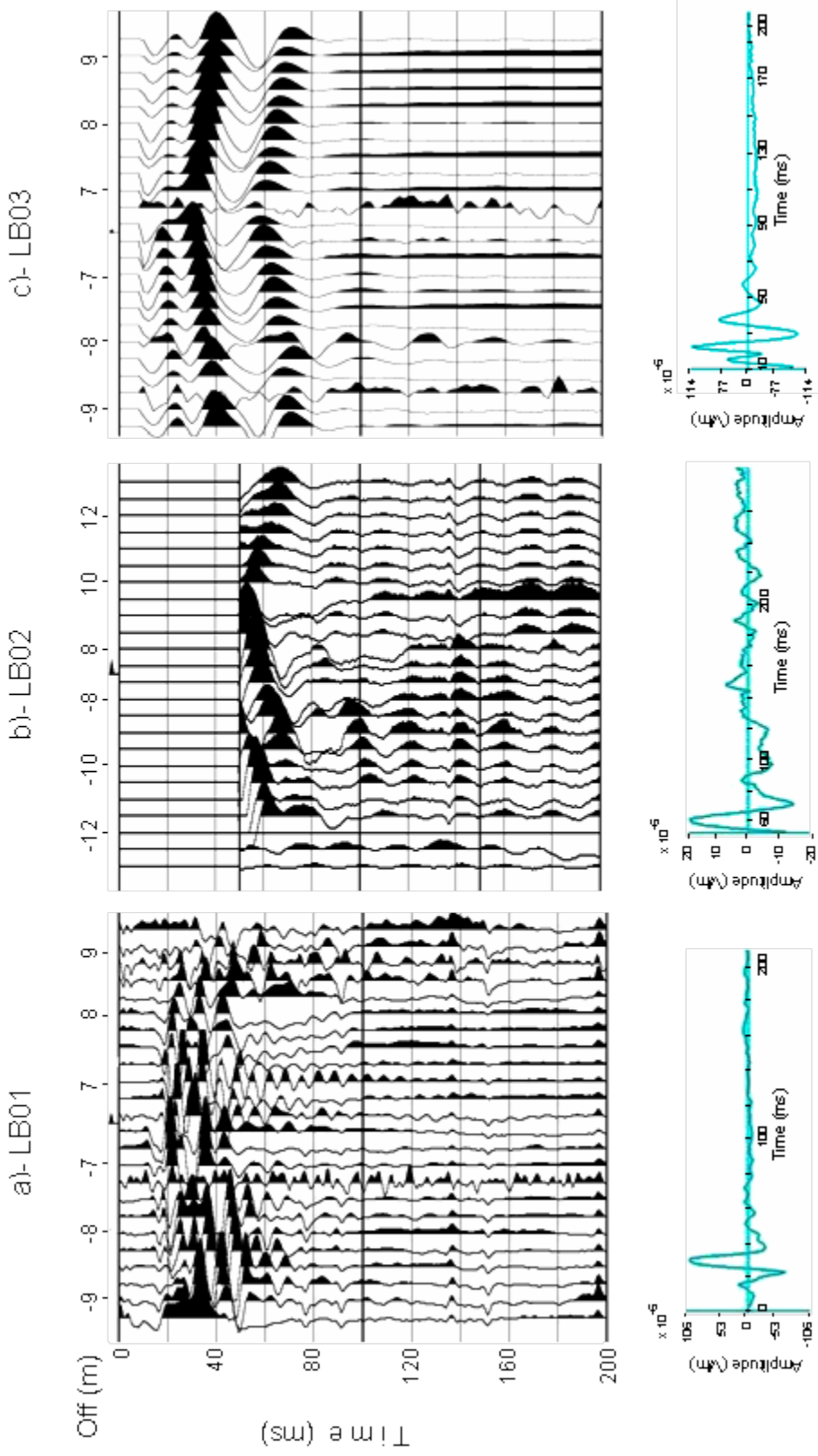


Figure 5.10. Raw seismoelectric data collected using 24 dipoles from three different locations at Lake Bryde area. The dipole sensor spacing is 25 cm for LB01 and LB03, and 50 cm for LB02 with a split spread and overlapping dipole configuration. The positive electrodes are in the inward direction of the array. The sections are dominated by electrical signals associated with ground-roll. Some simultaneous signals appearing at later time are not considered as electrokinetic signals. The amplitudes of signals are around 105, 20, and 110 microV/m at LB01, LB02, and LB03.

error was due to operator inexperience as the raw seismoelectric data is often very difficult to interpret and problems can go unheeded. Whereas the impact time in LB01 and LB03 position data was arranged to occur at 15 and 10 ms in the record, respectively. In general, the electric data are dominated by electrical signals associated with ground-roll. This signal masks other important electrical signals from the direct P-wave, refractions near the electrodes, and electrokinetic signals from interfaces (the desired Type 2 signals). Dipoles nearest to the shot point are the most affected, with low frequency “wow” associated with the vadose zone. This low frequency seismoelectric effect may be due to some near-shot viscous relaxation and is very reproducible (but not predicted in any theoretical analyses). In addition, the presence of electric signals associated with the compression head wave is also visible as the first arrival on the near-offset traces. In LB01 data, moreover, other high frequency and low amplitude telluric noise from a remote source interferes with the early signals, and appear as a simultaneous signal at (somewhat) times such as at 90, 138, 150, and 198 ms. These signals are not considered to be simultaneous electrokinetic signals generated by interfaces. Even though their polarity is the same as that expected from seismoelectric events, the signals are not consistently produced when the measurements are repeated with slightly altered shot-point position. Very noisy (telluric) conditions caused LB01 records to be less interpretable than the other site, and masked any simultaneous electrokinetic signals. In LB02 data high and low frequency powerline harmonic noise dominates late signals as seen by the polarity reversal on opposite sides of the shot-point. The 50 Hz powerline noise is very clear in the spectrum amplitude for LB02 data. The amplitude of this noise record is estimated to be 2 microV/m. The data in LB03 records does not exhibit obvious powerline harmonic noise effects, but long period noise is evident. These signals should originate from a remote source as the amplitude is relatively low. The maximum amplitude of recorded signals of LB03 is approximately 110 microV/m. None of the electrical records exhibited electrokinetic signals from interfaces beyond 80 ms after impact.

Some simultaneous events are visible in the raw shot records. However, these events are actually related to the trigger signal, or are non-repeatable (and have the wrong polarity symmetry with respect to the shotpoint) and are attributed to ambient noise external to the experiment. Simultaneous seismoelectric signals (the Type 2 electrokinetic signal) only become evident after implementing a (50 – 55 – 600 – 650 Hz Ormsby zero phase) band-pass filter and followed by a 200 – 600 Hz Butterworth zero phase band-pass filter to remove some unwanted signals. It has been demonstrated by Butler et al. (1996) that the Type 2 seismoelectric signals tend to have higher frequency content, so a selective band-pass filter can be quite effective in isolating these signals from Type 1 signals. Figure 5.11 shows filtered, repeat shot records from LB03 position; a series of high-frequency events have reached all dipoles at approximately the same time. The events are most evident and consistent at early times. These three records are obtained from the same location and same electrode configuration, but at slightly different shot point positions (less than a meter in offset from each other). The ability to reproduce these signals provides greater confidence that they arise from geological/geophysical interfaces. To ensure the validity of an event being simultaneous a careful check of the apparent velocity was made on an enlarged portion of the shot record. Figure 5.12 displays some of the filtered data shown in Figure 5.11 over the interval 5 – 45 ms, which clearly shows the very high apparent velocities of events. The amplitude of the filtered signals is approximately 10 microV/m.

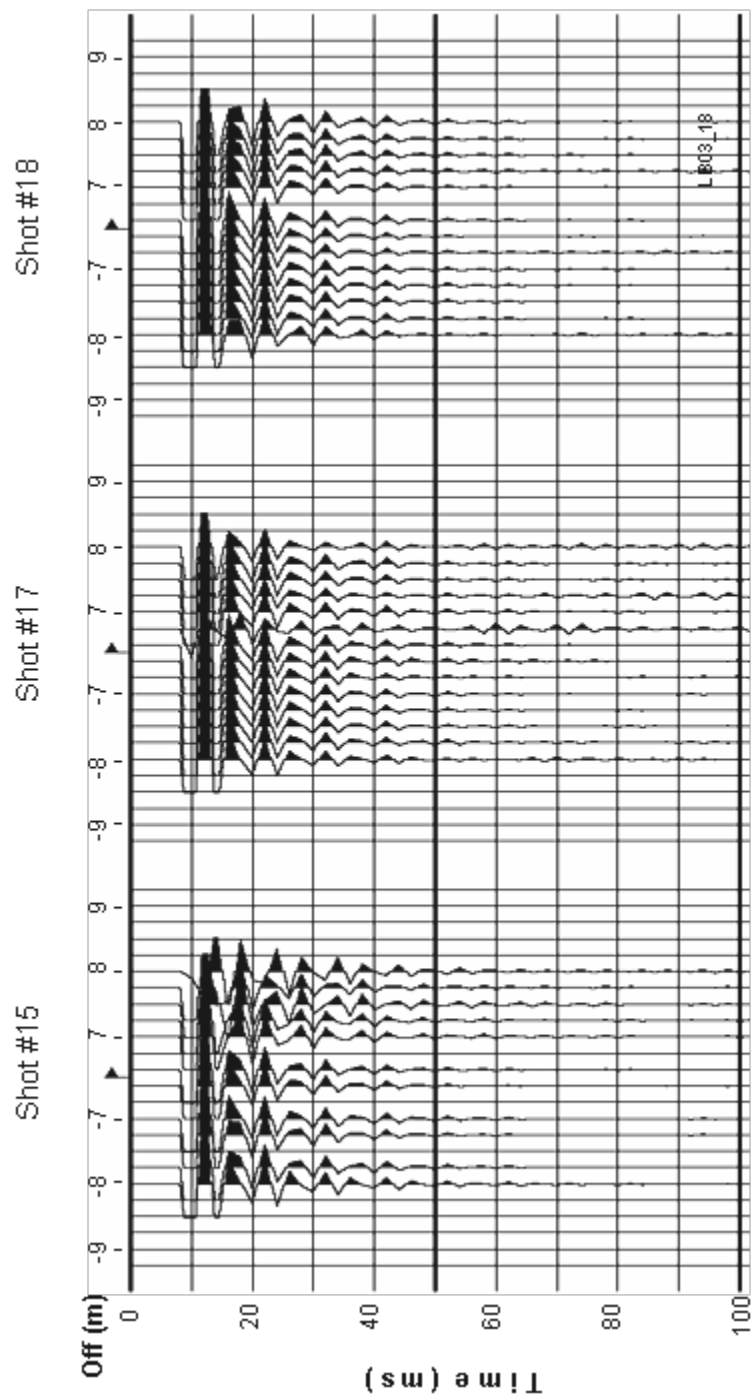


Figure 5.11. Filtered seismoelectric data from LB03. The data were acquired from three slightly different shot locations. A 200 – 600 Hz Butterworth zero phase band-pass filter was applied. Note that time at impact (trigger) is 10 ms. There are at least several seismoelectric signals from 1.5 to 26 ms after impact. Later signals are not truly simultaneous.

There are ten interfaces that appear in the logs of Figure 5.7 which can be classified into two main groups: geological and geophysical interfaces. The geological interfaces are the lithology apparently displayed on the geological log which are sandy clay to sand, sand to clayey sand, clayey sand to sand, sand to peaty sand, peaty sand to silty sand, and silty sand to saprolite/granite basement at 1, 2, 6, 18, 32, and 52 m depth, respectively. Whereas the geophysical interfaces are the boundaries that are shown as a physical property change on geophysical log which are water table, and some significant changes of gamma and conductivity logs within sand and peaty sand layers at 5, 16, 21, and 28 m depth, respectively.

To see if it is plausible that these interfaces could be responsible for the simultaneous signals seen in the electrical data the depths of these interfaces (h_i) are converted to one way seismic travel time (t_j) using velocity model (V_i) obtained from seismic refraction above and compared to activity in the electrical responses. As the Type 2 seismoelectric signals propagate much faster than acoustic waves the depth of interface can be converted as one way seismic travel time. The expected travel times of the known geology and geophysics boundaries are determined by using

$$t_j = \sum_{i=1}^j \frac{h_i}{V_i} \quad 5.1$$

to yield expected arrival times of 1.4, 2.9, 6.1, 11.8, 17.7, and 26 ms, and 5.3, 11, 13.1, and 16 ms, respectively. The arrival times are then compared to the activity on the seismoelectric record (displayed in Figure 5.12) to achieve an acceptable and reasonable match to any seismoelectric events. All these data are summarized in Table 5.3.

Table 5.3. Depth to time conversion of geology and geophysical interfaces that appear in the log data of Pingrup.

Geology & Geophysics Interfaces (Log)	Depth (m)	Transit Time Conversion (ms)	Label
• sandy clay – sand	1	1.4	A
• sand – clayey sand	2	2.9	B
• water table	5	5.3	C
• clayey sand – sand	6	6.1	-
• the conductivity and gamma log dramatically changes			
- within sand layer	16	11	D
- within peaty sand layer	21	13.1	E
- within peaty sand layer	28	16	F
• sand – peaty sand	18	11.8	-
• peaty sand – silty sand	32	17.7	G
• silty sand – saprolite	52	26	H

From table 5.3 there are eight anticipated seismoelectric events in Figure 5.12, which I have labeled A through H arriving at 1.4, 2.9, 5.3, 11, 13.1, 16, 17.7, and 26 ms after impact. All of the projected signal arrival times do plausibly correspond to the onset of an electrical signal. These electrical signals at these times are measured to be simultaneous and are interpreted to be electrokinetic signals from interfaces because it fulfills the first group of criteria described in the end of Chapter 4. The A event has the strongest electric field amplitude due to its proximity to the surface (earliest arrival time). The measured apparent velocity of 56,000 m/s for signal A and very large (immeasurably fast) velocity for other signals are within the expected velocity range of EM (electromagnetic) disturbance in a moderately conductive medium. The highly saline nature of the area appears to significantly decrease the amplitude of the signals, where it ranges from milli to micro-V/m. However, the saline environment also means that the ambient noise was also significantly lower than seen (and reported) elsewhere. Water salinity and fluid chemistry appear to be the most dominant aspects to influence the rocks

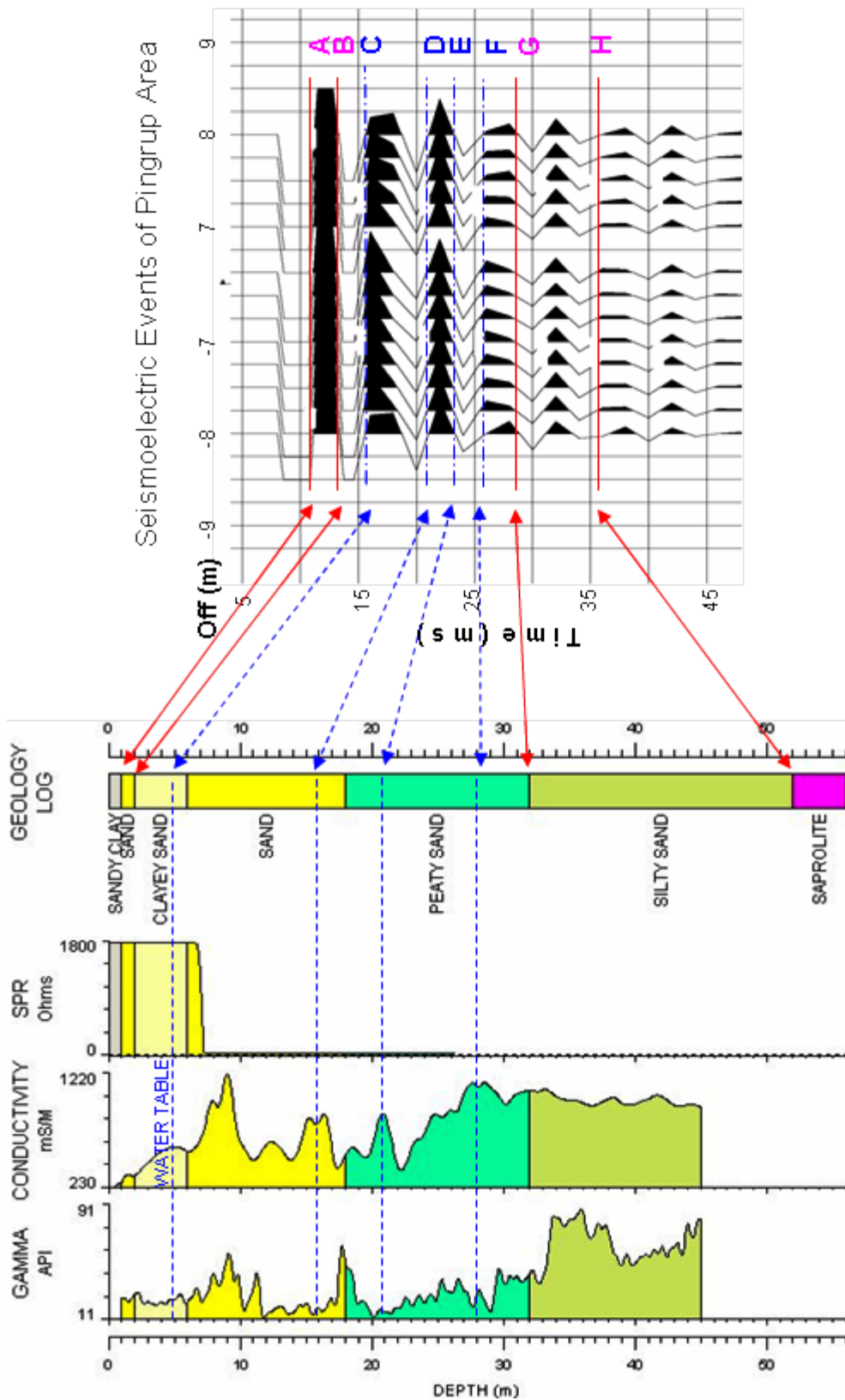


Figure 5.12. Enlarged view of LB03 shot #118 (of Figure 5.11). It shows high frequency simultaneous signals with very high apparent velocity that might come from interfaces. The geology (bold-red lines) and geophysics (dashed-blue lines) interfaces are interpreted to match the events. There are two geological boundaries (clayey sand to sand and sand to peaty sand) that are not well correlated with seismoelectric events. The maximum amplitude of events is approximately $10 \mu\text{V}/\text{m}$.

electrical conductivity. The seismic impedance contrasts between the clayey sand to sand and sand to peaty-sand boundaries, might not be strong enough to produce a seismoelectric response as these two geological boundaries did not match any reasonable event.

The onset of electrical activity in Figure 5.12, event A, appears to be produced from density contrasts at an interface at 1 m depth associated with the boundary between the semi-saturated alluvial sandy clay and the sand layer. A semi-saturated sand to clayey sand interface may produces a change in signal character, but the onset coincides with the wavelet from event A. Note that the character of the electrical signals also appear to change when the seismic wave enters the water table at 5 m depth. The peaty-sand and silty sand boundary and the silty-sand to granite basement at 32 and 52 m depth (events G and H) produce distinct wavelets that would be readily interpreted. Changes between regions having a contrast in chemical properties rather than contrasts in seismic impedance appear to be cause of events G and H.

Geological log projections don't provide a good match or justification for the other group of four events, C, D, E and F. However, an examination of the natural gamma and induction log data suggests significant physical changes that were not observed by the geologist. The mapped times of these changes is a better match to the phase of the electrical signals, and these interpreted events appear to originate from geophysical contrasts at depths of 5, 16, 21, and 28 m. A contrast in fluid chemistry at the watertable is a possible cause for event C, but seismic impedance and electrical conductivity are also possible causes. An interface within a thick sand layer at 16 m could explain the phase of electrical signal better than the mapped time of the sand-peaty sand interface. Alternatively, the depth of this interface may be better mapped with a geophysical tool than with an eye. The other two possible events, E and F, are similar to event D in that these possible events are strongly associated with increasing conductivity at 21 and 28 m depth within a peaty sand layer. However, whilst there is a reasonable case that the electrical signal changes character and phase to some degree with events D and F, there is less evidence of such a case with E. The physical log data indicates that the presence of

peat appears to affect the conductivity more than the clay content. Thus most of the electrical signal changes appear to be related to changes that contrast in water salinity rather than contrast in seismic impedance.

5.3.3 LB03 AVO Analysis

As there are eight possible seismic-to-electric signals that have already fulfilled the first group of EKS criteria, these signals are seismoelectric events that could arise from one or many boundaries. That is, even distinct events may come from the same interface via reflections of deeper interfaces and convert again. A good means to check whether signals separated in time can be attributed to the same interface is to perform AVO (Amplitude Variation with Offset) analysis. The methodology described in Chapter 4 was applied to the Pingrup data and assisted interpretation considerably in explaining the presence of deep seismoelectric conversions that were hard to explain given the very saline environment.

Figure 5.13 shows the shape of the electric field amplitude as a function of offset from Lake Bryde (LB) record for the interpreted events. There are eight AVO curves plotted in Figure 5.13. However, there are only five different amplitude peaks that can be uniquely associated with interfaces at greater depths of Lake Bryde site. The curves show that the maximum amplitude migrates further away from the shot-point as events become later in time, and the bell-shape lobes become broader as well. These observations strongly suggest that the series of electrical signals recorded in the field were generated from different interfaces. The first arrival t_1 through fifth arrival t_5 in the LB data are believed to originate from seismic-to-electric conversions that are associated with events A, B, C, D, and E, respectively. Since the curves are quite similar in pattern and have the same maximum amplitude position, the sixth through eighth arrivals (F to H) in the LB data most likely arise from the same interface via multiple reflections. The multiple conversion might be taking place within the peaty sand unit as the seismic wave hits a strong physical contrast within this layer. Very high changes are present in both

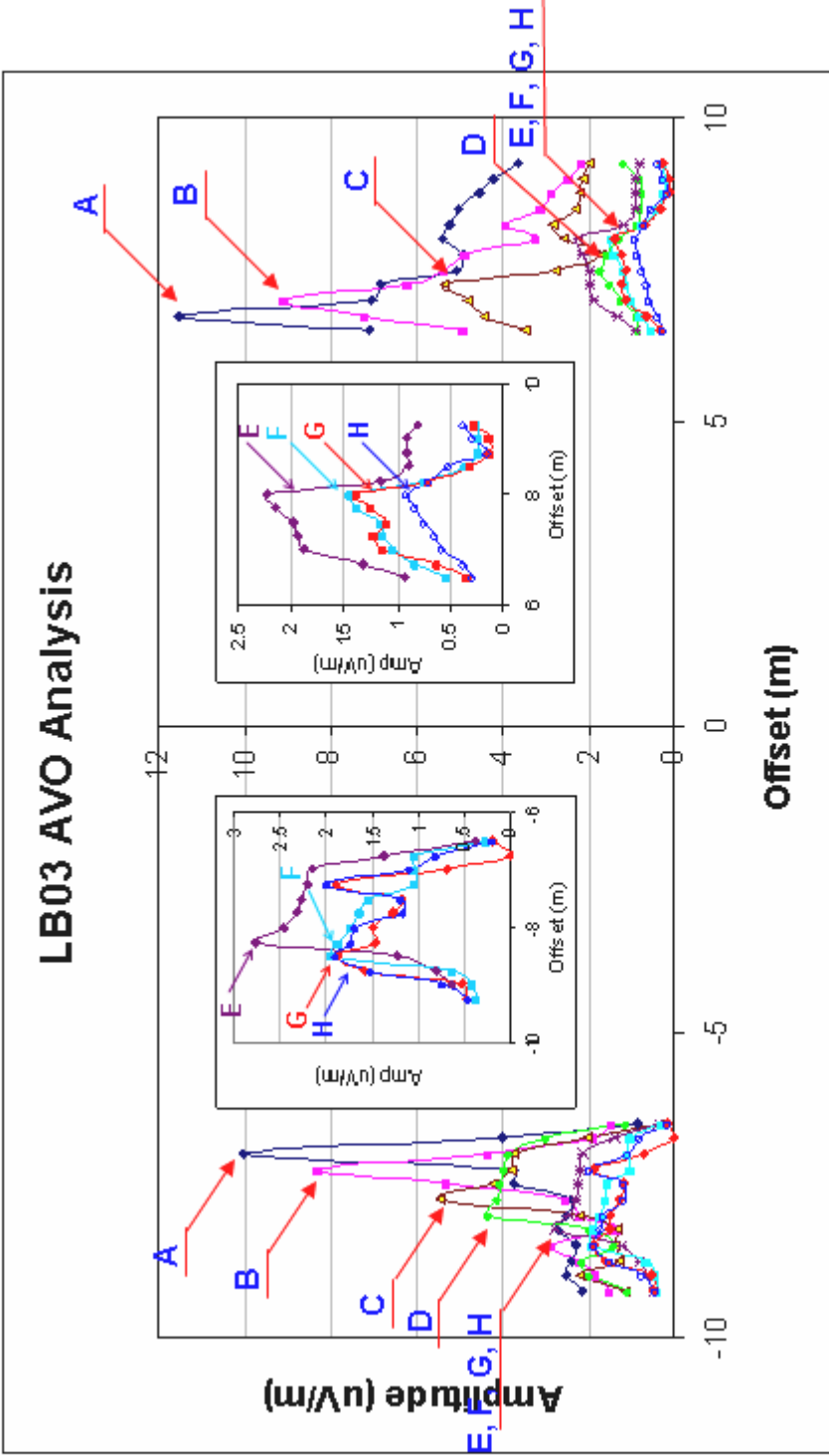


Figure 5.13. Electric field amplitude variation with offset plotted from Lake Bryde data. The first five curves (A, B, C, D, and E) are believed to originate from different interfaces. This is because the amplitudes and the peaks of curves become broader and move towards larger offsets. The last three curves (F, G, and H) are likely to be originate from the same interface (of E). The peaks of these curves are similar and are positioned at the same offset (see the inset).

conductivity and gamma logs at a depth of 21m. According to the AVO analysis the deepest interface that could be clearly detected is 21 m. These five likely interfaces to produce conversions are semi-saturated alluvial sandy clay to sand (1m), sand to clayey sand (2m), the water table (5m), an interface where the rock conductivity was changed significantly (16 m), and a significant change in conductivity interface at 21m depth. The other three possible seismoelectric events, which appear at 16, 17.7 and 26 ms after the impact have the same characteristic AVO curve with event E and are interpreted as originating from a seismic multiple reflection and a conversion nearer to the surface than the event time indicates.

5.4 Experiments Near the Blackwood River, Nannup

5.4.1 Field and Hydrogeological Description

The sites of the field trials were located in a reforested area near the town of Nannup, approximately 300 km south of Perth, Western Australia. The survey area is part of the Blackwood River catchment, which is the largest river catchment in the southwest of Western Australia. The contemporary land surface is generally undulating, but rapid changes in elevation do occur, mainly from erosion of the lateritic terrain surface by tributaries to the Blackwood River. Based on the topography map shown on Figure 5.14, the elevation is approximately 100 m AHD (Australian Height Datum). The climate of the region is characterized by cool, wet winters and warm to hot dry summers. Vegetation in the area consists of native Karri, Jarrah and (introduced) pine forests. The area where the surveys were conducted is part of a Water Corporation zone reserved for future water extraction from a huge aquifer, the Yarragadee. This aquifer is within a large sequence of sands and gravels, more than several hundred metres thick. There are many logged boreholes in the area used for evaluating and monitoring the quality and the quantity of groundwater as well as for bores for future water production of up to 50 gigalitres per year.

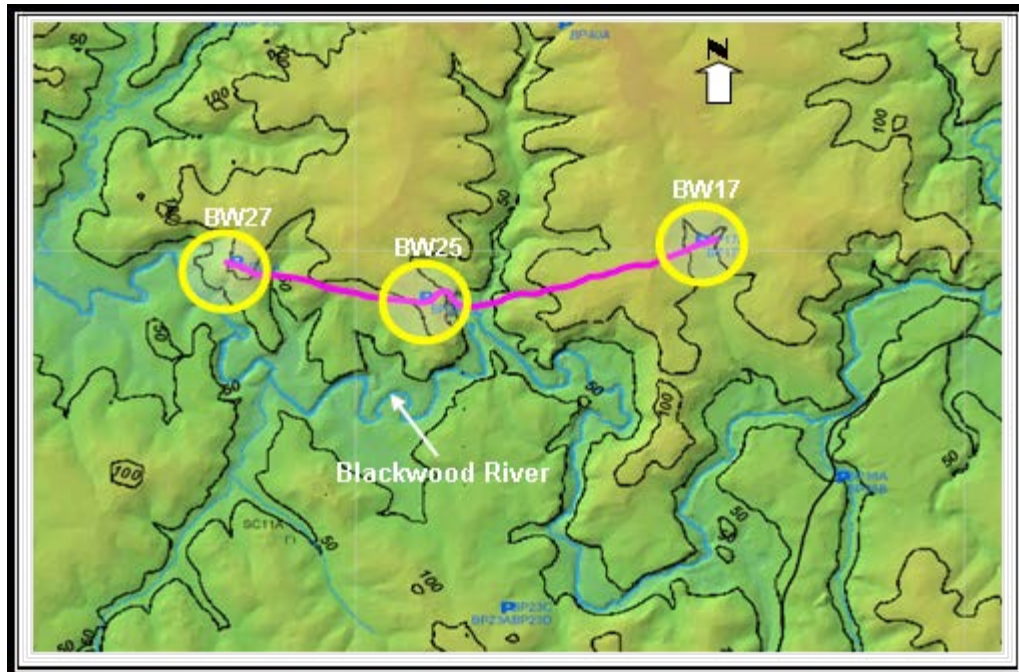


Figure 5.14. Topography of the Nannup survey area. Around boreholes BW17, BW25, and BW27 topography varies sharply, particularly in the vicinity of the river. Elevation varies from 0 to more than 100 m height. The site elevations of BW17, BW25 and BW27 are 90 m, 105 m, and 102 m AHD (map from Water Corporation, 2001).

The largest fresh aquifers are expected to lie within the Yarragadee formation. This formation is comprised of over 70% sandstone with interbedded siltstone and lesser amounts of shale and conglomerate present. Although the base of the formation has not been fully mapped, the 1250 m maximum thickness of the formation has already been intersected in KL7A borehole, and the base of this formation estimated at approximately –1600 m AHD (Baddock, 1995). The Yarragadee aquifer extends approximately 150 km north-south and is approximately 40 km wide and is a hydraulically connected aquifer. Another significant formation, the Leederville, overlies the Yarragadee formation in much of the area and is logged at some boreholes. The light shaded area on the map of Figure 5.15 is the main target area for hydrogeological investigations; where the Yarragadee formation is overlain by a perched aquifer within the near-surface Leederville formation. In addition to the geological and borehole log information, several moving

loop TEM surveys were conducted in the area at the same time, and provide additional resistivity information as well as some information between boreholes. Thus, this area seemed a suitable place to evaluate the seismoelectric method as it is of contemporary interest and has a wealth of supporting data.

Seismoelectric surveys were conducted near monitoring boreholes BW16, BW17, BW25, and BW27. The water salinity within the target aquifers were 200 to 1100 mg/L, with most less than 300 mg/L. This represents very fresh groundwater conditions (locally) except for borehole BW27 where the water is considered slightly saline (at 1100 mg/L). The main watertable is at approximately 67, 82 and 83m bgl (below ground level) for boreholes BW17, BW25 and BW27, respectively. However, a perched aquifer is present in all of these areas, but the levels are seasonally dependent. No water level or salinity data is available for borehole BW16. The estimated (by the Water Corporation, in 2002) main watertable level within the shaded area is shown in Figure 5.15.

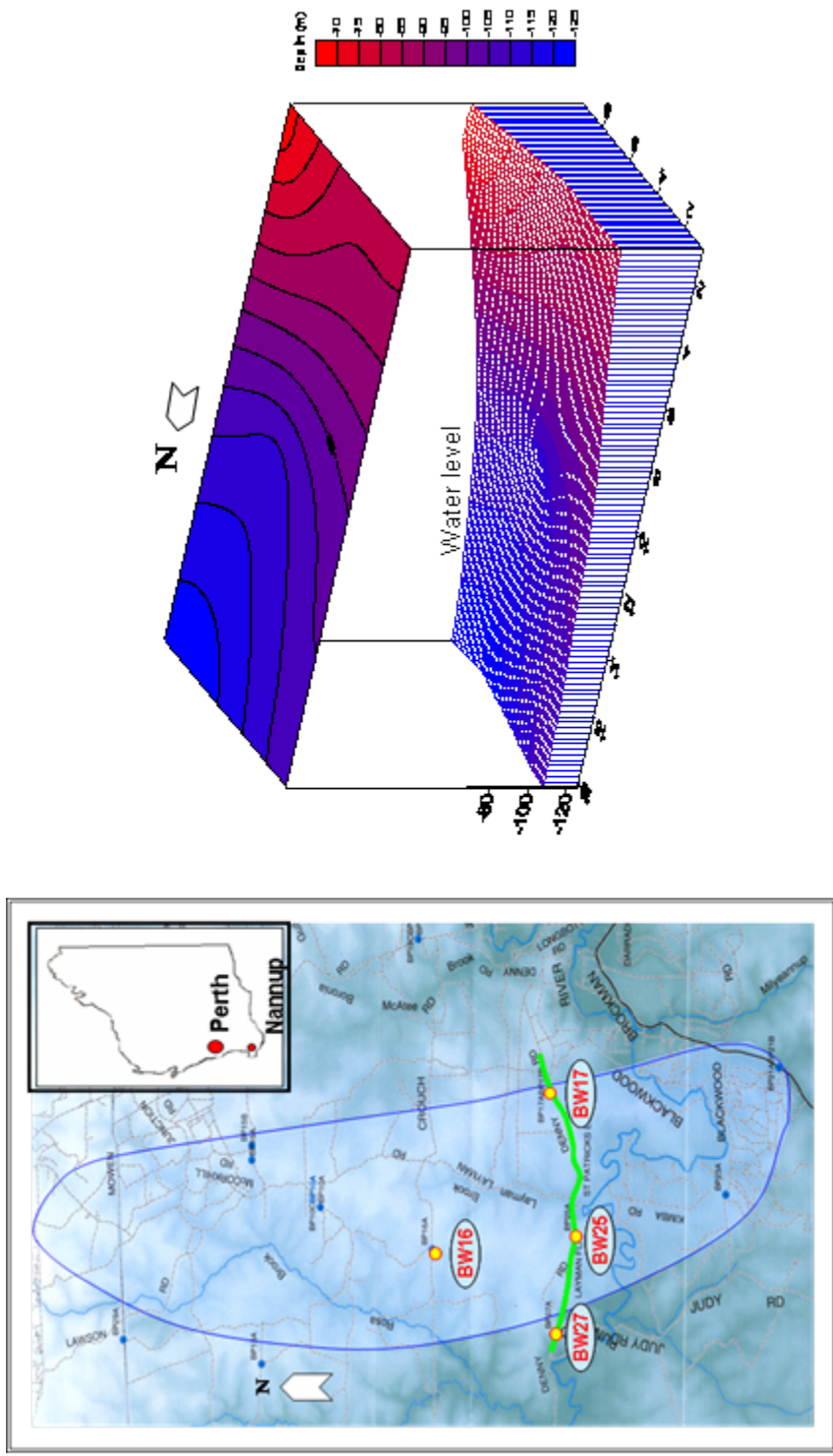


Figure 5.15. The local survey area (left). The light shaded areas show where a clay seal between the upper saturated Leederville formation and a partially unsaturated Yarragadee formation exists. The surface shows a North-South variation of watertable within the shaded area (right). As the topography of the water level in the South area is higher than in the North area the ground water flow is most in a Northerly direction; however, the superficial aquifers tend to flow into the Blackwood river system (map and water level data are from Water Corporation, personal communication, 2003).

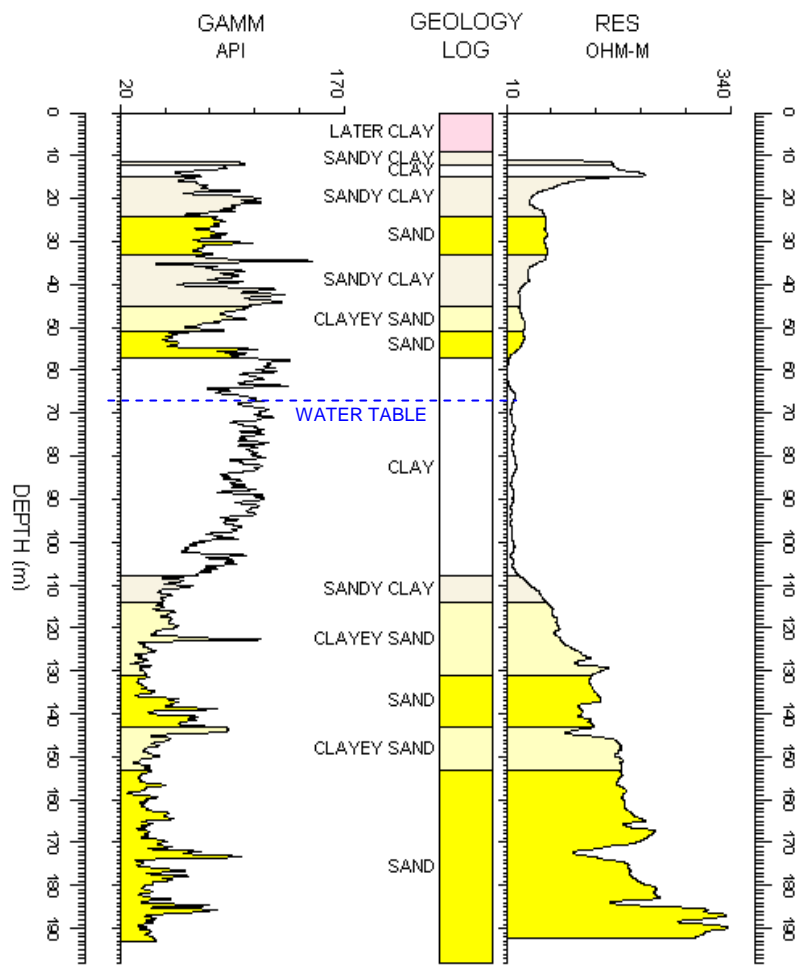


Figure 5.16. Borehole log data from BW17, Nannup site. The data consist of natural gamma, geology and resistivity log data (from left to right). In general, there are alternating clay and sand units that vary smoothly until the large basal sand unit is encountered. Note that the geophysical logs show more variability than the geological log. The water table is indicated at 67 m depth.

Figure 5.16 provides an example of borehole geological and geophysical log data from borehole BW17 as well as the lithology of the test area. The borehole is located approximately 5 m from the centre of the seismoelectric acquisition dipole spread. The stratigraphy is dominated by two materials, clay and sand, that alternate as follows: (i) a clay layer up to 24 m thick, (ii) a sand layer up to 9 m thick, (iii) another clay layer up to 12 m thick, (iv) another sand layer up to 12 m thick, (v) a thick clay layer up to 47 m thick (the seal between Leederville and Yarragadee), and (vi) a very thick sand layer base (up to several hundreds meters – part of the

Yarragadee formation). Physical property changes are more clearly seen in the geophysical log data rather than in the geological log. These data indicate that the alluvial sands are interbedded with clay layers. In addition, the water table of this area is at 67 m depth as indicated by moderate changes on both the gamma log and resistivity log. However, most of the formations above this level are at least partially saturated as evidenced by the seepage into nearby creeks. The sand-clay interfaces may have contrasts either in permeability, in electro-chemistry, or in elastic properties. Any of these changes may be sufficient to change the characteristic of both seismic and seismoelectric waves as they pass through the units.

5.4.2 Results and Discussion

5.4.2.1 Seismic Data

As with the Lake Bryde investigation, the velocity information at the Nannup site was extracted from independent seismic data. Both seismic refraction and near-surface seismic reflection surveys were carried out to support and compare to the seismoelectric data. The seismic data (as shown in Figure 5.17) were acquired using 24 geophones at 3-m spacing. A sledgehammer was the seismic source and 10 – 15 blows were stacked to produce a record. The shot points were located in both the split spread and end-on configurations to gather refraction data, and in a roll-along or common-midpoint configuration for reflection surveys. To provide reasonable velocity versus depth information the refraction shot points were located in 5 different positions: -31 m and -10 m left of the first geophone, in the centre of the geophone array, and 10 m and 31 m right of the last geophone.

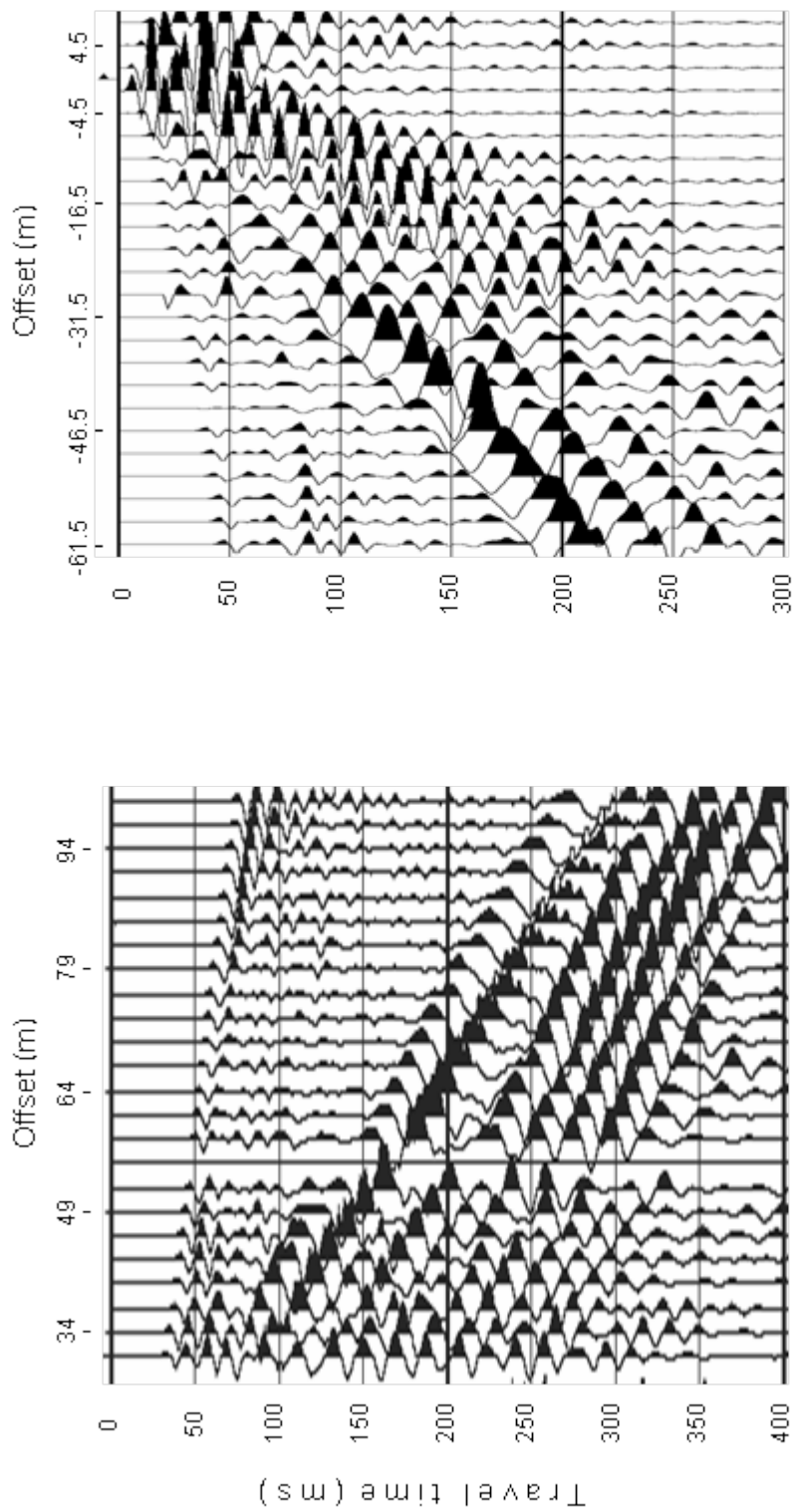


Figure 5.117. Example of raw seismic refraction (left) and reflection (right) shot record was acquired near bore-hole BW17. The data are the result of stacking 15 hammer blows. The refraction record recorded from a shot point deployed 31 m away from the 1st geophone. Both records were acquired with 24 geophones at 3-m spacing.

Seismic refraction data were used to obtain a one dimensional velocity model for later seismoelectric interpretation. Analysis of first break picks of the seismic data acquired near BW17 (Figure 5.18) yields four near-surface layers. A very shallow semi-saturated layer was identified distinctly from the other seismic records (i.e. when the 24 geophones were deployed at 1-m spacing). Thus, five near-surface layers were identified as seismic refractors. With respect to the geological log, these layers were situated in the partially saturated zone and may be attributable to: road fill, a very coarse to fine sand laterite unit, a sandy clay, a sand unit, and another sandy clay layer. The apparent velocities were 250, 720, 1860, 2010 and 2800 m/s respectively. The layers are relatively flat with thicknesses of 0.9, 2.8, 6.9, and 7.8 m (tabulated in Table 5.4). Note that the velocities indicate that formations are largely saturated at depths greater than 4m; thus, it cannot be assumed that the watertable depths in the borehole log are an accurate indication of the state of water saturation in the near-surface. Also, the velocity of the lowest layer (found in refraction data) indicates that the sandy clay formation is at least partially cemented as the velocities of sand/clay mixes should be about 1800-2200 m/s if unconsolidated (Lankston, 1990).

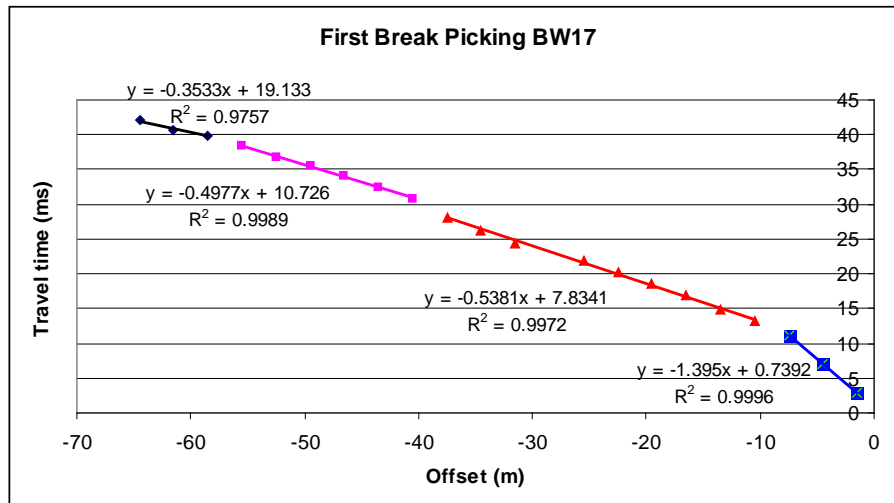


Figure 5.18. First break curve from a seismic refraction record at BW17. There are four linear curves that represent four different layers.

Table 5.4. The velocity model obtained from BW17 seismic refraction data

V_{app} (m/s)	Thicknesses (m)	Depth of top layer (m)
$V_1 = 250$	$Z_1 = 0.9$	0
$V_2 = 720$	$Z_2 = 2.8$	0.9
$V_3 = 1860$	$Z_3 = 6.9$	3.7
$V_4 = 2010$	$Z_4 = 7.8$	10.6
$V_5 = 2800$	$Z_5 = \sim$	18.4

The seismic reflection data from near borehole BW17 were processed using proMAX version 6.2 (from Landmark) to produce a “brute-stack” seismic section (no static corrections applied and no migration applied) that was subsequently interpreted (Figure 5.19). The data were processed with a 4-layer velocity model derived by semblance analysis, where the layers were assigned the following velocities as shown at Table 5.5.

There are to be nine distinct interfaces in the near surface that appear in the seismic reflection section and these can be associated with formations in the geological log. These layers can be designated: the top of a sandy clay layer, a sand unit, a sandy clay, a clayey sand, sand, a thick clay unit, another clayey sand, sand, and another clayey sand. The locations of these layers are at 15, 24, 33, 43, 51, 56, 116, 130 and 142 m depth, respectively. All of these layers overlie a thick sand unit that is expected to be the main aquifer of the Yarragadee formation. Seismic reflection data, in Figure 5.19, shows no clear layer between depths of 55 m to 100 m. This “zone of no reflection” confirms the presence of the clay unit approximately 50 m thick seen in the geological log (Figure 5.16 above) at these depths.

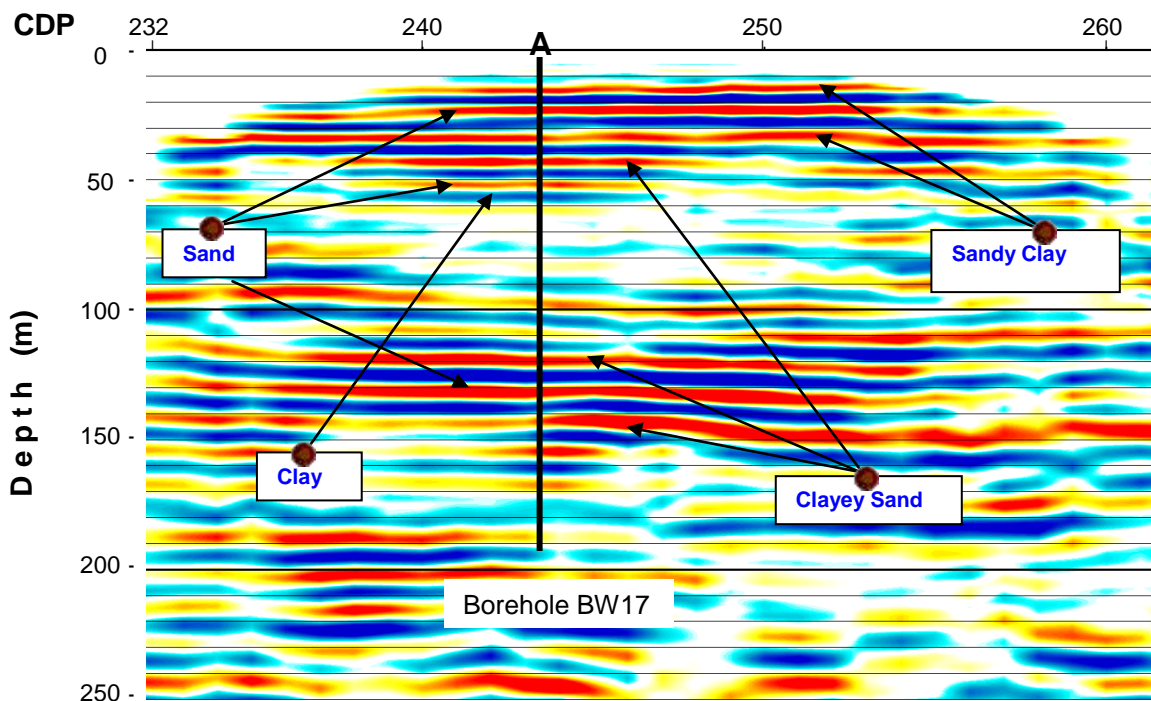


Figure 5.19. Interpreted near-surface brute stack seismic section obtained around borehole BW17. The borehole (depth of 198 m) is located in the middle of the section. There are nine identified layers where the deepest layer is located at 142 m depth. No layers are apparent between 50 and 100 m depth. A large clay unit of 50 m thick was confirmed by geological log data.

Table 5.5. The stacking velocity model obtained from seismic reflection processing

Layer	Two Way Time range (ms)	Velocity (m/s)
1	0 - 100	500
2	100 - 300	1200
3	300 - 400	2000
4	> 400	2500

There is a slight difference in the velocity models given by the seismic refraction and seismic reflection data. Note that the lowest layer in the refraction velocity model was generated from data from the last three geophones. However, stacking velocities are not considered particularly reliable either due to significant velocity variations (+/- 20% relative change) still providing much the same image. The refraction velocity model of BW17 represents the stratigraphy to approximately 19 m depth only, but on the other hand, the stacking velocity used for depth greater than 50 m in the seismic reflection data is 2500 m/s, which is in rough agreement. Therefore a velocity model having a velocity between 2500 and 2800 m/s is reasonable for depths greater than 20 m. An apparent velocity of 2800 m/s is a reasonable model to represent the partially consolidated sandy clay to saturated and consolidated clay unit (Lankston, 1990). Hence, the 5-layer velocity model from seismic refraction is used to provide depth conversion for interpreting the seismoelectric data.

5.4.2.2 Seismoelectric Data

Examples of unprocessed seismoelectric data records are displayed in Figure 5.20. The data were recorded around boreholes BW25, BW17 and BW27, which are kilometres apart. The shotpoint locations of sites BW25 and BW27 were set at offset with respect to the dipole array at 80 cm and 50 cm offset from the centre point of array, respectively. At BW17 the shotpoint was located at the center of dipole array, but offset perpendicularly 7 m away from the line. An example picture of how the seismoelectric data were acquired is shown in Figure 5.21. BW17 and BW27 data were recorded using the OYO DAS1 system with a 50 ms pre-trigger, whereas data from BW25 were recorded using a Bison 9500 system with no pre-trigger. Each record was a product of stacking 50 and 60 blows of a 5 kg hammer for BW25 and BW17 records, and 30 blows for the BW27 record. Powerline harmonic noise was effectively absent from all records except at BW17 data where 50 and 2500 Hz harmonics were present with maximum amplitudes of approximately 1100 μ V/m and 100 μ V/m, respectively. The raw electric-field

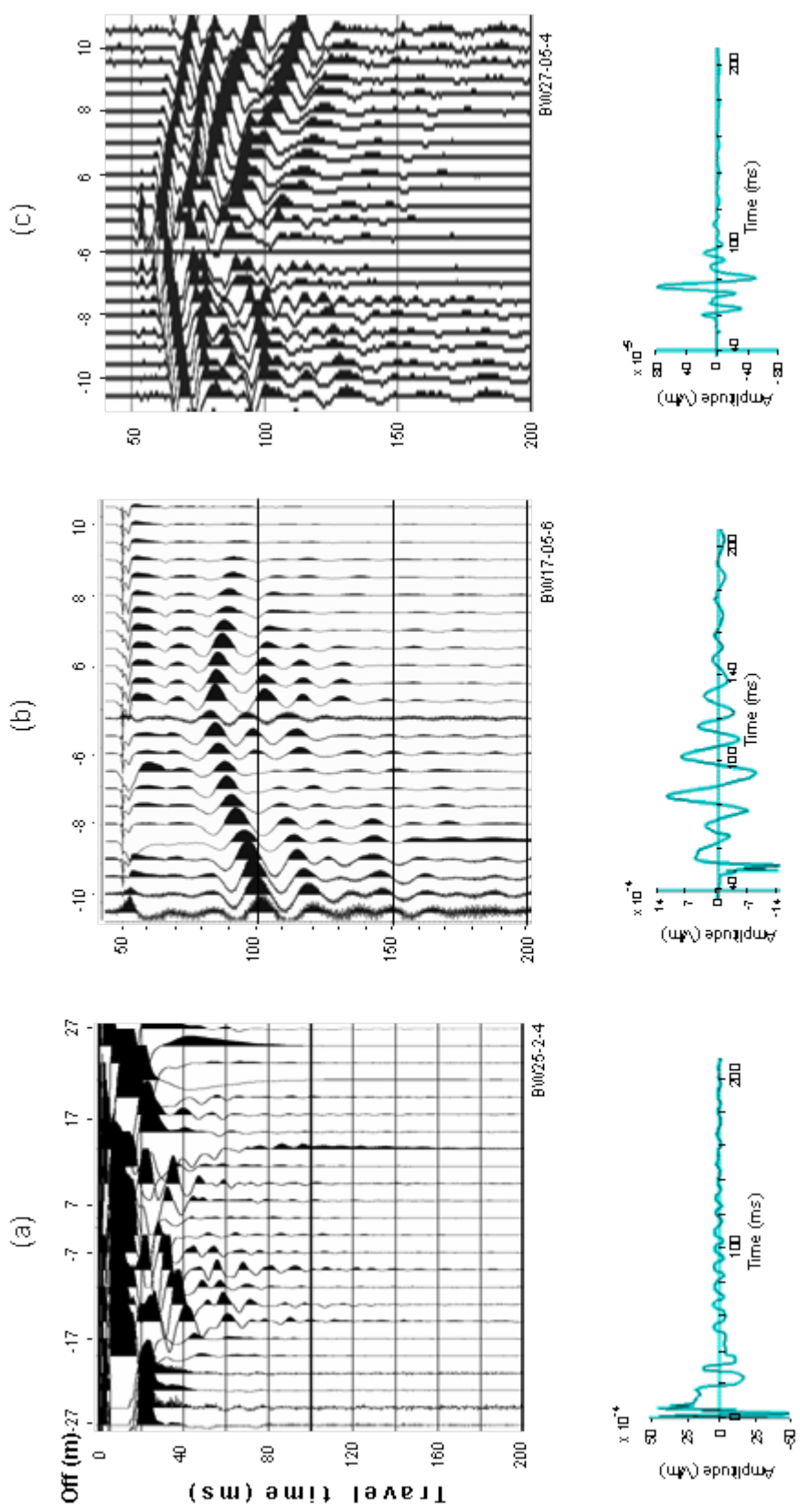


Figure 5.20. Raw seismoelectric data and their amplitude of signals acquired at BW25, BW17, and BW27 (from left to right). Impact times are at 0 ms at BW25 and 50 ms at BW17 and BW27. The recorded signals are generally dominated by ground roll wave. A high frequency noise (almost 200 Hz) also dominates the BW27 record as well as pre-trigger noise at BW25. The amplitudes of electrical signals are approximately 1.2, 1.3, and 0.8 milliV/m at BW25, BW17, and BW27.



Figure 5.21. This photograph shows the seismoelectric acquisition set-up at BW17. The dipoles were deployed in a split spread and overlapping configuration. Sixty blows of a 5 kg hammer were stacked to produce an EKS record. Note the borehole, BW17, is the blue pipe behind the truck.

amplitudes at BW25, BW17 and BW27 are approximately 1.2, 1.3, and 0.8 milliV/m, respectively. Note that the data from BW25 was severely contaminated by trigger noise that estimates of the seismic-related electrical signals are possibly more than a magnitude higher due to this interference. The electric activities in most records are due to seismic surface waves, and the amplitudes reflect the effect the fresh to saline environments of the near-surface groundwater has in scaling the Type 1 signal amplitudes. For example, the peak seismoelectric response at BW27, with higher salinity in the near-surface groundwater produces amplitudes an order of magnitude smaller than the other sites. As stated previously, the seismoelectric signal is reduced where the environment is more saline. Consequently, the smallest signals are measured at BW27. Also in common with the seismoelectric data from Lake Bryde, the signals in Figure 5.20(c) contain electric signals from direct compression waves, refractions near the electrodes, and electrokinetic signals from interfaces (which aren't visible with some processing). There are no detectable seismoelectric (Type 2) signals from interfaces beyond 80, 150 and 150 ms for the BW25, BW17 and BW27 records, respectively.

There are only few clear arrivals in the raw seismoelectric field data that take place essentially simultaneously across all antennas. Many of these are not a result from a seismoelectric conversion from an interface at depth. The strong pulses at time zero in seismoelectric records (at 0, 50, and 50 ms for BW25, BW17, and BW27, respectively) are rejected because these pulses are coincident with the impact as seen on the records (Figure 5.20). Other simultaneous signals are visible at 63 ms and at 100 ms in the example from BW17, and at around 53 ms in the example BW27 record.

The Type 2 seismoelectric signals, the type most easily associated with distinct geological interfaces, are masked by signals associated with various wave modes (ground-roll, refractions, and direct P-waves). The slightly large simultaneous pulses arriving 13 ms and 50 ms after blast at BW17 are most likely signals generated from interfaces at depth. The negative polarity of these signals on the right side of the shot point is clearer than on the left side. As was the case at Lake Bryde, these signals and other Type 2 seismoelectric signals only emerge after removing the low frequency noise using high pass filtering, in this case a 40 – 1000 Hz Ormsby minimum phase band-pass filter followed by a 150 – 800 Hz Butterworth minimum-phase band-pass filter. A series of high-frequency events that are repeatable reach all dipoles at approximately the same time and are evident at early time (as shown in Figure 5.22).

Figure 5.22 demonstrates the ability to consistently reproduce Type 2 seismoelectric signals (that occur at interfaces) in this location. Data acquired from BW17 had the source positioned at three slightly different locations: -50, -100 and 0 cm from the centre of array. Thirty hammer blows were stacked for shots #4 and #5 and 60 blows for #6. The configuration and the location of the dipoles are the same. The slight difference in source location makes little difference at depth, but was needed because the hammer and plate disturbed the ground considerably after so many blows (digging a considerable hole). Amplitudes of Type 2 signals decreases rapidly with time (depth) as would be expected from signals arising from deeper geological boundaries (Butler, 1996; Haartsen and Pride, 1997). The first two electric events have the largest amplitude due to proximity to the surface. These phenomena are consistent with the findings of Thompson and Gist (1993) and

Garambois and Dietrich (2001, 2002) that the amplitude of seismoelectric signals varies strongly with the depth and dip of interfaces. The maximum amplitude of these signals is around 700 microV/m. Most of the later signals (> 50 ms after impact) recorded at this site are interpreted to be noise as they were not consistently reproduced. Careful inspection of the apparent velocity is made on an enlarged portion of the shot record to check that the events are essentially simultaneous. Figure 5.23 displays some of the filtered data from Figure 5.22 over the interval 50 – 100 ms.

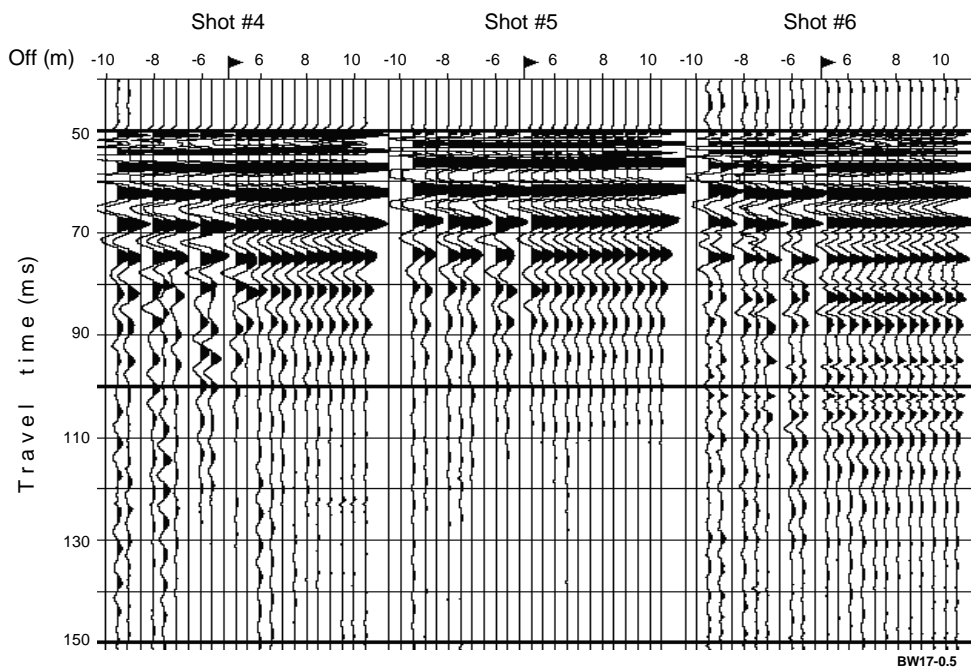


Figure 5.22. A series of Type 2 seismoelectric signals is consistently reproduced at BW17. The data were acquired from three slightly different shot positions but with the same 50 cm spaced dipole configuration. The data, which has time of impact at 50 ms, were processed using a Butterworth band-pass of 150 – 800 Hz minimum phase filter. The expected signals are in the range of 50 – 100 ms.

To obtain reasonable seismoelectric data interpretation a similar process to the Lake Bryde seismoelectric interpretation was carried out. The seismic refraction and reflection data and geological and geophysical log data shown in Figures 5.18, 5.19 and 5.16 were used to interpret the seismoelectric events. The depths of (fifteen) geological/geophysical interfaces were converted to seismic travel time. The estimated transit times are then embedded to filtered seismoelectric data shown in

Figure 5.23. As result the first eleven geology and geophysics boundaries are matched with possible seismoelectric events (i.e. transitions or phase changes in the electrical signals) labeled R through Z, and PP and QQ. The events R through Z could come from depths of 9, 15, 24, 33, 45, 51, 58, 107 and 113 m, respectively. Events PP and QQ possibly come from 67 and 85 m depth, respectively. The other four deeper geology boundaries are not matched with any seismoelectric events. The results are summarized and shown in Table 5.6.

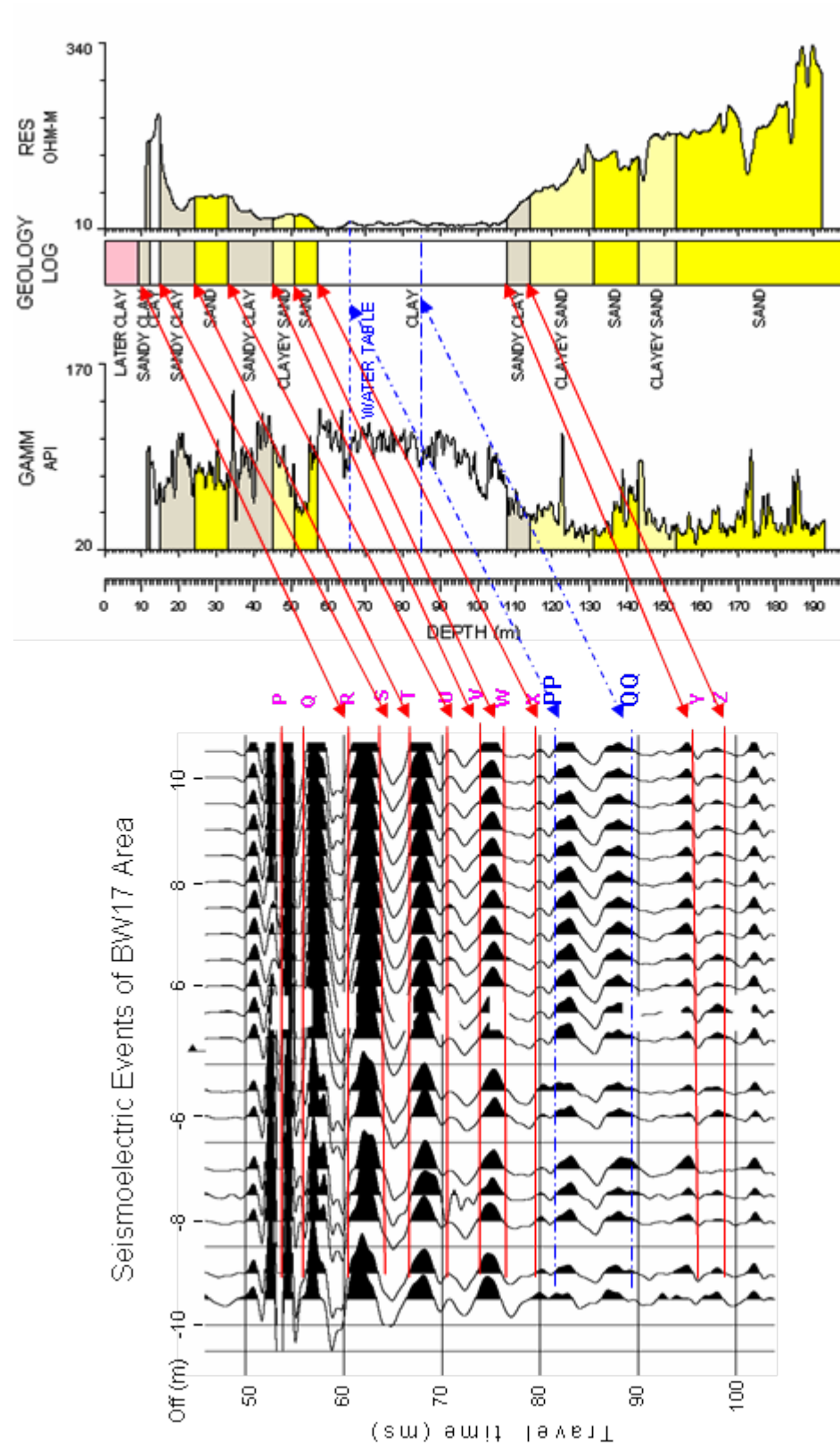


Figure 5.23. Enlarged and interpreted view of BW17 shot #6 records (in Figure 5.22). There are eleven geological (bold-red lines) and geophysical (dashed-blue lines) interfaces interpreted as being associated with EKS events. The maximum amplitude of the events is approximately $700 \mu\text{V/m}$. The event which is recorded at 82 ms is likely to correspond to the water table.

Table 5.6. Depth to (One Way) Time conversion of BW17 geological/geophysical logs.

Interface #	Geology Interface (Log)	Depth (m)	One Way Time Conversion (ms)	Label
1 st	laterite clay – sandy clay	9	10.3	R
2 nd	sandy clay – clay	12	11.9	-
3 rd	clay – sandy clay	15	13.4	S
4 th	sandy clay – sand	24	17.1	T
5 th	sand – sandy clay	33	20.3	U
6 th	sandy clay – clayey sand	45	24.6	V
7 th	clayey sand – sand	51	26.7	W
8 th	sand – clay	58	29.2	X
9 th	clay – sandy clay	107	46.7	Y
10 th	sandy clay – clayey sand	113	48.9	Z
11 th	clayey sand – sand	131	55.3	-
12 th	sand – clayey sand	143	59.6	-
13 th	clayey sand – sand	153	63.2	-
14 th	water table	67	32.4	PP
15 th	physical property changes	85	39.8	QQ

There are thirteen events that are simultaneous, have the correct polarity about the shotpoint, and are repeatable. These signals are interpreted to be seismoelectric signals from interfaces, and can be partitioned into two groups: eleven events appear to be associated with geological changes (bold lines) and an event with geophysical (dashed lines) changes. The geological boundaries associated with the events are labeled P through Z and occur at 3.8, 6, 10.3, 13.4, 17, 20.3, 24.6, 26.7, 29.2, 47 and 49 ms after impact. The two other events, PP and QQ, which might be correlated with other physical/chemical changes are identified at 32.4 and 39.8 ms after trigger time. The measured apparent velocities of more than 200,000 m/s for all of the events is in the expected velocity range of an EM disturbance at low frequencies in a superficial porous medium (average resistivity of about 400 ohm-m for the first 100

m; Sioni, 2003). The very fresh water environment may explain the relatively high amplitude of signals, which is in the range of sub milli-V/m. This amplitude (after filtering) is about 70 times greater than in the very saline-water seismoelectric signals measured at Lake Bryde.

Most events appear to have both geological and geophysical changes at the projected depths. The exceptions are the last two PP and QQ events which have a strong correlation with physical property changes only, but are only marked as being part of a clay unit in the geological log. As the pore fluid is fresh water, and very resistive, it is expected that the hydraulic conductivity (permeability) of rock may be the stronger influence upon the EKS streaming potential. Most of the events appear to be related to hydrogeological interfaces having a contrast in both impedance and permeability. The boundaries are, top-to-bottom (P to Z), base of road fill, very coarse laterite (like conglomerate) to fine sand, laterite clay to sandy clay, clay to sandy clay, sandy clay to sand, sand to sandy clay, sandy clay to clayey sand, clayey sand to sand, sand to clay layer, clay to sandy clay, and sandy clay to clayey sand unit at the depths given above. The existence of events P and Q relating to impedance contrasts is supported by notes of the driller's log as well as by seismic refraction as the upper, low velocity layers within a lateritic clay unit. Events S, T, through X were also confirmed by the 1st, 2nd, 3rd, 4th, 5th, and 6th layers/events in the brute-stack seismic reflection data. The S and W events, associated with (geological log) clay to sandy clay and clayey sand to sand interfaces at 15 and 51 m depths, respectively have negative polarity. However, increasing gamma ray counts in the log and decreasing resistivity normally indicate increasing clay content. Therefore, we expect that the S and W events are more likely due to the seismic P-wave passing through an interface with a permeability contrast (from permeable to relatively impermeable layer).

Two PP and QQ events (dashed lines at Figure 5.23) could not be matched to the geological log data. Thus, the natural gamma and induction logs were examined for evidence of physical property changes at the projected depths of these events. These events appear to be generated within a significant clay unit. The first event (which arrived 32 ms after impact) might be due to the chemical contrast of the (main) water table at a depth of 67 m. This high frequency signal was recorded relatively

strongly (compared to neighboring events). Another event (recorded at 39.8ms) could be associated with a change from higher clay content (increased gamma, decreased resistivity) to lower clay content at 85 m depth. This indicates that resistivity/conductivity changes may be the controlling factor, rather than changes in fluid-chemistry. Thus, the remaining two seismoelectric events might be caused by density and permeability contrasts rather than a contrast in water salinity.

5.4.2.3 BW17 AVO Analysis

An AVO analysis was implemented to ensure the thirteen events of BW17 above come from distinct interfaces. The absolute amplitudes of arrivals P through Z, PP and QQ as a function of source-receiver offsets were plotted in Figure 5.24. Only the first nine events, P, Q, R, S, T, U, V, X, and PP, fulfill the criteria for a non-multiple seismoelectric discussed in Chapter 4. Their curves are bell-shaped lobes with the maximum amplitude migrating away from the shot-point with arrival time, as well as the lobes becoming broader. Four of the possible events, W, QQ, Y, and Z, are likely multiple generated events as their AVO curves share the other events earlier in time. Thus, there are nine different interfaces that are identified to be associated with nine EKS events.

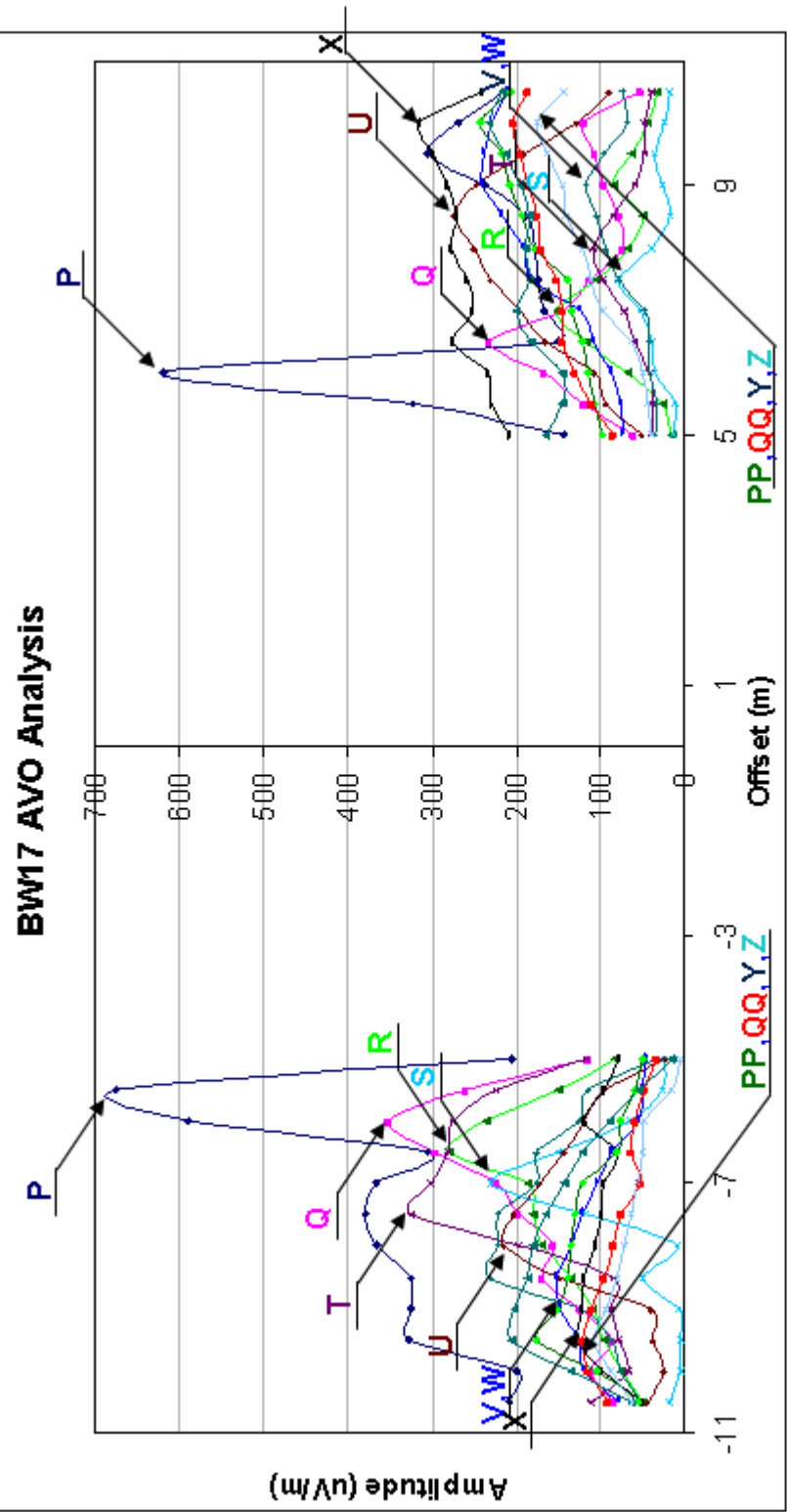


Figure 5.24. Analysis of amplitude as a function of shot point – dipole offset of BW17. Nine of the curves (P, Q, R, S, T, U, V, X, and PP) are clearly different in position, width, and amplitude. These curves are likely to be associated with nine different interfaces. The other four curves (W, Y, Z, and QQ) are interpreted as multiple events due to their similarity.

5.5 Enhancing the Data from BW16 and BW25 with a Virtual Shot Gather

The seismoelectric data at BW27 could not be processed and interpreted as easily as data from BW17. That is, separate the desired signal from the noise with a band-pass filter. In this survey area the first two metres of sediment is dominated by

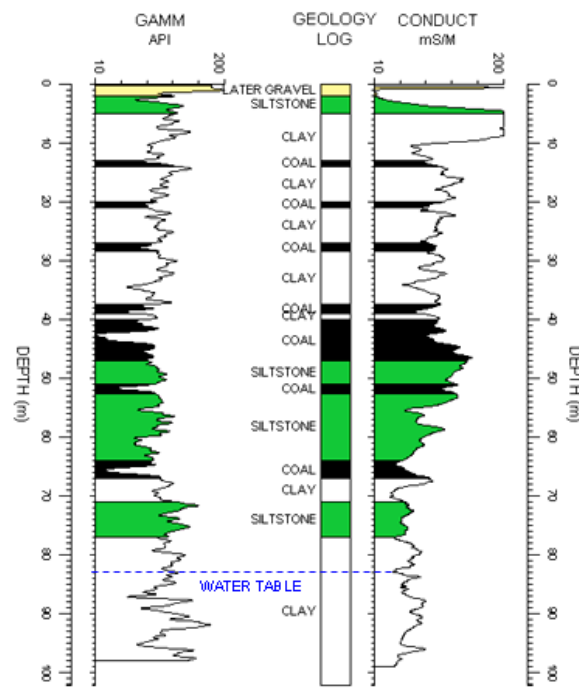


Figure 5.25. Geological and geophysical log data from BW27 Blackwood site showing that thin coal layers are interbedded within a large consolidated clay unit. The sandwiched coal is a low velocity zone within the clay layer and may generate guided/multiple waves.

lateritic gravel and conglomerates made from these gravels. This layer overlies a large clay-silt unit (more than 100 m thick) of the Leederville formation, which also has thin coal layers interbedded (Figure 5.25). Thus, the presence of both thin coal layers and cemented near-surface laterite gravel provides the possibility of strong guided waves and inter-bed multiples.

Not helping the seismoelectric method is the relatively high conductivity of this area, which results in smaller amplitude seismoelectric signals. This condition is

due to the relatively high salinity (1100 mg/L) and the clay-rich formations (dominated for up to first 40m depths). In addition, the very high frequency of the electric field (more than 200 Hz) that is associated with seismic surface waves made

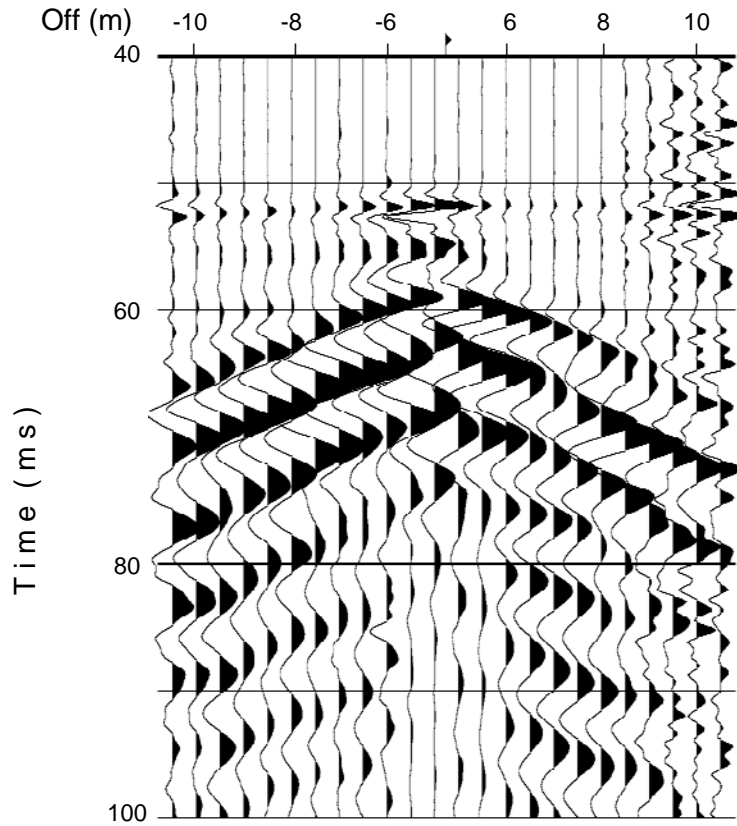


Figure 5.26. A processed seismoelectric record acquired from BW27 (see Figure 5.20 c) displaying very high frequency simultaneous seismoelectric signals taking place 2 ms after impact (time of impact is 50 ms) then followed by a plethora of high frequency guided waves. The waves are probably due to the presence of the strong acoustic impedance contrast of lateritic cemented-gravel to clay-silt unit.

a simple filtering approach unusable. Both a 150 – 1000 Hz high band-pass and various attempts at an f - k filter failed to separate out the seismoelectric signal (Type 2) from the seismic related signals. Relatively high frequency guided waves also still appear in the processed section 10 ms and more after impact (Figure 5.26). The Type 1 seismoelectric signals clearly exhibit move-out with seismic velocities, and

are similar to those seen at Nambi. There is a hint of the existence of high frequency simultaneous signals generated from boundaries at early times (first 10 ms after impact). However, the interfering signals contain a great deal of energy and cannot be removed without introducing serious artifacts in the data, which then cast doubt upon any remaining signals.

As f - k and τ - p filtering did not work with the original records an attempt was made to reacquire the data at a nearby borehole, BW25 (as BW27 was not accessible later), and at another borehole BW16 (in a new area for comparison). A new method of acquisition was attempted so that these methods may have a better chance at isolating the desired signals without producing numerous artifacts. To collect a record with better spatial sampling a virtual shot gather was constructed from five records. The aim of this virtual 120 channel shot record was to improve the effectiveness of later processing. The virtual shot was created by combining successive shot records from 24 dipoles after moving the shot point by small increments in the centre of the electrode array to emulate the effect of shifting all of the electric dipoles closer or further from the array centre. For the trial, 24 ground stakes were set in a staggered array with an offset of 2 m. Data merging from shot points at -80, -40, 0, 40, and 80 cm from the array centre is assumed to be equivalent to a single 120 channel record with 40 cm sampling. This type of record should allow velocity or move-out dependent filters to perform more effectively. The virtual 120 channels shot records are displayed in Figure 5.27 for BW16 and BW25. Unfortunately the trigger system of the Bison seismic system and the poor quality of the cables combined to produce spurious artifacts near and after time zero (with varying polarity), producing distracting interference, but the Type 1 seismoelectric signals are more clearly resolved in the virtual gather than in the raw 24 channel records.

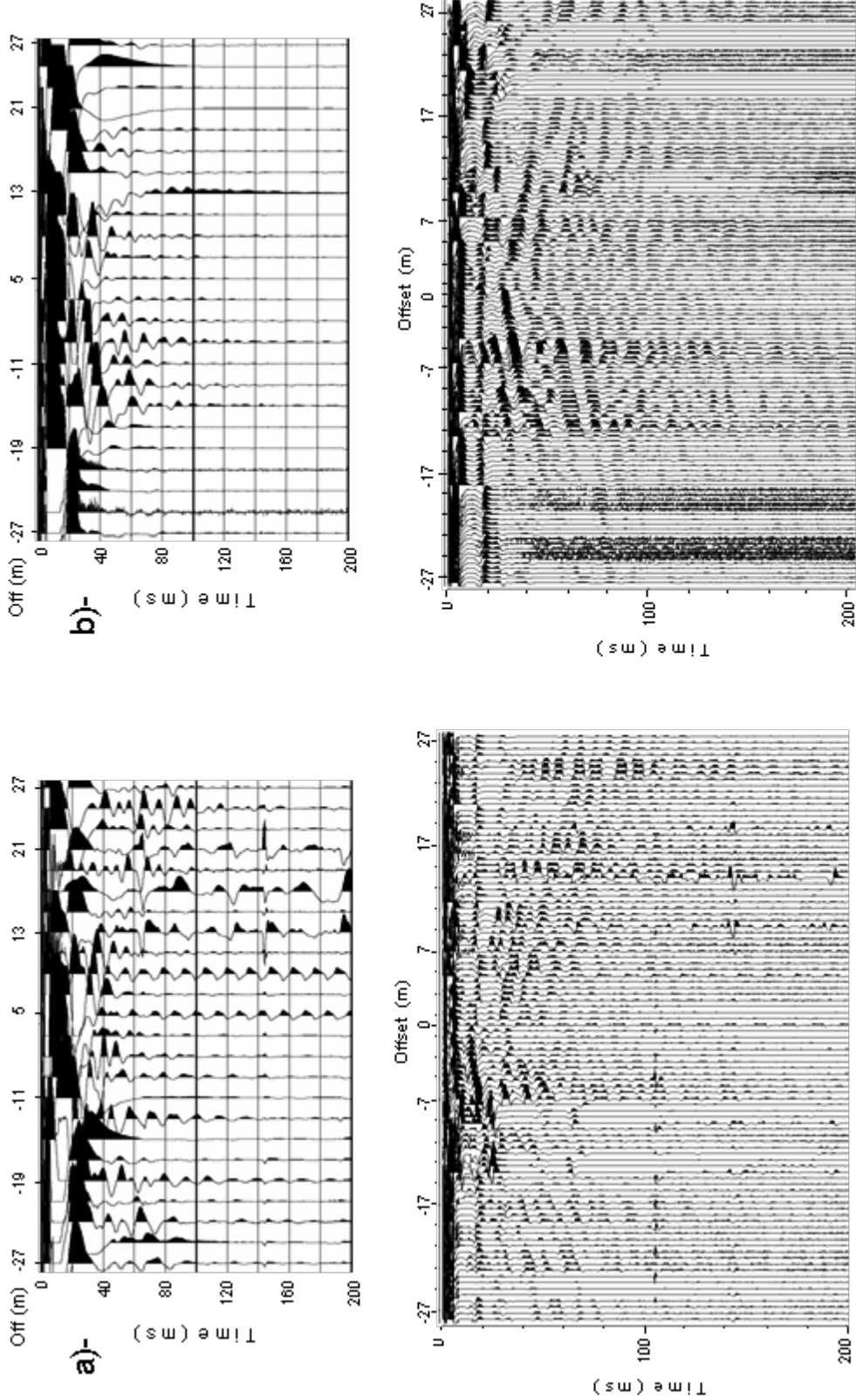
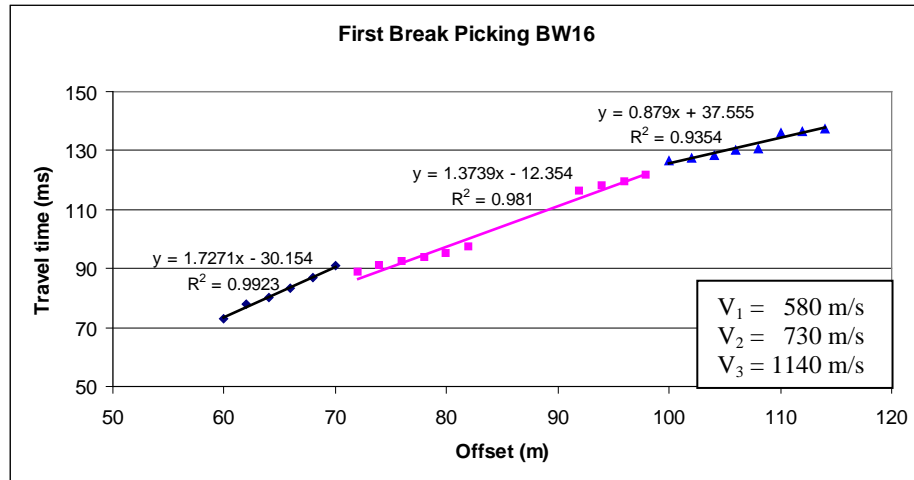


Figure 5.27. Raw seismoelectric data acquired from a)- BW16 and b)- BW25. The original records are shown at the top and the virtual 100+ channels shot record are shown below. The data was collected using 24 dipoles with 2m dipole spacing. A ‘dewow’ filter has been applied to the virtual short record for display purposes. Type 1 seismoelectric signals are more clearly resolved in the virtual records compared to the original record.

Seismic refraction data provided a velocity model to calculate and to interpret the seismoelectric events at both locations. The seismic refraction data were acquired using 24 geophones at 2-m spacing except the closest geophone offset from the centre of array at 5 m. To achieve deeper boundary target the shot points were deployed up to 60 m away from the 1st geophone. Ten to twenty blows of a sledgehammer were stacked to obtain a clear seismic record. Velocity analysis from first break picking of seismic refraction data for both the areas BW16 and BW25 are shown in Figure 5.28. There are three layers in the velocity models where the deepest of top layers are identified at about 28.5m for BW16, and 27.5m for BW25 (see Table 5.7). The velocity model at BW16 produces lower velocities than the BW25 or BW17 areas. Near to area of BW16 was a sizable gravel pit (full of lateritic pisoliths) used for road fill, indicating a sizable lateritic profile in the area. Laterite gravels are also found near BW25, but the gravel layers are less thick and appear to be well cemented in the near-surface. Moreover, the area near BW16 was drier than BW25 and BW17 according to the map of the perched water table produced by Water Corporation.

a)- BW16



b)- BW25

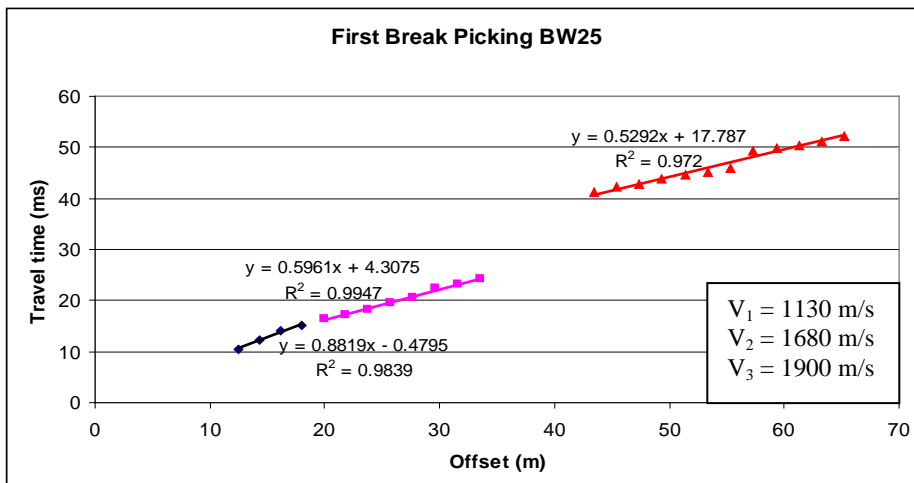


Figure 5.28. Time to offset curves of BW16 and BW25 for seismic refractions. The curves are used to obtain the P-wave velocity model. There are three layers in each area, where the deepest layer is up to 28.5m and 27.5m for BW16 and BW25, respectively. There are no data between 82 to 92m and 34 to 44m in Figure a) and b), respectively as the closest geophones offsets to the centre of array are 5m. The critical distance is at 22.5 and 43.5 m for BW16, and is at 6.7 and 97.5 m for BW25.

Table 5.7. P-wave velocity model of BW16 and BW25 from seismic refraction data.

V_{app} (m/s)	Thicknesses (m)	Depth of top layer (m)
BW16		
V ₁ = 580	Z ₁ = 8.5	0
V ₂ = 730	Z ₂ = 20	8.5
V ₃ = 1140	Z ₃ = ~	28.5
BW25		
V ₁ = 1130	Z ₁ = 3.7	0
V ₂ = 1680	Z ₂ = 23.8	3.7
V ₃ = 1900	Z ₃ = ~	27.5

The BW16 and BW25 seismoelectric data were interpreted similarly to the other EKS data sets previously presented. The depths of geological/geophysical interfaces (of BW16 and BW25) were converted to travel time applying the velocity model shown in Table 5.7. To evaluate any wavelets which may be associated to geological/geophysical interfaces, the converted times are then embedded to the seismoelectric record. A short seismoelectric interpretation and its relationship with seismic refraction results to correlate with geological and/or geophysical boundaries are tabulated in Tables 5.8 and 5.9, and displayed in Figures 5.29 and 5.30.

Table 5.8. Conversion of depth of (BW16 geology) interfaces to one way time (OWT) and the correlation with interpretation of filtered BW16 seismoelectric data.

Descriptions of geology/ geophysics boundary	Depth of interface (m)	OWT Conversion (ms)	Label
1. laterite clay – clay	3	5.2	-
2. clay – siltstone	8	13.8	AA
3. siltstone – silty clay	9	15.5	BB
4. silty clay – clay	13	20.8	CC
5. clay – sandy clay	16	24.9	DD
6. sandy clay – clay	26	38.6	EE
7. clay – sandy clay	31	44.2	FF
8. sandy clay – clay	40	52.1	-
9. clay – sand	45	56.5	-
10. sand – silty sand	57	67.1	-
11. silty sand – sand	59	68.8	-
12. sand – silty sand	75	82.8	-
13. silty sand – sand	87	93.4	-
14. sand – silty sand	94	99.5	-
15. silty sand – sand	95	100.4	-
16. sand – sandy clay	101	105.6	-

Table 5.9. Conversion of depth of (BW25 geology) interfaces to transit time and the correlation with interpretation of filtered BW25 seismoelectric data.

Descriptions of geology/ geophysics boundary	Depth of interface (m)	OWT Conversion (ms)	Label
1. laterite gravel – sand	3	2.7	-
2. sand – sandy clay	5	4	-
3. sandy clay – clay	9	6.4	-
4. clay – sandy clay	15	10	JJ
5. sandy clay – silty sand	22	14.2	-
6. silty sand – sand	32	19.8	KK
7. sand – clayey sand	36	21.9	LL
8. clayey sand – sand	39	23.5	-
9. sand – silty clay	47	27.7	-
10. silty clay – sand	52	30.3	MM
11. sand – silty sand	62	35.6	NN
12. silty sand – sand	66	37.7	-
13. sand – sandy silt	73	41.4	OO
14. sandy silt – sand	78	44	-
15. water table	83	46.7	-
16. sand – clayey sand	88	49.3	-

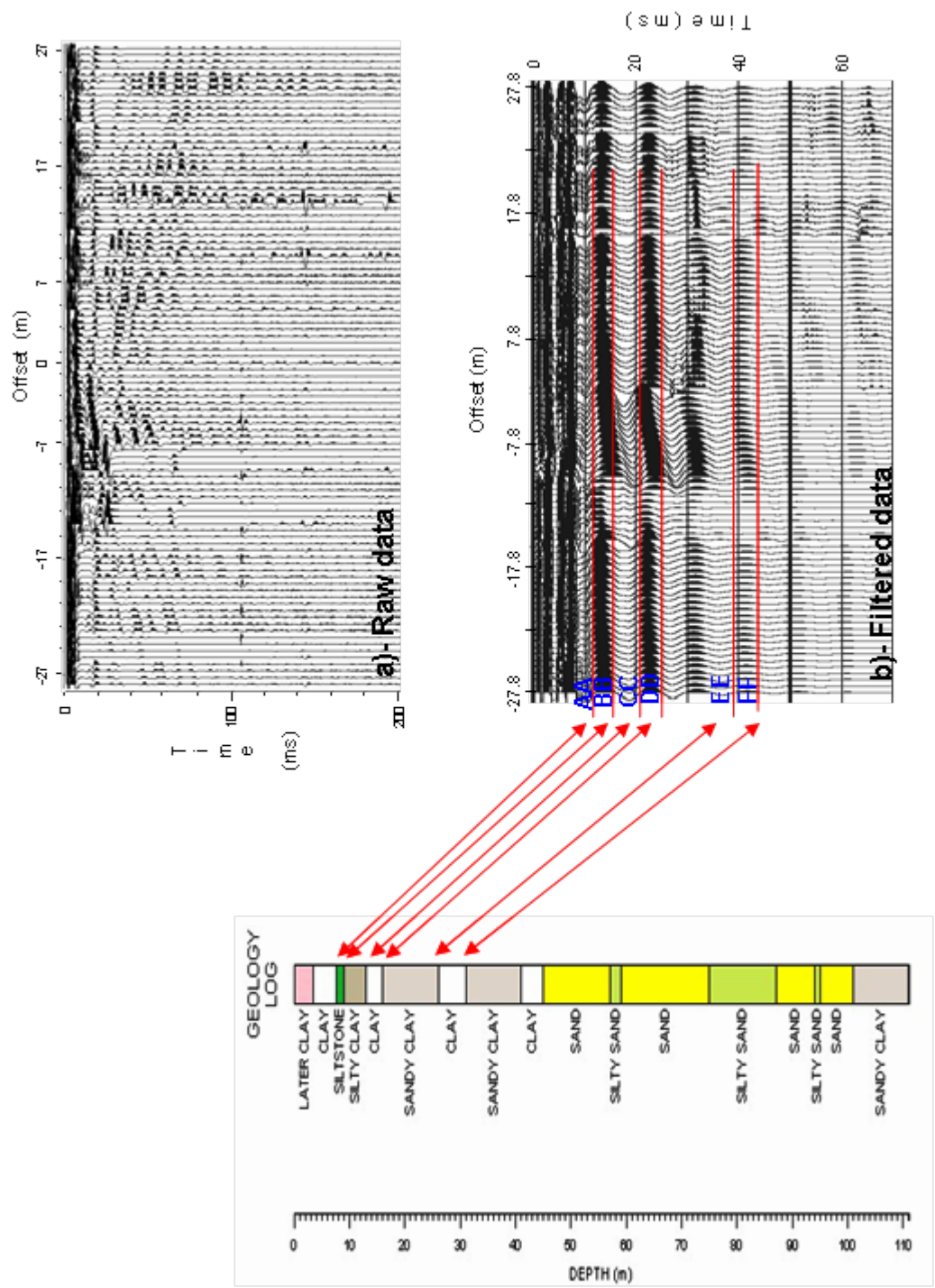


Figure 5.29. An example of seismolectric data from BW16. Figure a) is the EKS virtual 100+ channel shot record, and Figure b) is comparison between geological log data and the processed virtual shot record. The sequence of filtering was a high-pass filter of 100 Hz followed by $f-k$ filtering. An AGC with 100 ms window is applied before $f-k$ and then removed after $f-k$ filtering. After filtering only events with very high apparent velocities remain ($> 20,000$ m/s).

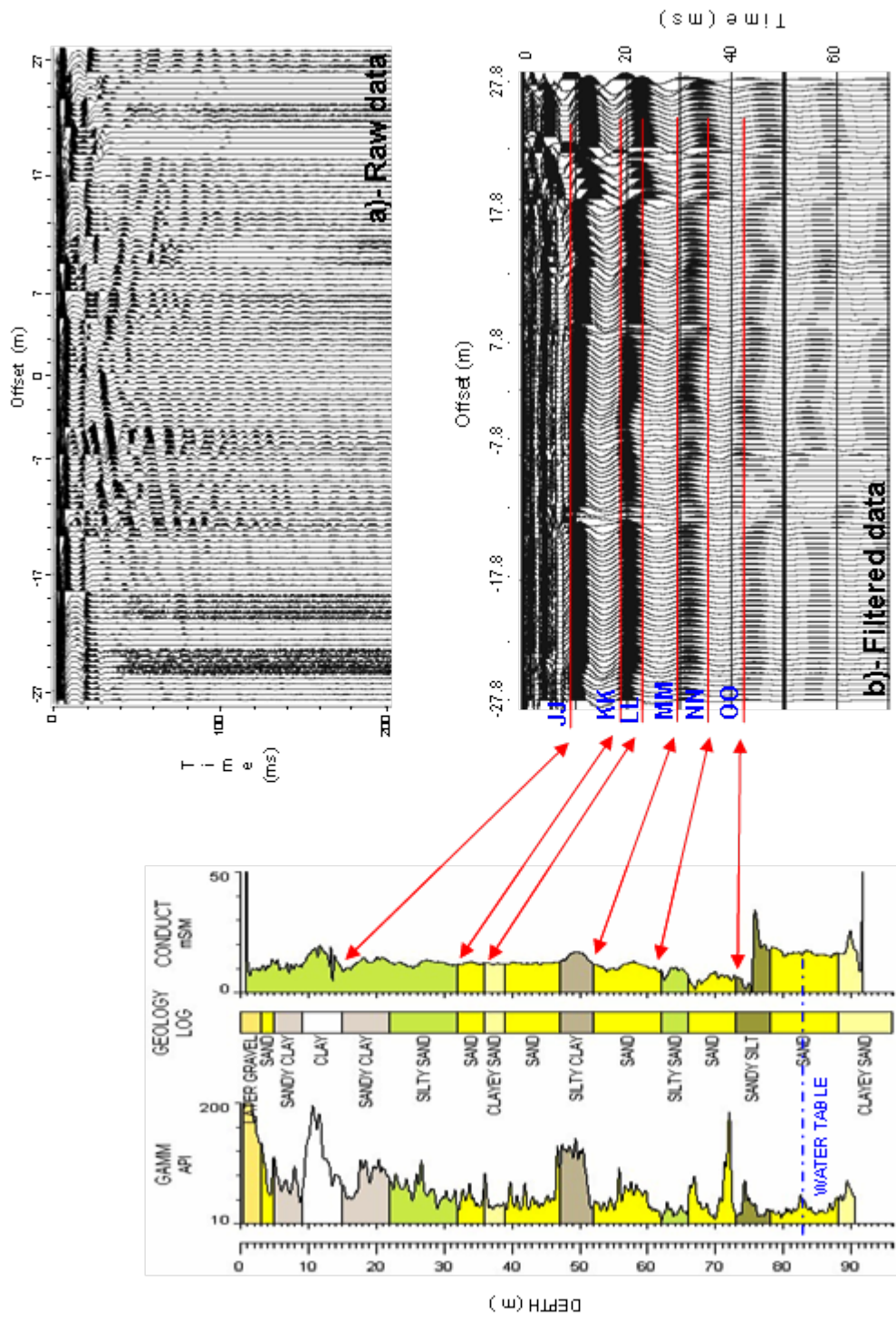


Figure 5.30. An example of seismolectric data from BW25. Processing was the same as for BW16. Figure a) is the raw record of EKS virtual 100+ channels, and Figure b) is a comparison between geological log data and the processed virtual shot record. Only six geological boundaries are interpreted to be correlated with seismolectric events. The events recorded in the first 8 ms could not be resolved (see Figure a). This is due to a problem in the trigger system, and poor quality seismic cable that produced distracting interference.

The events shown in Figures 5.29 and 5.30 appear to be generally correlated with boundaries having a significant contrast in porosity and permeability. Lithologically, both areas are dominated by a sand unit (which is expected to be the main aquifer) overlying clay sediment. Furthermore, the figures show that the alluvial sand layer is interbedded with thin silt, as well as clay layers. These interfaces have contrasts in either permeability, electrokinetic or elastic properties that may strongly affect the characteristics of both seismic and seismoelectric waves as they pass through. In fact, both Figures 5.29 and 5.30 show that most of the events are associated with these boundaries. As the areas have a fresh water environment the raw record peak electrical amplitudes are in the range of few milliV/m (approximately 1.3 mV/m for BW16 and 1.2 mV/m for BW25). However, most of signal in this record is the trigger noise which is an order of magnitude greater than the Type 1 seismoelectric signals evident in the records. Therefore, seimoelectric signals (of any type) are around 1mV/m or less in amplitude. The frequency range is between 80 and 220 Hz with 100 Hz being the most dominant frequency at BW16 and 90 Hz at BW25. The high frequency events appear at early arrival times (shallow event depths), whereas, the low frequency events tend to appear at later times in the records.

5.5.1 BW25 AVO Analysis

Data from BW25 data were also analyzed by using AVO curve analysis. The absolute amplitudes were picked and plotted as a function of shotpoint – antenna offsets. The AVO curves in Figure 5.31 shows that longer offsets result in clear broadening of the BW25 curves. The first through fourth arrival (JJ to MM) curves are quite symmetric, decreasing in amplitude versus arrival time, and the curve becomes broader with depth.

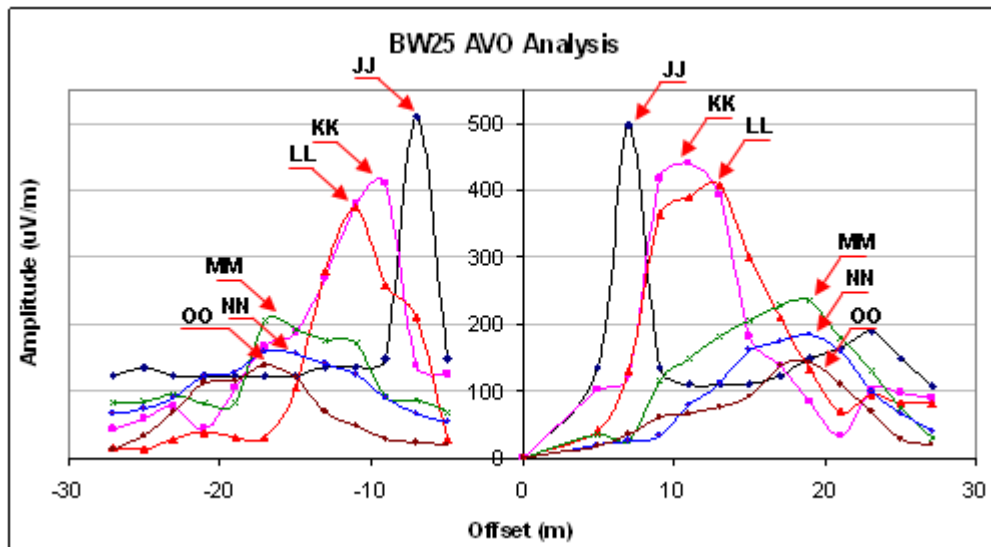


Figure 5.31. Analysis of amplitude variation with offset of BW25 Nannup data. The curves look symmetrical, especially at < 15m offsets. Four events (JJ, KK, LL, and MM) are interpreted to be from different interfaces as the bell shaped curves clearly change in both peak position and broaden. The last two events (NN and OO) are interpreted to be a multiple from the same interface due to similarity.

A number of these events plausibly result from seismic-to-electric conversion at the clay to sandy clay interface, silty sand to sand interface, sand to clayey sand interface and silty clay to sand interface at depths of 15, 32, 36 and 52 m, respectively (see Table 5.9). However, the last three curves are quite similar shape, indicating a multiple conversion. The source of this conversion is likely to be a layer of silty clay to sand interface at 51 m depth.

The broadening of the lobes of the AVO curves in previous analysis (in Figures 5.13 and 5.24) are not as great as would be expected theoretically. This may be due to the short range of offsets, which are 3 to 5 meters only. In contrast, the amplitude variations at BW25 are better exhibited as the range of offset was set much wider at up to 25m. In addition, since the effect of saline groundwater reduces the resultant electric field considerably; thus, the AVO curves signal-to-noise decrease markedly as shown in the Lake Bryde data. Amplitude variation with offset at Blackwood (especially at BW25 site) has greater signal-to-noise and a wider range of offsets than the data obtained from Lake Bryde. Thus, the shifting of the maximum

amplitude and broadening of the curves with depth is more pronounced (Figure 5.31 at BW25) due to fresh groundwater and the longer offsets measured in the data.

CHAPTER 6

CONCLUSIONS AND RECOMMENDATIONS

6.1 Conclusions

The existence of both Type 1 (electrical signals that are co-seismic, and travel with various seismic waves) and Type 2 (electrical signals originating from an interaction of the seismic wave with a geological change) seismoelectric responses based upon electrokinetic effects has been experimentally verified in our field experiments and further characterized. Seismoelectric data were successfully collected from environments with fresh and saline areas, saturated and unsaturated media, and shallow and deeper aquifers. These data were supported by other geophysical and geological data in their interpretation. The data acquisition methodology was refined after each of field tests and previous data reanalyzed when new approaches were devised. Thus, a new workflow and approach to producing, analyzing, and interpreting seismoelectric data has been produced with this thesis.

In general, Type 1 seismoelectric signals are identified strongly associated with direct waves, surface waves (such as ground roll/Rayleigh waves), multiple/guided waves, and head-waves. This type of signal exhibits a move-out of arrival time versus dipole position as it propagates with the velocity of the seismic waves causing the electrical response. However, the ground roll component is the most dominant seismoelectric signal of this type in our records. The highest amplitudes recorded are approximately 1.3 mV/m seen in the freshwater environment of the Nannup test area.

As predicted, Type 2 seismoelectric signals appear as simultaneous signals regardless of the position of the electrical sensor (dipole). This type of signal diffuses very quickly from interfaces with apparent velocities of more than 100 km/s; thus, these signals show almost no move-out with shot-to-receiver offset. These signals appear to be the most useful in determining hydrogeological properties as there is a physical theory that can be used to make predictions about their

behavior, and thus interpret the origin of their cause. The highest recorded amplitude of Type 2 signals in my field tests is approximately 0.7 millivolts/m in a near-surface freshwater environment. Signals as small as 1 microvolts/m were also reliably measured. A characteristic of Type 2 signals verified by my tests are that the signal amplitudes vary strongly with the depth to the interfaces. The events that emerged from different interfaces have amplitude-versus-offset curves that appear as two lopsided bell-shaped lobes that are symmetric about the shotpoint. This is the same shape predicted and observed by other researchers (Haartsen and Pride, 1997; Butler et al., 1996; Garambois and Dietrich 2001). Deeper interfaces produce a broader shape of electric fields on the surface and the amplitude maximum moves to longer offsets from the shotpoint. In addition, the amplitudes decrease substantially with depth of interface.

In my field experiments we was able to identify five significant hydrogeological boundaries up to 21 m deep in saline groundwater conditions, and up to nine interfaces up to 67 m deep in freshwater aquifers. These interfaces were identifiable in the geological and geophysical well-logs as well as in the near surface seismic section. Type 2 frequency signals were also shown to be able to respond to a layer as thin as 1 m. Moreover, the average signal strength is controlled by salinity of groundwater. Amplitudes of the signals of freshwater environment at Nanup BW17 were 70 times larger than the signals obtained in the saline environment at Lake Bryde LB03.

It was next to impossible to directly recognize the Type 2 simultaneous seismoelectric signals in our raw data records. These signals were always masked by Type 1 signals. To bring out the signal of interest, and to remove the low velocity and low frequency Type 1 signals either a band pass filter and/or an f - k filter needs to be applied on the raw data. In addition to frequency/spatial bandpass filters the harmonic subtraction technique (from Butler and Russell, 1993 and 2003) should be implemented when the power line noise is apparent in the raw data.

The signals that were interpreted to be associated with interfaces of geological or physical contrast appeared in both positive and negative polarities. Events with negative polarity (with our experiment set-up with positive electrodes closest to the

shotpoint) appear to be most correlated with interfaces of increasing clay content. Changes in clay content could lead to several important physical properties changes such as permeability, impedance, fluid-chemistry, and electrical conductivity. Close examination of the borehole log data and comparison to the seismoelectric responses (from Lake Bryde and Nannup datasets) indicates that it is interfaces with strong contrasts in permeability and seismic impedance that seem to be most attributable to the type responses seen at these sites. Thus, the method is sensitive to changes in hydraulic permeability and rock porosity. With regard to the (limited) data collected in this study, the negative polarity of events tended to occur when the seismic wave propagates through a permeable medium to a relatively impermeable medium.

Data from the Lake Bryde area demonstrated that the seismoelectric method is able to detect the changes in electrical conductivity. Conductivity changes due to water salinity changes were more dominant in producing seismoelectric events than the effect of more electrically conductive material (such as clay content) itself. Evidence of responses due to changes in salinity could be seen in the smaller amplitudes of seismoelectric response; whereas, the presence of a clay layer, appeared to have little influence in this regard and was more distinguishable via the polarity of seismoelectric event (believed to be due to the vast reduction in hydraulic permeability from sands to clays).

Some seismoelectric events are from interfaces above the water table and do not fit within the basic theory (for saturated media) outlined in Chapter 2. In fact, both types of seismoelectric signals (Type 1 and 2) are generated not only from fully saturated zones, but we have also recorded from interfaces within the semi-saturated (vadoze zone) or even the unsaturated zone. Almost all of the surveys were done during (or near) winter rainfall seasons and it might be expected that much of the near-surface is at least partially saturated during the measurements. It is noteworthy that whilst the work of Pride and Haartsen, (1996) is based upon the linking of seismic waves to electrical response via the constitutive equations of saturated media, the simple model put forward by Butler (1996) works well in this scenario as it only requires that there exist a linkage between the seismic and electric fields.

To collect seismoelectric data an overlapping electrode configuration is better than a series configuration. This configuration provides a longer the dipole length, which provides a larger potential difference. This configuration is better at avoiding spatially aliased data by virtue of greater sample density without reducing signal-to-noise ratio. For practical purposes the optimal configuration is a 50% overlap as there is a twofold reduction in possible spatial aliasing without containing too much signal in common with neighboring dipoles.

The measurement and preservation of very small seismoelectric signals in the presence of cultural noise that is usually much greater in amplitude is difficult. Therefore, the acquisition of seismoelectric data should consider these conditions as needed for success:

- a- ensure there is a good electrical contact between the stakes and ground;
- b- use a differential pre-amplifier to amplify and buffer the very weak signal;
- c- apply either good isolated cables or separate the cables each other as much as possible to avoid cross-communication noise;
- d- arrange the seismograph as far away as possible from both the dipole array and all other electrical sources to minimize the ambient noise; and
- e- use an energetic source or stack considerably to enhance the signal-to-noise ratio.

Eliminating Type 1 seismoelectric signals is of paramount importance. However, the best means to eliminate these signals is with a very high spatial sampling strategy (of the order of a 0.2 to 0.5 m dipole staggering) so that post-processing algorithms can eliminate this noise by exploiting the offset-time relationships between the types of signals. In data processing, the noise that is still observed in seismoelectric data records were eliminated or suppressed by using a sequence of filters such as the HSUB program, band-pass filter, and f - k filter. These filters need to have the parameters set so that ringing and artifacts are minimized. In particular, the band-pass filter and f - k filter need to be set for the specific case of extracting electric fields rather than any rules of thumb used for seismic data processing. The last step is to apply AVO analysis to ensure that the seismoelectric events arise from different interfaces. AVO curves can confirm that the deeper interfaces have the correct distribution of amplitudes and allow the recognition of multiple events.

A system with a fairly large channel capacity is needed to enable the f - k or τ - p filter to isolate the simultaneous signals and eliminate the interfering signals with a very narrow band-pass (in the f - k space). The relatively wide bandwidth of the interfering seismoelectric signals drives the need for dense spatial sampling of the signal. As this may require more than 80+ dipole sensors to gather sufficient shot-to-dipole offset it makes collecting seismoelectric data an expensive business in either time or capital. To avoid this dilemma a virtual shot gather method was developed and tested. A 24 channel system with 5 or more closely spaced shots produced a single shot record with an equivalent of 120+ channels of data. This data, while not of especially high quality, enabled the extraction of Type 2 seismoelectric signals from areas that beforehand could not provide interpretable records.

6.2 Recommendations

The present acquisition system, built from existing instruments and adaptations of other instruments was less than perfect. Setting of pre-amplifier gains, leakage currents from seismic cable, interfering electric fields from failed neighbor dipoles, positive feedback instability, cross-communication in cables were examples of field problems that consumed much attention during the acquisition. In terms of mobility and work efficiency in the field the (20 kg) BISON seismograph and its seismic cable (5 kg per 12 takeouts) was preferable to the OYO DAS-1 (150 kg including batteries and roll-box) with its 192 channel cable links (20 kg for 5 take-outs) despite the better data quality offered by the OYO system. Also, a set of mobile electrodes (capacitive coupling) would significantly improve productivity. Pre-amplifiers need to be stable and flexible given the great variance in near surface conditions and noise levels from site-to-site. A properly isolated distributed seismic acquisition system would improve the quality of data and speed the acquisition of field surveys.

Once the data has been collected with sufficient spatial sampling there is enormous scope for various algorithms to be applied to remove the co-seismic noise (Type 1

seismoelectric signals) and much research is yet to be done in this area. However, without proper sampling, it is clear that little can be done to extract the most interesting signals with the algorithms commonly available in seismic reflection processing software. The bane of this thesis was trying to remove these signals, and where there were strong near-surface co-seismic signals, it often proved an insurmountable problem. Clearly, dense spatial sampling strategies must be employed during acquisition, and further works into new algorithms to cope with this issue are needed.

In order to be used for commercial purposes we need do more to characterize the seismoelectric signal in relation to geological information. Further analysis of signal amplitude (AVO) is also important. It may lead to recognizing and mapping the hydrogeological boundaries without supporting borehole data (perhaps using a basic inversion scheme). Magnitude, polarity, phase, and frequency of signals are some parameters that might be used to characterize the signal in relation to physical properties. As the signal polarity can identify a permeable-to-impermeable boundary, other parameters (or a combination) may be able to identify a specific physical condition of the rock. Theoretically, data from the seismoelectric method directly correlates with hydraulic parameters; therefore, the seismoelectric signal should also be able to directly map changes in hydraulic permeability, rock porosity, or fluid chemistry. The electric signals from interfaces should be transformed to be information of hydraulic parameters. As the hydraulic parameters can be traced theoretically, seismoelectric modeling and inversion processing is an area for further work.

References

- Abramson, H.A., 1934, Electrokinetic Phenomena and Their Application to Biology and Medicine: *ACS Monograph Series*, No. **66**, Chemical Catalog Co., New York.
- Baddock, L. J., 1995, Geology and hydrogeology of the scott Coastal Plain, Perth Basin: *Western Australia Geological Survey*, Report 1995/7, 58p.
- Beamish, D., 1999, Characteristics of near surface electrokinetic coupling: *Geophys. J. Internat.*, **137**, 231-242.
- Biot, M.A., 1956a, Theory propagation of elastic waves in a fluid saturated porous solid. I. Low-frequency range: *J. Acoust. Soc. Am.*, **28**, 168 – 178.
- Biot, M.A., 1956b, Theory propagation of elastic waves in a fluid saturated porous solid. II. Higher-frequency range: *J. Acoust. Soc. Am.*, **28**, 179 – 191.
- Bishop, J.R., 1981, Piezoelectric effects in quartz-rich rocks: *Tectonophysics*, **77**, 297 – 321.
- Blau, L. W., and Statham, L., 1936, Method and apparatus for seismic-electric prospecting: *U.S. Patent No. 2054067*.
- Boulytchov, A., 2002, Seismic-electric benchmarking of caves and underground water horizons: *Expanded abstract, SEG Int'l Exposition and 72nd Annual Meeting*, Salt Lake City, Utah, USA, p. 1594 – 1597.
- Brace, W.F., and Orange, A.S., 1968a, Electrical resistivity changes in saturated rocks during fracture and frictional sliding: *Journal of Geophysical Research*, **73**, p.1433
- Brace, W.F., and Orange, A.S., 1968b, Further studies of the effects of pressure on electrical resistivity of rocks: *Journal of Geophysical Research*, **73**, p.5407.
- Broding, R.A., Buchanan, S.D. and Hearn, D.P., 1963, Field experiments on the electroseismic effect: *IEEE Trans. Geoscience Electronics*, **GE-1**, 23 – 31.

Burger, H.R., 1992, Exploration geophysics of the shallow subsurface, Prentice Hall, New Jersey.

Butler, K.E. and Russel, R.D., 1993, Short Note: Subtraction of powerline harmonics from geophysical records: *Geophysics*, **58**, 898 – 903.

Butler, K.E., 1996, Seismoelectric effects of electrokinetic origin: Ph.D. Thesis, The University of British Columbia, Canada.

Butler, K.E., Russell, R.D., Kepic, A.W. and Maxwell, M., 1996, Measurement of the seismoelectric response from a shallow boundary: *Geophysics*, **61**, 1769-1778.

Butler, K.E., Kepic, A.W., and Rosid, M.S., 2002, An experimental seismoelectric survey for groundwater exploration in the Australian Outback, *Proceedings of SEG Int'l Exposition and 72nd Ann. Meeting*, Salt Lake City, Utah, USA, p. 1484 – 1487.

Butler, K.E., and Russell, R.D., 2003, Cancellation of multiple harmonic noise series in geophysical records: *Geophysics*, **68**, 1083 – 1090.

Carter, R. Bruce, 2002, Butterworth Filters, <http://www.geocities.com/rbrucecarter/bu.htm>.

Christoforou, C.C., Westermann-Clark, G.B., and Anderson, J.L., 1985, The Streaming Potential and Inadequacies of the Helmholtz Equation: *Journal of Colloid and Interface Science*, **106**, 1 – 11.

Corwin, R. F., and Hoover, D. B., 1979, The self-potential method in geothermal exploration: *Geophysics*, **44**, 226 – 245.

Davis, J. A., James, R. O., and Leckie, J. O., 1978, Surface ionization and complexation at the oxide/water interface: *Journal of Colloid and Interface Sciences*, **63**, 480 – 499.

Debye, P., 1933, A method for the determination of the mass of electrolyte ions: *J. Chem. Phys.*, **1**, 13.

Dobrin, M. B., and Savit, C. H., 1988, Introduction to geophysical prospecting, 4th Edition, McGraw Hill Book Co., Singapore.

Dodson, W.J., 1999, Hydrogeology of the Newdegate 1:250 000 sheet: Water and Rivers Commission, Hydrogeological Map Explanatory Notes Series, Report HM 5, 27p.

Fitterman, D.V., 1978, Electrokinetic and Magnetic Anomalies Associated with Dilatant Regions in a Layered Earth: *Journal of Geophysical Research*, **83**, 5923 – 5928.

Frenkel, J., 1944, On the theory of seismic and seismoelectric phenomena in moist soil: *Journal of Physics (USSR)*, **8**, 230 – 241.

Garambois, S. and Dietrich, M., 2001, Seismoelectric wave conversions in porous media: Field measurements and transfer function analysis: *Geophysics*, **66**, p. 1417 – 1430.

Garambois, S. and Dietrich, M., 2002, Full waveform numerical simulations of seismoelectromagnetic wave conversions in fluid-saturated stratified porous media: *J. of Geophysical Research*, v. **107**, n. B7, p. ESE 5 – 1 – ESE 5 – 18.

Geological Survey of Western Australia, 1984, Newdegate 1 : 250,000 Geological Series, Sheet SI 50-8: *Geological Survey of Western Australia*.

Grant, F. S., and West, G. F., 1965, Interpretation Theory in Applied Geophysics: McGraw-Hill, New York.

Haartsen, M. W., and Pride, S. R., 1997, Electroseismic waves from point sources in layered media: *Journal of Geophysical Research*, **102**, 24745 – 24769.

Hillel, D., 1980, Fundamentals of Soil Physics, Academic Press, London, p. 178.

Hingston, F. J., and Gailitis, V., 1976, The geographic variation of salt precipitated over Western Australia: *Australian Journal of Soil Research*, **14**, 319 – 335.

Hunter, R. J., 1981, Zeta Potential in Colloid Science: Principles and Applications, Academic Press, New York, p. 125.

Ishido, T., and Mizutani, H., 1981, Experimental and theoretical basis of electrokinetic phenomena in rock-water systems and its application to geophysics: *Journal of Geophysical Research*, **86**, 1763 – 1775.

Ivanov, A. G., 1939, Effect of electrization of earth layers by elastic waves passing through them: *Doklady Akademii Nauk SSSR*, **24**, n. 1, p. 42 – 45, (in English).

Ivanov, A. G., 1940, The seismoelectric effect of the second kind: *Izvestia Akademii Nauk SSSR, seriya geograficheskaya i geofizieskaya*, **4**, no. 5, 699 – 727, (English trnl. obtained from US library of congress).

Jouniaux, J., and Pozzi, J., 1995, Streaming potential and permeability of saturated sandstones under triaxial stress: Consequences for electrotelluric anomalies prior to earthquakes: *J. Geophys. Res.*, **100**, p. 10197 – 10209.

Kepic, A.W., Maxwell, M. and Russell R.D., 1995, Field trials of a seismoelectric method for detecting massive sulfides: *Geophysics*, **60**, 365-373.

Kepic, A. W., 1995, Seismoelectric responses from sulphide orebodies: Ph.D. Thesis, Department of Geophysics and Astronomy, University of British Columbia, Canada.

Kepic, A. W., and Russell, R. D., 1996, Fiber optic time break: *Geophysics*, **61**, p. 294 – 298.

Kepic, A., Russell, R. D., Maxwell, M., and Butler, K. E., 2001, Underground tests of the radio pulsed effect seismoelectric method at the Lynx Mine, Canada: *Canadian Journal of Exploration Geophysics*, **32**, no. 2, p. 107 – 112.

Kepic, A. W. and Butler, K. E., 2002, The art of measuring very low amplitude seismoelectric signals: *64th EAGE Conference & Exhibition Mtg.*, Expanded Abstracts, p. 193.

Kepic, A. W., and Rosid, M. S., 2004, Enhancing the seismoelectric method via a virtual shot gather: *SEG Int'l Exposition and 74th Ann. Meeting*, Denver, Colorado, USA, Expanded Abstracts, p. 1337 – 1340.

Lankston, R. W., 1990, High-Resolution in Refraction Seismic Data Acquisition and Interpretation: Investigations in Geophysics No. 5, in *Geotechnical and Environmental Geophysics*, Ed. Stanley H. Ward, p. 45 – 73, Society of Exploration Geophysicists, Tulsa, Oklahoma, USA.

Long, L.T. and Rivers, W.K., 1975, Field measurement of the electroseismic response: *Geophysics*, **40**, 233-245.

Lorne, B., Perrier, F., and Avouac, J.P., 1999a, Streaming potential measurements 1. Properties of the electrical double layer from crushed rock samples: *Journal of Geophysical Research*, **104**, 17857 – 17877.

Lorne, B., Perrier, F., and Avouac, J.P., 1999b, Streaming potential measurements 2. Relationship between electrical and hydraulic flow patterns from rock samples during deformation: *Journal of Geophysical Research*, **104**, 17879 – 17896.

Martner, S.T. and Sparks, N.R., 1959, The electroseismic effect: *Geophysics*, **24**, p. 297-308.

Maxwell, M., Russell, R.D., Kepic, A.W., and Butler, K.E., 1992, Electromagnetic responses from seismically excited target B: non-piezoelectric phenomena: *Exploration Geophysics*, **23**, 201-208.

Mikhailov, O.V., Haartsen, M.W. and Toksoz, M.N., 1997, Electroseismic investigation of the shallow subsurface: Field measurements and numerical modelling: *Geophysics*, **62**, 97-105.

Mitchell, J. K., 1993, Fundamentals of soil behavior, John Wiley and Sons, Toronto, Canada.

Mizutani, H., Ishido, T., Yokokura, T., and Ohnishi, S., 1976, Electrokinetic phenomena associated with earthquakes: *Geophysical Research Letters*, **3**, 365 – 368.

Morgan, F.D., Williams, E.R., and Madden, T.R., 1989, Streaming potential properties of Westerly granite with applications: *Journal of Geophysical Research*, **94**, p. 12449 – 12461.

Neev, J., and Yeatts, F.R., 1989, Electrokinetic effects in fluid-saturated poroelastic media: *Physical Review B*, **40**, 9135 – 9141.

Nitsan, U., 1977, Electromagnetic emission accompanying fracture of quartz-bearing rocks: *Geophy. Res. Lett.*, **4**, 333 – 336.

Palmer, D., 1986, Refraction Seismic, the lateral resolution of structure and seismic velocity, Handbook of geophysical exploration: section I. Seismic Exploration, Helbig, K. and Treitel, S. ed., Geophysical Press, London.

Parkhomenko, E.I., and Gaskarov, I.V., 1971, Borehole and laboratory studies of the seismoelectric effect of the second kind in rocks: Izv. Acad. Sci. USSR, *Physics of the Solid Earth*, (English translation by Am. Geophys. Union), **7**, 663 – 666.

Pride, S. R., and Morgan, F. D., 1991, Electrokinetic dissipation induced by seismic waves: *Geophysics*, **56**, 914 – 925.

Pride, S.R. and Haartsen, M.W., 1996, Electroseismic wave properties: *J. Acoust. Soc. Am.*, **100**, 1301-1315.

Pride, S. R., 1994, Governing equations for the coupled electromagnetic and acoustics of porous media: *Physical Review B.*, **50**, p. 15678-15696.

Revil, A., Darot, M., and Pezard, P. A., 1996, From surface electrical properties to spontaneous potentials in porous media: *Surv. Geophysics*, **17**, p. 331 – 346.

Rosid, M.S., and Kepic, A.W., 2003, Groundwater Exploration via Seismoelectric Survey, *Proceedings the 6th SEGJ International Symposium*, Tokyo, Japan, p. 348 – 353.

Rosid, M.S., and Kepic, A.W., 2004, Using the seismoelectric method for hydrogeological investigations: *Proceedings the EEGS Annual Meeting SAGEEP 2004*, Denver, Colorado, USA, p. 1480 – 1489.

Rosid, M.S., and Kepic, A.W., 2005, Hydrogeological mapping using the seismoelectric method: *Exploration Geophysics*, **36**, p. 245 – 249.

Russell, R. D., Butler, K. E., Kepic, A. W., and Maxwell, M., 1997, Seismoelectric exploration: *The Leading Edge*, **16**, 1611 – 1615.

Shaw, D. J., 1969, Electrophoresis, Academic Press, London.

Sheriff, R.E., 1996, Understanding the Fresnel Zone, Geophysical Corner, *AAPG Explorer*,<http://www.searchanddiscovery.net/documents/geophysical/sheriff/images/sheriff.pdf>

Sheriff, R. E., 2002, Encyclopedic Dictionary of Applied Geophysics, Fourth Edition, Society of Exploration Geophysicists, Oklahoma, USA.

Sill, W. R., 1983, Self-potential modeling from primary flows: *Geophysics*, **48**, p. 76 – 86.

Sioni, Sioni, 2003, Imaging a Sand Lens within the Leederville and Yarragadee Aquifers (WA) Using Resistivity, TEM, AMT, and Seismic: *MSc Thesis*, Curtin University of Technology, Perth, WA.

Sobolev, G. A., Demin, V. M., Los, V. F., and Maybuk, Yu. Ya., 1980, Mechano-electrical radiation from orebodies: *Dokl. Akad. NAUK. S.S.S.R.*, **252**, 1353 – 1355.

Sobolev, G. A., Demin, V. M., Los, V. F., and Maybuk, Yu. Ya., 1982, Study of the electromagnetic radiation of rocks containing semiconductor and piezoelectric minerals: *Izv. Akad. NAUK. S.S.S.R., Fizika Zemli*, no. 11, 72 – 86. (English Tranl. 1983, *Izv. Acad. Sci. U.S.S.R., Physics of the Solid Earth*, **18**, 888 – 897).

Sobolev, G. A., Demin, V. M., Narod, B. B., and Whaite, P., 1984, Test of piezoelectric and pulsed radio methods for quartz vein and base-metal sulfides prospecting at Giant Yellowknife Mine, NWT, and Sullivan Mine, Kimberley, Canada: *Geophysics*, **49**, 2178 – 2185.

Steeple, D. W., and Miller, R. D., 1990, Seismic Reflection Methods Applied to Engineering, Environmental, and Groundwater Problems: *Geotechnical and Environmental Geophysics*, Ed. Stanley H. Ward, Vol. I, Society of Exploration Geophysicists, Tulsa, USA.

Strachan, E., and Wolfe, P. J., 2001, Seismoelectric Investigations at Clean and Contaminated Sites: 14th Annual Symposium on the Application of Geophysics to Engineering and Environmental Problems, March 4 – 7, 2001, Denver, Colorado, *Expanded Abstracts*.

Sumner, J. S., 1976, Principles of Induced Polarization for Geophysical Exploration, Development in Economic Geology, 5, Elsevier Scientific Publishing Company, Amsterdam, Netherlands.

Telford, W.M., Geldart, L.P., and Sheriff, R.E., 1996, Applied Geophysics, 2nd edition, Cambridge University Press, USA.

Thompson, R.R., 1936, The seismic-electric effect: *Geophysics*, **1**, 327 – 335.

Thompson, R.R., 1939, A note on the seismic-electric effect: *Geophysics*, **4**, 102 – 105.

Thompson, A.H. and Gist, G.A., 1993, Geophysical applications of electrokinetic conversion: *The Leading Edge*, **12**, 1169-1173.

Tuck, G.J., Stacey, F.D., and Starkey, J., 1977, A search for the piezoelectric effect in quartz-bearing rocks: *Tectonophysics*, **39**, T7 – T11.

Volarovich, M. P., and Parkhomenko, E. I., 1954, The piezoelectric effect in rocks, *Izv. AN SSSR, ser. Geophys.*, **3**, 37 – 48.

Volarovich, M.P., Parkhomenko, E.I., and Sobolev, G.A., 1959, Field investigation of the piezoelectric effect in quartz bearing rocks: *Dokl. Akad. NAUK. S.S.S.R.*, 128, no. 3. (English Tranl. **128**, 964 – 966).

Volarovich, M.P. and Sobolev, G.A., 1969, Direct piezoelectric prospecting of quartz and pegmatic veins: *Geoexploration*, **7**, 241 – 246.

Water Corporation, 2001, Water Corporation of Western Australia submission to the senate enquiry into Australia's urban water management, July 2001: *Water Corporation* (<http://www.aph.gov.au/senate/committe/ecitactte/water/submissions/sub049.pdf>).

Yamada, I., Masuda, K., and Mizutani, H., 1989, Electromagnetic and acoustic emission associated with rock fracture: *Phys. Earth and Plan. Int.*, **57**, 157 – 168.

Yilmaz, O., 2001, Seismic Data Analysis: Vol. I, Society of Exploration Geophysicists, USA.

Zablocki, C. J., 1966, Electrical Transients Observed during Underground Nuclear Explosions: *J. of Geophysical Research*, **71**, 3523 – 3542.

Zhu, Z., Haartsen, M., and Toksoz, M. N., 2000, Experimental studies of seismoelectric conversions in fluid-saturated porous media: *J. of Geophysical Research*, v. **105**, p. 28,055 – 28,064

Zhu, Z., and Toksoz, N. M., 2003, Seismoelectric Measurements in Cross Borehole Models with Fractures, *Proceedings the 6th SEGJ International Symposium*, Tokyo, Japan, p. 342 – 347

Every reasonable effort has been made to acknowledge the owners of copyright material. I would be pleased to hear from any copyright owner who has been omitted or incorrectly acknowledged.